Dynamic Simulation Techniques for Airborne Wind Energy Systems

Evaluating the role of kite inertia in a soft-wing system operated in pumping cycles

Vince van Deursen

TU Delft

Dynamic Simulation Techniques for Airborne Wind Energy Systems

Evaluating the role of kite inertia in a soft-wing system operated in pumping cycles

Thesis

for the purpose of obtaining the degree of Master of Science
at Delft University of Technology,
to be defended publicly on Wednesday September 4, 2024 at 2:30 pm

by

Vince van Deursen

Supervisors:	Dr.-Ing. R. Schmehl
	O. Cayon MSc.
Date:	August 2024
Faculty:	Aerospace Engineering

Cover: Kitepower's V5.40 kite with $40\,\mathrm{m}^2$ wing surface area operating on the former naval airbase Valkenburg (July 2018) [1].

Abstract

Airborne wind energy (AWE) systems harness wind power using devices that fly in controlled patterns. Two main concepts exist, where the kite is performing crosswind maneuvers. In the 'drag mode' concept, power is generated onboard, whereas power is generated on the ground in the 'pumping cycle concept'. Quasi-steady state modeling (QSM) is a robust technique for simulating the behavior of a soft kite in a pumping cycle AWE system due to its ease of use – requiring minimal tuning of modeling coefficients – and its ability to rapidly deliver results with reasonable accuracy. QSM effectively predicts parameters like tether force and kite velocity for smaller AWE systems. However, its limitations become apparent with increasing kite mass, where the neglect of inertial forces leads to notable inaccuracies in tether tension and unresolved phase differences between acceleration and velocity. The threshold kite mass-to-surface ratio at which these errors become significant remains undefined, as well as a consistent definition of quasi-steadiness in the context of AWE. This research aims to present such definition and to quantify the validity limits of assuming quasi-steadiness. Dynamic equations of motion tailored to AWE applications are derived, and various parameterization techniques to simulate dynamic motion along a predetermined flight path are presented. The solution space of three modeling approaches – steady, quasi-steady, and dynamic – are compared to assess the significance of different components of inertial forces, such as those caused by Coriolis, centrifugal, Euler, or relative accelerations. The study shows that if only a time-averaged quantity is of interest (e.g. average traction power), the quasi-steady model is reasonably accurate, provided a sufficient distance to the feasibility boundaries of the solution space. However, the quasi-steady model fails to accurately predict other aspects of the solution, such as amplitude or phase. The limitations of this analysis stem from the use of a steady aerodynamic model with constant lift and drag coefficients, and the assumption of a rigid, inertia-free tether. Consequently, the presented dynamic model still leaves various unsteady real-world effects unresolved, introducing potential sources of error. This research seeks to serve as a foundational step for future research, enabling more in-depth investigation of the many unsteady phenomena present in AWE systems.

Preface

Organization

This thesis is submitted in partial fulfillment of the requirements for the Master of Science degree in Aerospace Engineering at Delft University of Technology. The research presented in this document reflects the culmination of my studies and the knowledge I have acquired during my time at this exciting institution.

The thesis, part of the Aerospace & Wind Energy master's track at the Faculty of Aerospace Engineering, is a project of approximately one academic year, in which the student demonstrates their ability to independently plan and execute a research or design project, apply relevant theory, critically analyze results, and produce outcomes scientifically relevant in the fields of of aerodynamics and wind energy. This work dives into the relatively new topic of airborne wind energy (AWE), with a particular focus on the dynamics of crosswind tethered flight.

The document is organized as follows. In chapter 1, the topic of AWE is introduced, and the unsteady nature of crosswind tethered flight is explained. Chapter 2 presents a literature review on the techniques available for simulating crosswind tethered flight. Subsequent knowledge gaps are identified and the main research question and methodology are presented in chapter 3. Chapters 4 to 6 are all dedicated to the development of the presented theoretical framework on crosswind tethered flight dynamics. This framework is verified in chapter 7 and extensively tested in chapter 8. Finally, chapter 9 concludes the research by addressing the main research question and sub-questions, with chapter 10 discussing the limitations of the study and offering recommendations for future research.

Acknowledgments

Wind energy and aerodynamics have fascinated me ever since I was a child. Family holidays were often spent sailing through the Zeeland Delta, and weekends were dedicated to building radio-controlled model aircraft with my father and grandfather. These experiences motivated me to study aerospace engineering at Delft University of Technology and to pursue competitive sailing.

The first time I met Dr.-Ing. Roland Schmehl and Oriol (Uri) Cayon PDEng., my supervisors, was online in the summer of 2023. Naturally, I was on a sailing boat, anchored off the coast of Belgium. While the boat's rocking motion had me swaying side-to-side in front of the camera, I heard Roland say that he never had seen such a quick response to a thesis vacancy. I suppose my affinity with wind energy and sailing made for an easy decision when stumbled upon it.

Roland mentioned, ”I think your background as a data scientist and your competitive sailing hobby will come in handy”. And indeed, he was right. This thesis has seen countless hours of coding, code restructuring, and a wide variety of emotions reflected in my git commit messages – from frustration to eventual satisfaction. Moreover, the perseverance developed through competitive sailing, really helped me to delve into the theory and mathematics required for this field of research. Although I am not sure if Roland anticipated the resulting (sometimes rather lengthy) discussions on terminology when he made his comment, haha.

I am grateful for the opportunity to conduct this research together with Roland and Uri. Thank you, Roland, for always bringing up new information or suggesting alternative approaches whenever I was stuck on something. Thank you, Uri, for your valuable insights and terminology suggestions, which greatly contributed to the quality of the final result.

Furthermore, I would like to thank my thesis assessment committee members Prof.dr. Simon Watson and Dr.ir. Alexander (Sander) Van Zuijlen, for their interest in this thesis and for taking the time to read and assess this work. And finally, thank you to my parents, for always inspiring me to go the extra (nautical) mile.

Vince van Deursen
Delft, August 2024

Contents

Preface ii

Nomenclature v

1 Introduction 1
- 1.1 Development history of airborne wind energy systems 1
- 1.2 Unsteady nature of crosswind tethered flight 2

2 Available techniques for modeling pumping cycle AWE system dynamics 4
- 2.1 Building blocks of an AWE system model 4
- 2.2 Quasi-steady modeling 4
  - 2.2.1 Early quasi-steady modeling 5
  - 2.2.2 Empirical validation of a quasi-steady model with no inertial forces 6
  - 2.2.3 The versatility of quasi-steady modeling 6
  - 2.2.4 Analytical solution for a quasi-steady helical path 8
- 2.3 Dynamic modeling 9
  - 2.3.1 Dynamic model with realistic system components 9

3 Research design 10
- 3.1 Need for research in the context of tethered flight dynamics 10
  - 3.1.1 Ambiguity in the definition of quasi-steadiness 10
  - 3.1.2 Incomplete understanding of the impact of assuming quasi-steadiness 10
  - 3.1.3 Limited availability of dynamic models 10
  - 3.1.4 Lack of tailored dynamic equations of motion 10
  - 3.1.5 Simplistic path control techniques 11
- 3.2 Research objectives and questions 11
- 3.3 Methodology 11

4 Deriving equations of motion of tethered flight 13
- 4.1 Reference frames 13
  - 4.1.1 Wind reference frame W 13
  - 4.1.2 Azimuth-Zenith-Radial reference frame AZR 13
  - 4.1.3 Course reference frame C 14
- 4.2 Translational motion in the course reference frame 15
  - 4.2.1 Velocity in the course reference frame 16
  - 4.2.2 Acceleration in the course reference frame 16
- 4.3 Equations of motion in the course reference frame 18
  - 4.3.1 Dynamic equilibrium 18
  - 4.3.2 Inertia-free equilibrium 19
  - 4.3.3 Steady equilibrium 19
  - 4.3.4 Quasi-steady equilibrium 19

5 Modeling external loads on the kite 22
- 5.1 Tether force of an inertia-free, straight tether 22
  - 5.1.1 Tether force due to distributed tether drag load 23
  - 5.1.2 Tether force due to simplified tether drag 24
- 5.2 Aerodynamic force acting on the kite 25

6 Imposing the kite trajectory 28
- 6.1 General parameterization problem description 28
- 6.2 Parameterization equations in the AZR-frame 29
- 6.3 Setting up path parameterizations 30

6.3.1 Parameterizing in s . . . 31
6.3.2 Parameterizing in both s and t . . . 33
6.4 Parameterized position integration schemes . . . 34
6.4.1 Dynamic position integration . . . 34
6.4.2 Quasi-steady position integration . . . 35

7 Verifying the dynamic model **37**
7.1 Qualitative discussion on the equations of motion . . . 37
7.2 Comparison to Talmar's asymptotic solutions . . . 37
7.3 Verification of the distributed tether drag model . . . 38
7.3.1 Comparison with the simplified drag tether model . . . 39

8 Analyzing the impact of the inertial forces **40**
8.1 Qualitatively assessing the effect of the distinct inertial terms . . . 40
8.1.1 Identifying the dominating the inertial components . . . 40
8.1.2 Examining the phase differences in the solutions . . . 41
8.2 Other effects of dynamic simulation . . . 43
8.2.1 Transient and asymptotic parts in the solution . . . 43
8.2.2 Increased smoothness of the dynamic solution . . . 44
8.2.3 Enlarged solution space of the dynamic simulation . . . 44
8.3 Solution space comparison . . . 46
8.3.1 Sensitivity of the normalized average traction power . . . 47
8.3.2 Sensitivity of the tangential speed variation . . . 48
8.3.3 Sensitivity of the phase of the velocity response . . . 50
8.4 Sensitivity to wind conditions . . . 52
8.4.1 Impact of the mean wind speed profile . . . 52
8.4.2 Impact of turbulence . . . 53
8.5 Impact of the tether model . . . 55

9 Conclusions **56**
9.1 Summary of the developed theory and models . . . 56
9.2 The impact of kite inertia . . . 57

10 Recommendations **59**
10.1 Improvements to the current work . . . 59
10.2 Research made accessible by the current work . . . 59

References **61**

A Simulation parameters **63**

Nomenclature

Abbreviations

Abbreviation	Expansion
AEP	Annual Energy Production
AWE	Airborne Wind Energy
DOF	Degree Of Freedom
EOM	Equations Of Motion
KCU	Kite Control Unit
QSM	Quasi Steady Model

Symbols

Symbol	Definition	Unit
C	Aerodynamic coefficient, subscripts L, D, for lift and drag	-
D	Aerodynamic drag	N
d_t	Tether diameter	m
F_a	Aerodynamic force	N
F_g	Gravitational force	N
F_t	Tether force at kite-tether interface	N
$F_{t,g}$	Tether force at ground station	N
f	Reeling factor	-
f_x	Reeling factor in downwind direction	-
g	Gravitational acceleration	$\mathrm{m\,s^{-2}}$
L	Aerodynamic lift	N
m	Mass, subscripts k, t for kite, tether	kg
M	Moment	N m
P	Power	W
r	Radial distance	m
s	Path coordinate	-
t	Time	s
v_w	True wind speed	$\mathrm{m\,s^{-1}}$
v_a	Apparent wind speed	$\mathrm{m\,s^{-1}}$
v_k	Kite speed	$\mathrm{m\,s^{-1}}$
β	Elevation angle	rad
γ_a	Aerodynamic flight path angle	rad
Φ	Phase	rad
ϕ	Azimuth angle	rad
ϕ_a	Aerodynamic roll angle	rad
θ	Polar angle	rad
χ	Course angle	rad
χ_a	Aerodynamic heading angle	rad
ω	Path maneuver frequency	$\mathrm{rad\,s^{-1}}$
$\mathbf{r}$	Position vector, with subscript k for kite, t for tether.	-
$\mathbf{R}$	Parameterized position vector	-
$\mathbf{\Omega}$	Rotation vector referring to the rotation of a reference frame	-

Notation

In this report, the following notation conventions are used.

- Vectors are denoted by bold symbols and the letter $\mathbf{e}$ denotes a unit vector, such that $\mathbf{x} = x\mathbf{e}_x$.
- The subscript of a vector denotes the vector component in a direction, i.e. the kite velocity in the radial direction becomes $\mathbf{v_{k,r}}$. A further distinction is made between velocity and speed, i.e. the radial speed $v_r = \|\mathbf{v_r}\|$
- Dotted symbols represent total time derivatives, e.g. the derivative $\frac{dr}{dt} = \dot{r}$.
- Accelerations and velocities are referred to as absolute, unless square brackets are used. For example, $\dot{\mathbf{r}}$ would be the absolute velocity as seen from an inertial reference frame, whereas $[\dot{\mathbf{r}}]$ is the velocity relative to a moving reference frame.
- Vector-superscripts denote the unit vectors in which a vector in matrix notation is expressed. For example:

$$\begin{bmatrix} x \\ y \\ z \end{bmatrix}^{x,y,z} \equiv x\mathbf{e}_x + y\mathbf{e}_y + z\mathbf{e}_z$$

- Coordinate transformation matrices are denoted as $\mathbb{T}$. Its interpretation depends on the number of subscripts:
  - Singular subscripts, followed by an angle in round brackets, refers to a rotation of that angle around a (unit) vector. For example, $\mathbb{T}_x(-\alpha)$ is a rotation of $-\alpha$ around the $\mathbf{e}_x$ vector.
  - Double subscripts refer to the reference systems, with the first reference system being obtained from the second. For example: $\mathbb{T}_{B\leftarrow A}$ (read: B from A) is the transformation matrix that transforms A-frame basis vector components into B-frame basis vector components.

1
Introduction

1.1. Development history of airborne wind energy systems

Airborne wind energy (AWE) is a relatively new field of research, which after the seminal work of Loyd in 1980 [2], only really started developing in the 21st century [3]. The fruitful concept of AWE could form a significant contribution to the ongoing transition towards more sustainable electricity generation [3, 4, 5].

Where conventional horizontal axis wind turbines employ tower-mounted rotors to generate electrical power from the wind, the electrical power in an AWE system is generated by a kite. Although many AWE concepts exist, the most well-researched concepts are those where the kite performs crosswind flight maneuvers. In a "drag mode" AWE system, energy is generated by wind turbines that are mounted on the kite, which is flying crosswind maneuvers continuously. In a "pumping cycle" AWE system, energy is generated on the ground by the reel-out and reel-in of the tether, where the traction force is high during reel-out and low during the reel-in and transition flight phases. The name 'pumping cycle' refers to the alternating reel-in and reel-out motion of the kite. The kite is performing crosswind maneuvers during reel-in, which are discontinued during reel-out. Various companies are working to transform these concepts into commercially viable products, such as Kitepower's 100kW soft-kite pumping cycle system [6].

Compared to conventional horizontal axis wind turbines, AWE systems require much fewer materials to produce the same amount of energy as no heavy foundation or tower is required [3]. Furthermore, they access winds at higher altitudes resulting in a higher capacity factor as the wind is less turbulent and speeds are higher [4]. The currently untouched wind resource in wind speed maxima such as lower level jets is estimated at roughly three times the 2012 global electricity demand [4]. Commercialization of AWE systems is being challenged by the lack of favorable legislation, lack of design and operation standards, increased system complexity, and decreased robustness compared to conventional wind turbines [4]. In terms of cost, it seems that economically feasible AWE systems can be built significantly smaller than conventional turbines [7]. To support the development of AWE systems, it is important to be able to predict the system's behavior accurately with a robust and efficient model.

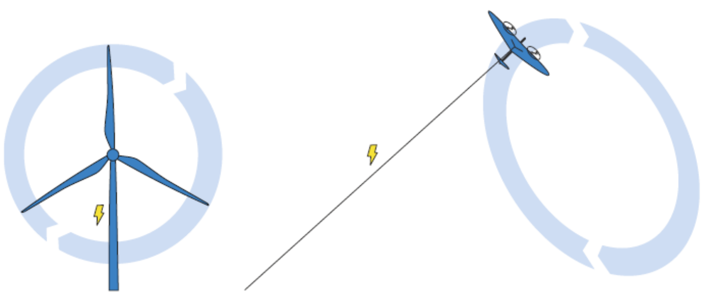

Figure 1.1: Conventional wind turbine (left) vs. FlyGen crosswind concept (right), from Zillman and Bechtle [8].

1.2. Unsteady nature of crosswind tethered flight

Any kite that is flying crosswind maneuvers inherently experiences unsteady flight conditions, as its motion is constrained by the tether. Typical crosswind flight patterns are circular or figure-eight-like, and during such maneuvers, the kite's speed and direction are constantly changing. This dynamic nature of tethered flight translates to all kinds of unsteady phenomena in the AWE system, each with a varying timescale and intensity.

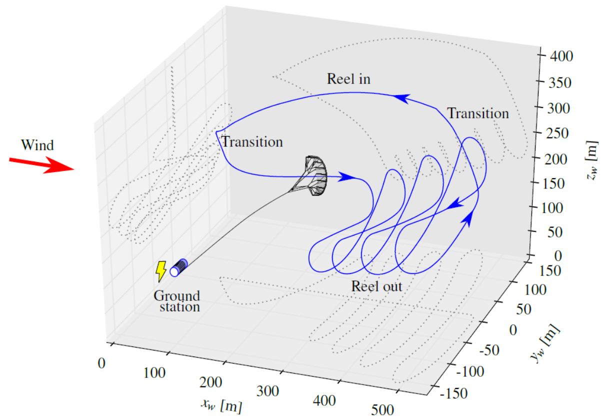

Figure 1.2: A kite flying a figure-eight crosswind pattern is constantly changing direction. From Fechner [9].

Table 1.1 shows an overview of common unsteady phenomena observed in crosswind-flying AWE systems. When the period is significantly shorter than the duration of one crosswind maneuver, the effects of such phenomena tend to average out over time. This nullifies the need to accurately resolve such phenomena when simulating system-level quantities like tether force and kite velocity.

In contrast, slow unsteady effects, such as centrifugal forces caused by the kite directional change, occur over longer periods and are thus more likely to significantly influence the error in predicted system-level quantities when left unresolved.

Table 1.1: Examples of phenomena that form sources of unsteadiness in a crosswind-flying AWE system, ranked by timescale.

Phenomenon	**Consequences**	**Timescale [s]**
Tether reel-in / reel-out	Variation in tether length introduces Coriolis acceleration. Variation in airborne mass creates unsteady difference between tether tension at kite versus tension at the ground station.	$\mathcal{O}(10^1)$ to $\mathcal{O}(10^2)$ [a]
Wind shear / veer in ABL	Variation in local true wind velocity creates unsteadiness in aerodynamic loads.	$\mathcal{O}(10^1)$ to $\mathcal{O}(10^2)$ [a]
Kite (de)powering	Variation in kite pitch causes unsteadiness in aerodynamic loads.	$\mathcal{O}(10^1)$ to $\mathcal{O}(10^2)$ [a]
Kite steering	Kite deformation causes aerodynamic unsteadiness. Change in sideslip angle and angle of attack causes aerodynamic unsteadiness.	$\mathcal{O}(10^0)$ to $\mathcal{O}(10^1)$ [b]
Variation in kite direction	Causes inertial forces experienced by the tether and kite.	$\mathcal{O}(10^0)$ to $\mathcal{O}(10^1)$ [b]
Variation in kite speed	Causes inertial forces and unsteadiness in aerodynamic loads.	$\mathcal{O}(10^0)$ to $\mathcal{O}(10^1)$ [b]
Microscale turbulence	Variation in local true wind velocity creates unsteadiness in the aerodynamic loads. Microscale atmospheric turbulence and the corresponding timescale is discussed in more detail by Schön and Kermarrec [10].	$\mathcal{O}(10^{-1})$ to $\mathcal{O}(10^1)$
Tether aeroelastic effects (eg. lock-in, vortex-induced vibrations)	Unsteadiness in tether drag and tension. Various tether aeroelastic phenomena and their timescale are discussed in more detail by Dunker [11].	$\mathcal{O}(10^{-3})$ to $\mathcal{O}(10^0)$
Kite aeroelastic effects (eg. trailing edge flutter, seam-ripping)	Unsteadiness in aerodynamic loads on the kite. Various kite aeroelastic phenomena are discussed in more detail by Leuthold [12].	$\mathcal{O}(10^{-3})$ to $\mathcal{O}(10^0)$

[a] The timescale of these phenomena is the same order of magnitude as the duration of one pumping cycle, which is typically $\mathcal{O}(10^1)$ to $\mathcal{O}(10^2)$ seconds. For example, KitePower's V3 prototype LEI pumping cycle system had a mean pumping cycle duration of 131.0 s over 87 pumping cycles [13].
[b] The timescale of these phenomena is the same order of magnitude as the number of maneuvers during one pumping cycle, which is around $3 - 10$ times smaller than the cycle duration, an example given in figure 1.2.

2

Available techniques for modeling pumping cycle AWE system dynamics

2.1. Building blocks of an AWE system model

Any AWE system model combines elements of dynamics, fluid mechanics, structural mechanics, and control theory. Figure 2.1, somewhat analogous to the well-known Collar's Triangle in the field of aeroservoelasicity, shows the integration of the individual component models required for a complete system model. The complexity with which each system component (i.e. kite, tether, and generator) is modeled, ultimately determines which unsteady phenomena in table 1.1 are resolved.

This chapter offers an overview of the modeling techniques available for estimating the behavior of soft-kite, pumping cycle AWE systems. It particularly focuses on the method used to simulate the motion of the airborne components, i.e. the 'dynamics' block in figure 2.1. The flight dynamics are typically modelled as quasi-steady or fully dynamic.

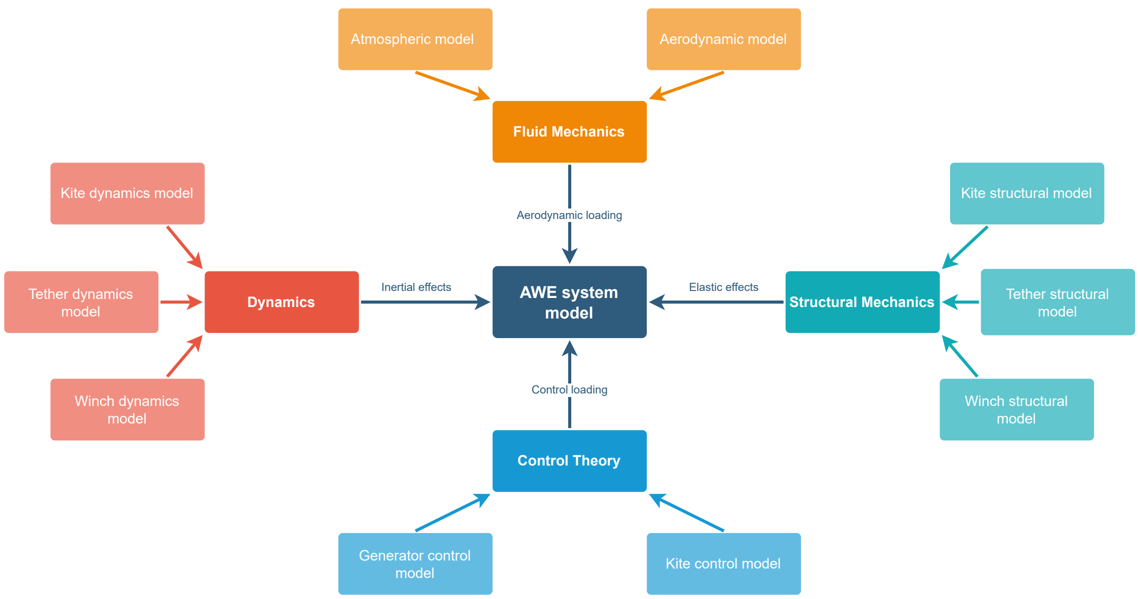

Figure 2.1: AWE system modeling building blocks.

2.2. Quasi-steady modeling

Simulating the dynamic motion of an AWE system is complicated, as this essentially forms a second order differential problem. However, when certain acceleration terms in the equations of motion are neglected, the differential problem may be reduced to a first order problem, meaning that the force equilibrium at any point in time is independent of past or future equilibria. Thus, by neglecting certain acceleration terms, the system state becomes time-invariant, which greatly simplifies the motion simulation the airborne components in an AWE system.

In AWE literature, such model in which certain acceleration terms are neglected, is often referred to as a quasi-steady model (QSM). Many QSM variations have been used throughout literature – as will be discussed in this section.

2.2.1. Early quasi-steady modeling

In the 2013 master's thesis by Noom [14], a quasi-steady framework was introduced to analyse the mechanical power generation of a pumping cycle AWE system. In this framework, Noom derived quasi-steady equations of motion in spherical coordinates, using the physics convention. Noom presented a method to simulate the full pumping cycle in a computationally efficient manner.

To obtain a quasi-steady model, Noom neglects specific inertial force components. Noom's quasi-steady assumption dictates that at any instance in time, the changes in the tangential and radial speed components are small. The corresponding quasi-steady polar acceleration $\ddot{\theta}$ and quasi-steady azimuth acceleration $\ddot{\phi}$ consequentially became equations (2.1) and (2.2), resulting in the quasi-steady inertial force in equation (2.3). The force equilibrium at any position was then calculated iteratively, without requiring past or future information of the system.

$$\ddot{\theta} = -\dot{\theta}\left(\frac{\dot{r}}{r} + \dot{\chi}\tan\chi\right) \tag{2.1}$$

$$\ddot{\phi} = -\dot{\phi}\left(\frac{\dot{r}}{r} - \dot{\chi}\frac{1}{\tan\chi} + \dot{\theta}\frac{1}{\tan\theta}\right) \tag{2.2}$$

$$\mathbf{F_{i,qs}} = -m\begin{bmatrix} \ddot{r} - r\dot{\theta}^2 - r\dot{\phi}^2\sin^2\theta \\ r\ddot{\phi} + 2\dot{r}\dot{\phi} - r\dot{\phi}\sin\theta\cos\theta \\ r\ddot{\phi}\sin\theta + 2\dot{r}\dot{\phi}\sin\theta + 2r\dot{\theta}\dot{\phi}\cos\theta \end{bmatrix}\begin{bmatrix}\mathbf{e}_\theta \\ \mathbf{e}_\phi \\ \mathbf{e}_\mathrm{r}\end{bmatrix} \tag{2.3}$$

Noom briefly analyzed the impact of this quasi-steady assumption: considering straight flight, the result on the force equilibrium was small, but the effect on the flight conditions was significant ([14]. As the result on the force equilibrium was small, all inertial forces were neglected in the subsequent modeling of the full pumping cycle.

Noom simulated the generated power throughout the traction phase by parameterizing the figure-eight flight pattern. The polar angle θ and the azimuth angle ϕ were both prescribed as functions of parameterization coordinate s. Then, the change in position due to a timestep dt followed from the derivative $\frac{ds}{dt}$ in equation (2.4), or equation (6.7) in [14]. Noom then efficiently simulated the kite motion with the forward Euler scheme in equation (2.5).

$$\frac{ds}{dt} = \frac{\lambda v_w}{r\sqrt{\frac{d\theta}{ds}^2 + \frac{d\phi}{ds}^2}} \tag{2.4}$$

$$\Delta s = \frac{ds}{dt}\Delta t \tag{2.5}$$

Noom's work proved to become a starting point for future work, as the framework is very useful to quickly assess the power and forces generated throughout the traction phase in a pumping cycle AWE system. However, the assessment on the impact of assuming quasi-steadiness is rather brief, and the necessity of this assumption is not thoroughly addressed. Noom acknowledges these limitations and recommends further research on this topic.

An arguable caveat in Noom's work is the lack of clarity on when the quasi-steady inertial force in equation (2.3) is resolved, or when all inertial forces are neglected. Additionally, equations (2.1) to (2.3) are rather lengthy and difficult to interpret, complicating model verification. Moreover, Noom's position integration scheme introduces two model errors: equation (2.5) neglects any variation in kite speed, and equation (2.4) does not properly account for the curvature of the flight path (to be further discussed in chapter 6).

Concluding, Noom's work is an important stepping stone, but also brings up questions about the impact of assuming quasi-steadiness, what the definition of quasi-steadiness should be, and how the kite motion should be modeled in a parameterized way.

2.2.2. Empirical validation of a quasi-steady model with no inertial forces

In 2019, Van Der Vlugt et al. continued Noom's work and applied the quasi-steady theory to simulate the motion of the 20kW pumping cycle AWE 'technology demonstrator', developed by Delft University of Technology [15]. Where Noom resolved certain inertial forces in some traction phase simulations, in the paper by Van Der Vlugt et al., all inertia forces were consistently neglected. The tether force corresponding to this inertia-free equilibrium, was then calculated by equation (2.6).

$$\mathbf{F_t} = \mathbf{F_a} - \mathbf{F_g} \tag{2.6}$$

Van Der Vlugt et al. modeled the kite as a lumped mass for which the lift and drag coefficients are assumed constant throughout a flight phase. The true wind velocity and air density at the kite are determined with the log and exponential laws presented by Stull [16]. The inelastic tether is lumped with the kite, the steady tether sag is accounted for, and the tether drag is implemented as an additional drag component in the system's aerodynamic drag coefficient per equation (2.7). Each quasi-steady state equilibrium was then solved iteratively.

$$C_D = C_D, k + \frac{d_t r}{4S} C_{D,c} \tag{2.7}$$

To simulate a full pumping cycle, Van Der Vlugt et al. simulated the retraction, transition, and traction phases in a distinct manner. This resulted in a discontinuous flight path.

In the retraction and transition phases, the position of the kite is updated through a backward finite difference scheme, where the radial kite speed resulted from a control input and the tangential kite speed followed from solving the quasi-steay equilibrium.

In the traction phase, the tangential motion of the kite was not resolved. Instead, the traction phase was modeled as a sequence of representative states, for which the position and heading was predetermined (e.g. the area center of one of the figure-eight lobes). It was assumed that the forces obtained by solving the representative state equilibrium, would correspond well with the average forces throughout the traction flight pattern.

The model was compared to experimental data of the 20kW technology demonstrator, comprised of test data in moderate winds and strong winds. Van Der Vlugt et al. concluded that the model is perfectly suited as a basis for optimization and scaling studies, but also acknowledge that it is not suitable for investigating dynamics-related topics, such as peak loading during crosswind maneuvers. In a more extensive validation study by Schelbergen and Schmehl [13], the same model was compared to much more flight data (87 pumping cycles) of the same kite, albeit with a different ground station. The estimated cycle duration was highly accurate with an error of -1.7%, and the error in the mean cycle power was -26.4%. Because of the required tuning of the drag coefficient, Schelbergen and Schmehl conclude that some modeling choices should be reassessed to obtain an accurate white-box model.

Summarizing, the validation study by Schelbergen and Schmehl shows that a quasi-steady framework, such as Noom's [14] or the one by Van Der Vlugt et al. [15], may be used to efficiently simulate AWE system behavior, although certain improvements may be necessary.

2.2.3. The versatility of quasi-steady modeling

To demonstrate the versatility of quasi-steady modeling, this section presents examples of studies in which the efficiency of QSM allowed to effectively answer complex questions, regarding the operation of AWE systems.

Cycle efficiency optimization by Fechner and Schmehl, 2013

Fechner and Schmehl used a quasi-steady model in 2013 to analyze the cycle efficiency of a pumping kite system in 2013 [17]. They resolved the traction phase as a sequence of representative states with constant azimuth and elevation angles. During the transition and retraction phases, the change in elevation angle due to the kite speed was resolved. This simple yet effective model was then used to optimize the pumping cycle power efficiency, by controlling the reel-out and reel-in speeds. A constraining maximum tether force was included in the optimization procedure.

Fechner and Schmehl introduced the terms pumping efficiency, cycle efficiency and total efficiency. Such terms are useful to quantify the efficiency of a pumping kite system. Fechner and Schmehl concluded that the Delft University of Technology's 20kW demonstrator achieves a maximum total efficiency of 20%, and showed that their model indicates a maximum total efficiency of 50% to 60%, for a medium sized pumping cycle system. All in all, Fechner and Schmehl showed how having an efficient model to predict the energy production of an AWE system aids the development of such system, as it can be used to optimize the control and therefore energy yield.

Flight path optimization and control by Jerez Venegas, 2017

Also Jerez Venegas demonstrated in their master's thesis of 2017 [18] the versatility of quasi-steady modeling. Jerez Venegas investigated the optimal pumping cycle trajectory and used the same quasi-steady modelling approach as Noom's due to its high computational efficiency. Whereas Fechner and Schmehl in [17] only considered two-dimensional kite motion, Jerez Venegas modeled the turning maneuvers of the kite during the traction phase.

The steering of the kite was resolved by deriving a 'turn rate law', that is, an equation that dictates the course angle rate of change $\dot{\chi}$. This law was then used in a controller to fly realistic, continuous flight paths without discontinuities. An optimizer was developed to determine the Lissajous-figure-eight traction trajectory that would result in the highest average instantaneous power.

Jerez Venegas' work shows how assuming quasi-steadiness allows to efficiently investigate various topics. They showed how a controller can be developed to effectively follow a predetermined flight path, and how such flight path can be power-optimized. However, Jerez Venegas' work again raises subsequent questions related to the dynamics of the system. It is not well-explained how the average power is calculated throughout the flight phases, and how this power is affected by the quasi-steadiness assumption.

To clarify, by assuming quasi-steadiness, the instantaneous power can be calculated at any position along a trajectory. Jerez Venegas calculates the average cycle power with equation (2.8) (equation (6.2) in [18]), where P_i is the instantaneous power at each time step i. Unfortunately, the thesis does not explain how the position, and thus the instantaneous power, at each time step is determined. This omission prompts questions about how variations in kite speed along the trajectory affect the cycle power and the flight path optimization.

$$\bar{P} = \frac{1}{T} \sum i = 0^N P_i \tag{2.8}$$

Wind farm layout optimization by Johnson, 2019

Yet another complicated research question was approached using QSM by Johnson [19]. Johnson investigated the optimal layout of a farm consisting of pumping cycle AWE systems, in which each system was assigned an unique flight path to maximize the power density of the wind farm.

Johnson modeled the power produced by each flight path with quasi-steady model, similar to Noom's model discussed in section 2.2.1, but with all inertial forces discarded. A parameterized Lissajous figure-eight flight path was imposed, and the same forward Euler scheme as Noom's, equation (2.5), was used to integrate the position. This means that Johnson's model contains the same model errors as Noom's. Johnshon verified each path's feasibility with empirically obtained turn rate limits.

Using this model, Johnson showed that increasing the number of kites yields better power levelization, and that the path azimuth and elevation angles of each system should be carefully considered to optimize the farm's power yield. In general, an upwind kite elevation higher than that of the downwind units was beneficial. Johnson demonstrated that QSM could be effectively applied to the complex problem of optimizing a pumping cycle AWE system farm.

Assigning a unique flight path to each kite, drastically increased the complexity of the optimization problem. Therefore, the need of an efficient model and with that, the versatility of QSM is once more reiterated.

Wind profile clustering to estimate annual energy production

Schelbergen et al. showcased the versatility of quasi-steady modeling in the context of AWE once more in their study of 2020 [20]. They presented a method to efficiently predict the annual energy production (AEP), through clustering of wind profiles.

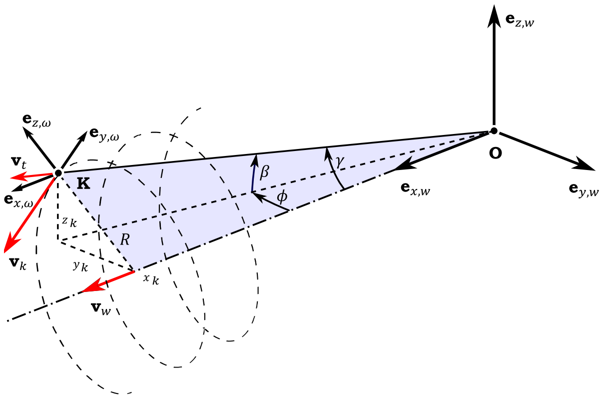

Figure 2.2: The downwind helical flight path for which Talmar derived an analytical tether force solution [21].

Schelbergen et al. reasoned that because typical AWE systems operate at altitudes $z > 150\,$m, substantial uncertainties are introduced when using the wind profile power law or logarithmic law: these relationships are not strictly valid beyond the surface layer of the atmospheric boundary layer. They further argued that these methods do not provide information about any wind direction dependence with height, or the presence of lower-level wind speed maxima. Following these arguments, they proposed a clustering procedure for representing wind profile shapes, that include the vertical variation of both wind speed and direction, based on measured or modelled data.

Using a k-means clustering approach, Schelbergen et al. demonstrated that the accuracy of a representation with three of more clusters is already greater than that of the a logarithmic representation, for the used DOWA data set. Through use of the quasi-steady model by Van Der Vlugt et al. [15], to be further discussed in section 2.2.2, power curves of a pumping cycle AWE system were determined for the various wind clusters. By clustering, the number of optimizations required to obtain the AEP was reduced from 8760 for an hourly brute-force calculation, to only 100 for a four-cluster representation with 25 optimizations per cluster. Thus, AEP estimation using clusters was roughly two orders of magnitude faster.

Schelbergen et al. demonstrated that the use of quasi-steady modeling extends beyond the general use case of flight simulation. Having an efficient model to predict the power production of a pumping cycle AWE system also enables the exploration of other complex questions, such as the development of an efficient wind resource model specifically tailored to such systems.

2.2.4. Analytical solution for a quasi-steady helical path

In the 2021 master's thesis by Talmar [21], the role of the inertial forces in a pumping cycle AWE system was studied. Talmar derived analytical dynamic equilibrium solutions and compared the results to the aforementioned inertia-free model by Van Der Vlugt et al.

Two special cases were considered: a downwind circular flight path and a downwind helical flight path. In both cases, the kite speed was assumed constant, resulting in an asymptotic solution (no transient response). Figure 2.2 shows such downwind helical path: the helix axis is aligned with the wind vector, and the kite is reeled out such that the wind-aligned reeling factor f_x is constant. As the helix radius R is constant, the cone angle γ decreases for increasing distance between the kite and ground station. Ignoring gravity, Talmar shows that the tether tension F_t for the helical path becomes equation (2.9) (eq. 3.38 in [21]). The circular path tether tension is obtained by setting $f_x = 0$.

$$F_{t_{\text{helix}}} = \frac{1}{(1-f_x)\cos\gamma}\frac{\rho S C_L v_w^2}{2E}\left[\lambda^2 + (1-f_x)^2\right]^{\frac{3}{2}} \tag{2.9}$$

Equation (2.9) was then used to investigate the role of the inertial forces in these special flight cases. The gravity force was removed from the inertia-free model by Van Der Vlugt et al., to allow a fair comparison between the obtained tether forces and traction powers. The error in traction power ranged between 1-2% for lightweight, soft kites.

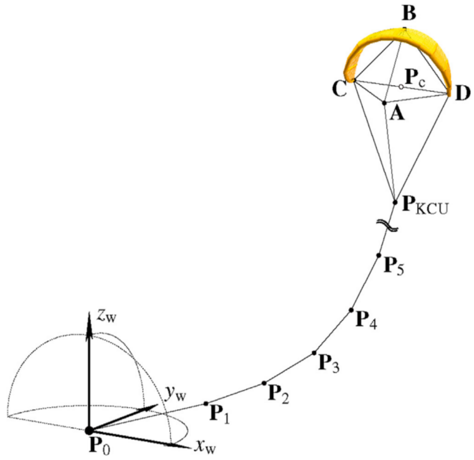

Figure 2.3: Lumped-mass tether with four-point kite model, by Fechner et al. [22]

2.3. Dynamic modeling

Quasi-steady models simplify the inertial effects present in the system and cannot resolve the hysteresis in the system response (e.g., the change in response to a change in initial conditions). A fully dynamic model must be used if such effects should be resolved. Dynamic models tailored to the application of pumping cycle AWE systems are relatively limited.

2.3.1. Dynamic model with realistic system components

Fechner et al. developed a fully dynamic model aimed at pumping cycle soft kite systems in 2015 [22]. By modeling each major system component with much more detail compared to previously discussed models, this model resolves the dynamics of all major components. The atmosphere, tether, kite and generator are modeled as follows.

- **Atmosphere**: The air density was modeled with the Stull's exponential law [16] and a weighting of the power and laws was used to obtain a velocity profile that matched measurements at three altitudes.
- **Tether**: The tether was modeled as a series of linked lumped-masses, as shown in figure 2.3. Each tether segment is subjected to a spring force, a damping force, and an aerodynamic drag force.
- **Kite**: The kite is modeled in two different ways: by a one-point mass and a four-point model. In the one-point model, kite steering input is modeled as a sideways force, in the four-point model, the kite is steered by varying the lengths between the four points, allowing for uncoordinated turns. In both models, the aerodynamic loads are quasi-steady: a linear function of the local angle of attack.
- **Ground station:** A realistic winch model was used, that resolved the drum inertial forces and generator torque. During the traction and retraction phases, the winch PID controller tracks set values for reeling speed and tether force, and soft transitions are implemented in the transition phases. The kite controller steers the kite towards Zenith in the transition and retraction phases and towards points left or right of the downwind vector in the traction phase.

Fechner et al. compared the model to flight data of the TU Delft HYDRA kite, and tuned the model steering parameters to let the simulated flight path resemble the measured flight path. They concluded that the model predicts a more realistic dynamic response to steering inputs then simpler models, and seems well suited for flight path optimization. The accuracy of the predicted power output was insufficiently validated.

3
Research design

This chapter sets an outline for the research conducted in this thesis. First, the research gaps are identified, after which the research objective and subsequent research questions are formulated. The chapter concludes by setting out the methodology that will be used to answer these research questions.

3.1. Need for research in the context of tethered flight dynamics

Following the discussion in chapter 2, several research gaps and challenges can be identified in the modeling techniques available for the dynamics of AWE systems.

3.1.1. Ambiguity in the definition of quasi-steadiness

The concept of quasi-steadiness lacks a universally accepted definition, leading to discrepancies in model formulations. For instance, Van Der Vlugt et al. assumes the absolute acceleration to be zero, whereas Noom only assumes the rate of change in the kite tangential and radial speed components to be zero. This lack of a consistent definition of quasi-steadiness means that validation studies are difficult to compare and complicates research progress.

3.1.2. Incomplete understanding of the impact of assuming quasi-steadiness

The role of the inertial forces in AWE systems, and thus the impact of assuming quasi-steadiness, remains poorly understood. Although Noom and Talmar argue that the influence of inertia on the generated power is small, both authors recommend further research.

Key questions about how the inertial effects scale with the increasing mass of airborne components and which inertial effects (e.g., Coriolis, centrifugal) are most significant, have yet to be answered. Considering that the validation study by Schelbergen and Schmehl in section 2.2.2 shows a relatively large error in the estimated power production for the inertia-free quasi-steady model by Van Der Vlugt et al, it is important to gain more insight in the impact of neglecting certain inertial terms. Better understanding of these impacts is key to developing better modeling techniques.

3.1.3. Limited availability of dynamic models

Dynamic models that accurately predict the power output are limited. Analytical solutions, such as those proposed by Talmar, are applicable to specific flight cases only, and may not extend well to general flight cases. The numerical model by Fechner can be used to simulate realistic system dynamics, but requires extensive tuning of model parameters. Also, quasi-steady models seem to outperform this model in terms of accuracy in power generation. Obtaining a robust dynamic model that accurately predicts the power output is key to understanding the role of inertial forces in crosswind tethered flight.

3.1.4. Lack of tailored dynamic equations of motion

The equations of motion solved by the models discussed in chapter 2 are typically expressed in difficult-to-interpret state variables. Note for example Noom's quasi-steady polar angular acceleration and quasi-steady azimuth angular acceleration in equations (2.1) and (2.2) respectively, which must be substituted into the even more complicated inertial force equation (2.3). More intuitive would be to express the dynamic equations of motion in terms of state variables relevant to crosswind tethered flight.

For example, the kite velocity can be expressed in terms of the tangential speed, radial speed, and course angle, instead of the rate of change of the polar and azimuth angles. Expressing the system dynamics in such state variables specifically tailored to crosswind tethered flight would make the equations of motion easier to interpret. This, in turn, would help model verification and validation.

3.1.5. Simplistic path control techniques

Current models employ relatively simplistic methods to simulate the traction force as a consequence of a prescribed flight path. For example, the method used by Noom and Johnson to integrate the position along a parameterized path, does not account for changes in speed along the path, as well as the sphericality of the path. And although Venegaz and Fechner implemented realistic controllers, these cannot be used to obtain the exact tether force from a prescribed path: the flown path will always differ from the prescribed path if a controller is used. Obtaining a path control technique that accounts for the system dynamics is essential to understanding the importance of resolving these dynamics.

3.2. Research objectives and questions

The identified modeling challenges regarding the dynamics of crosswind tethered flight form the starting point of this thesis. This thesis aims to advance the understanding of crosswind tethered flight dynamics, by assessing the impact of assuming quasi-steadiness. The main research question is formulated as such:

1. What is the impact of assuming quasi-steadiness on the predicted behavior of a pumping cycle, soft kite system?

Answering this question is hindered by the challenges in section 3.1. A clear definition of quasi-steadiness is required, and tailoring the equations of motion to crosswind tethered flight, aids model verification. Also, to make a fair comparison between models, a path-control method is required that consistently resolves the relevant path curvature and kite dynamics. Subsequent research questions that will be answered in this thesis are:

2. What should be the definition of quasi-steadiness, in the context of crosswind tethered flight dynamics?
3. How can the dynamics of crosswind tethered flight be expressed in terms of state variables relevant to this application?
4. How does the impact of the different inertial effects scale with varying system properties?
5. What is the effect of resolving the inertial effects at different degrees of complexity on the model's efficiency and robustness?
6. How should a parameterized flight path be imposed to accurately solve the dynamic equations of motion?
7. How does accounting for the system dynamics when imposing a fight path affect the predicted power output?

Having answered these confining subquestions, an answer to the main research question can be formed, regarding the impact of assuming quasi-steadiness

3.3. Methodology

To investigate the impact of assuming quasi-steadiness, a dynamic model will be developed and compared to various quasi-steady models.

Chapter 4 derives the dynamic equations of motion in terms of state variables relevant to crosswind tethered flight. The first step is to identify these relevant state variables and to define useful reference frames. Having obtained the dynamic equations of motion, they are tweaked to provide a clear definitions of steady-state, quasi-steadiness and dynamic crosswind tethered flight, and the corresponding equations of motion are presented.

To be able to solve the equations of motion, a simple tether model and kite model are derived in chapter 5. The tether mass is lumped with the kite, and is assumed to be straight and rigid. Two formulations of tether drag are proposed: one which resolved the exponential drag distribution on the tether, another one in which the drag load is simplified to point load. The kite is modeled as a point mass and is assumed to operate with constant lift and drag coefficients.

Then, the method for imposing the parameterized path is derived in chapter 6. Two formulations and solution methods are proposed to solve the differential problem that is formed by the equations of motion. A state-space solution scheme to solve the second order initial value problem that is formed by the dynamic equations of motion is proposed, as well as a solution scheme that integrates the first-order differential equation formed by the steady and quasi-steady equations of motion.

Chapter 7 verifies the model framework, by performing unit tests and by comparing the dynamic model to Talmar's analytical solutions for the circular and helical flight paths.

Once the framework is sufficiently verified, the role of the inertial forces is assessed in chapter 8. The sensitivity to system quantities such as kite mass and aerodynamic coefficients is tested, as well as the sensitivity to the operational quantities such as the flight path curvature and reeling speed. Also, the impact of atmospheric unsteadiness, such as a nonuniform mean wind speed or turbulence is assessed.

Finally, the impact of resolving the inertial forces on the solution response in terms of average values, amplitudes and phases is concluded in chapter 9 and recommendations regarding future work or improvements to the current work are discussed in chapter 10.

4

Deriving equations of motion of tethered flight

As the kite is connected to the ground station by the tether, the position of the kite is most intuitively described in spherical coordinates. For example, the kite's position could be given as a triple of azimuth angle, elevation angle and radial distance. However, using the time derivatives of these spherical coordinates to describe the velocity, results in much more complicated equations, compared to using Cartesian coordinates.

The aim of this chapter is to derive equations of motion that describe the kite motion in an intuitive manner and to propose clear definitions of steady and quasi-steady flight, specifically tailored to tethered flight. To achieve this, let's start by defining convenient reference frames.

4.1. Reference frames

Throughout this report, three reference frames are used: the inertial wind reference frame W, the spherical azimuth-zenith-radial reference frame AZR and the course reference frame C. Each reference frame has its origin at the ground station point O_G.

4.1.1. Wind reference frame W

The wind reference frame (W-frame) is an inertial reference frame in which the position of a point k is expressed in Cartesian coordinates (x, y, z). The W-frame has its origin at the ground station point O_G and is oriented such that $\mathbf{e}_x$ unit vector is aligned with the mean wind speed vector at reference height. The $\mathbf{e}_z$ unit vector points vertically up from the Earth's surface. The W-frame is assumed to be inertial, that is, the effects of the Earth's rotation on the kite motion in this reference frame are neglected.

The position vector $\mathbf{r}_\mathrm{k}$ of a point k is thus given by equation (4.1).

$$\mathbf{r}_\mathrm{k} = x\mathbf{e}_x + y\mathbf{e}_y + z\mathbf{e}_z \tag{4.1}$$

4.1.2. Azimuth-Zenith-Radial reference frame AZR

The Azimuth-Zenith-Radial frame (AZR-frame) is a rotating reference frame in which the position of a point k is expressed in terms of the spherical coordinates (ϕ, β, r) with ϕ the azimuth angle, β the elevation angle β, r the radial distance.

Figure 4.1 shows the transformation between the W-frame and the AZR-frame. With $\mathbf{r}_\mathrm{k}$ the position vector of k, i.e. the line segment between k and O_G, then the radial distance coordinate r is equal to the length of $\mathbf{r}$. The elevation angle β is measured between the $\mathbf{e}_x, \mathbf{e}_y$-plane and $\mathbf{r}$ and the azimuth angle ϕ is measured between the $\mathbf{e}_x, \mathbf{e}_z$-plane and $\mathbf{r}$.

Introducing the unit vectors $\mathbf{e}_\phi, \mathbf{e}_\beta, \mathbf{e}_\mathrm{r}$ as shown in figure 4.1, the position of k in the AZR-frame is expressed only in terms of distance r along unit vector $\mathbf{e}_\mathrm{r}$ (equation (4.2)).

$$\mathbf{r}_\mathrm{k} = r\mathbf{e}_\mathrm{r} \tag{4.2}$$

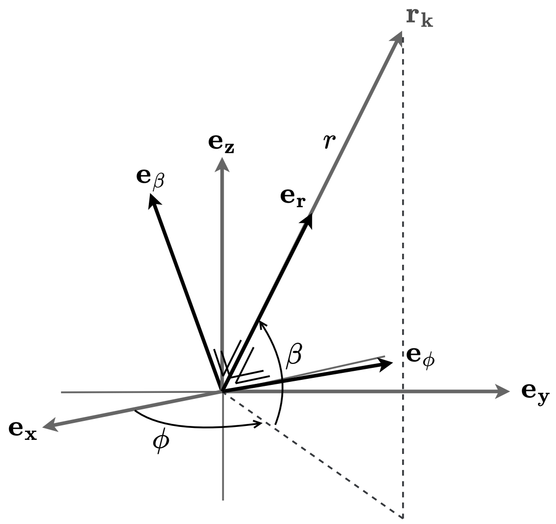

Figure 4.1: Azimuth-Zenith-Radial reference frame AZR unit vectors $\mathbf{e}_\chi, \mathbf{e}_\mathrm{n}, \mathbf{e}_\mathrm{r}$ originating from rotating the W-frame.

The transformation matrix $\mathbb{T}_{AZR\leftarrow W}$ (read: AZR from W) that relates the AZR-frame unit vectors $\mathbf{e}_\phi, \mathbf{e}_\beta, \mathbf{e}_\mathrm{r}$ to the W-frame unit vectors is given by equation (4.4). This transformation is the result of two subsequent transformations. The first transformation, a rotation of magnitude $\phi + \frac{\pi}{2}$ around $\mathbf{e}_z$, is denoted as $\mathbb{T}_z(\phi + \frac{\pi}{2})$. The second transformation is a rotation of magnitude $\frac{\pi}{2} - \beta$ around $\mathbf{e}'_x$, denoted as $\mathbb{T}_{x'}(\frac{\pi}{2} - \beta)$. Here, the prime symbol $'$ indicates that the rotation is along the $\mathbf{e}_x$-vector of the subsequent frame W' and not the starting frame W. Note that the matrix multiplication is performed from right-to-left, explaining the seemingly reversed order of transformations in equation (4.4).

$$\begin{bmatrix} \mathbf{e}_\phi \\ \mathbf{e}_\beta \\ \mathbf{e}_\mathrm{r} \end{bmatrix} = \mathbb{T}_{AZR\leftarrow W} \begin{bmatrix} \mathbf{e}_x \\ \mathbf{e}_y \\ \mathbf{e}_z \end{bmatrix} \tag{4.3}$$

$$\begin{aligned} \mathbb{T}_{AZR\leftarrow W} &= \mathbb{T}_{x'}\left(\frac{\pi}{2} - \beta\right) \mathbb{T}_z\left(\phi + \frac{\pi}{2}\right) \\ &= \begin{bmatrix} 1 & 0 & 0 \\ 0 & \cos(\frac{\pi}{2} - \beta) & \sin(\frac{\pi}{2} - \beta) \\ 0 & -\sin(\frac{\pi}{2} - \beta) & \cos(\frac{\pi}{2} - \beta) \end{bmatrix} \begin{bmatrix} \cos(\phi + \frac{\pi}{2}) & \sin(\phi + \frac{\pi}{2}) & 0 \\ -\sin(\phi + \frac{\pi}{2}) & \cos(\phi + \frac{\pi}{2}) & 0 \\ 0 & 0 & 1 \end{bmatrix} \\ &= \begin{bmatrix} -\sin\phi & \cos\phi & 0 \\ -\sin\beta\cos\phi & -\sin\beta\sin\phi & \cos\beta \\ \cos\beta\cos\phi & \cos\beta\sin\phi & \sin\beta \end{bmatrix} \end{aligned} \tag{4.4}$$

The presented definition of coordinates ϕ, β, r is arguably the most intuitive right-handed spherical coordinate system possible, considering the application to AWE systems. By defining $\mathbf{e}_\mathrm{r}$ 'outwards', positive radial speed $\dot{r}$ translates to kite reel-out. Likewise, using elevation angle β instead of the polar angle often used in mathematical contexts, results in upward kite flight for a positive elevation rate $\dot{\beta}$. When regarding the sphere enclosed by a constant radius r as a 'small Earth', it becomes apparent that the presented AZR-frame with unit vectors $\mathbf{e}_\phi, \mathbf{e}_\beta, \mathbf{e}_\mathrm{r}$ is analogous to the East-North-Up reference frame often used in the context of orbital mechanics. This resemblance is the rationale behind the chosen order of notation of the AZR unit vectors.

4.1.3. Course reference frame C

The position of a point K is intuitively described in spherical coordinates (ϕ, β, r). However, representing the velocity $\mathbf{v}_\mathrm{k}$ using the time derivatives $(\dot{\phi}, \dot{\beta}, \dot{r})$ can be less intuitive. To address this, we introduce the course reference frame C in which the velocity is decomposed into a radial speed component v_r, a tangential speed v_τ within the plane τ tangential to the unit sphere, and a specific direction angle.

Thee C-frame has the unit vectors $\mathbf{e}_\chi, \mathbf{e}_\mathrm{n}, \mathbf{e}_\mathrm{r}$ as the basis vectors (read: course direction, normal direction, radial direction). The transformation that relates the C-frame to the AZR-frame consists of a rotation along the $\mathbf{e}_\mathrm{r}$ axis, in order to align the $\mathbf{e}_\chi$ axis with the tangential velocity component of K. That is, $\mathbf{e}_\chi$ is such that the kite velocity $\mathbf{r}_\mathrm{k}$ becomes equation (4.5).

$$\mathbf{v}_\mathrm{k} = v_\tau \mathbf{e}_\chi + v_r \mathbf{e}_\mathrm{r} \tag{4.5}$$

To intuitively quantify this rotation around $\mathbf{e}_\mathrm{r}$, we define the course angle χ such that $\chi = 0$ results in flight towards the Zenith, and that $0 \leq \chi \leq \pi$ results in a positive azimuth rate $\dot{\phi}$. One can observe that viewing the unit sphere as a 'small Earth', this definition of χ is analogous to a geographic compass heading where 0° points North and 90° points East. The required rotation along the $\mathbf{e}_\mathrm{r}$ axis then becomes $\frac{\pi}{2} - \chi$, resulting in the transformation $\mathbb{T}_{C\leftarrow AZR}$ given in equation (4.6). Consequently, the transformation $\mathbb{T}_{C\leftarrow W}$ becomes equation (4.7) and the C-frame unit vectors $\mathbf{e}_\chi, \mathbf{e}_\mathrm{n}, \mathbf{e}_\chi$ are obtained through equation (4.8). The C-frame unit vectors are displayed in figure 4.2.

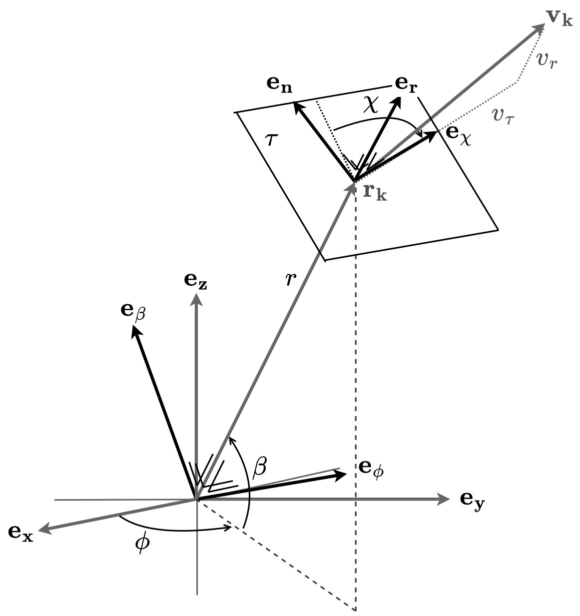

Figure 4.2: Unit vectors $\mathbf{e}_\chi, \mathbf{e}_\mathrm{n}, \mathbf{e}_\mathrm{r}$ of the course reference frame C, originating from rotating the AZR-frame around the $\mathbf{e}_\mathrm{r}$ axis $\frac{\pi}{2} - \chi$, with χ the course angle. For clarity, the C-frame basis vectors are drawn on the tangential plane τ, but its origin lies at the ground station O.

$$\mathbb{T}_{C\leftarrow AZR} = \mathbb{T}_r\left(\frac{\pi}{2} - \chi\right) = \begin{bmatrix} \sin\chi & \cos\chi & 0 \\ -\cos\chi & \sin\chi & 0 \\ 0 & 0 & 1 \end{bmatrix} \tag{4.6}$$

$$\begin{aligned} \mathbb{T}_{C\leftarrow W} &= \mathbb{T}_{C\leftarrow AZR}\mathbb{T}_{AZR\leftarrow W} \\ &= \begin{bmatrix} -\sin\chi\sin\phi - \cos\chi\sin\beta\cos\phi & \sin\chi\cos\phi - \cos\chi\sin\beta\sin\phi & \cos\chi\cos\beta \\ \cos\chi\sin\phi - \sin\chi\sin\beta\cos\phi & -\cos\chi\cos\phi - \sin\chi\sin\beta\sin\phi & \sin\chi\cos\beta \\ \cos\beta\cos\phi & \cos\beta\sin\phi & \sin\beta \end{bmatrix} \end{aligned} \tag{4.7}$$

$$\begin{bmatrix} \mathbf{e}_\chi \\ \mathbf{e}_\mathrm{n} \\ \mathbf{e}_\mathrm{r} \end{bmatrix} = \mathbb{T}_{C\leftarrow AZR} \begin{bmatrix} \mathbf{e}_\phi \\ \mathbf{e}_\beta \\ \mathbf{e}_\mathrm{r} \end{bmatrix} = \mathbb{T}_{C\leftarrow W} \begin{bmatrix} \mathbf{e}_x \\ \mathbf{e}_y \\ \mathbf{e}_z \end{bmatrix} \tag{4.8}$$

4.2. Translational motion in the course reference frame

Newton's second law of motion states that the absolute acceleration $\frac{d^2\mathbf{r}_\mathrm{k}}{dt^2}$ of a point k is equal to the sum of forces acting upon k, divided its mass m. With the position vector $\mathbf{r}_\mathrm{k}$ of k expressed in Cartesian coordinates by equation (4.9), the absolute acceleration simply becomes equation (4.10).

$$\mathbf{r}_\mathrm{k} = x\mathbf{e}_x + y\mathbf{e}_y + z\mathbf{e}_z \tag{4.9}$$

$$\frac{d^2\mathbf{r}_\mathrm{k}}{dt^2} = \frac{d^2x}{dt^2}\mathbf{e}_x + \frac{d^2y}{dt^2}\mathbf{e}_y + \frac{d^2z}{dt^2}\mathbf{e}_z \tag{4.10}$$

As discussed before, the position of a kite is most intuitively expressed in spherical coordinates (ϕ, β, r), and the velocity is conveniently expressed in the state variables tangential velocity v_τ, reeling speed v_r and course angle χ. The question arises: how to express the absolute acceleration $\frac{d^2\mathbf{r}_\mathrm{k}}{dt^2}$ in terms of these state variables, that is, how to express $\frac{d^2\mathbf{r}_\mathrm{k}}{dt^2}$ in the C-frame basis vectors?

4.2.1. Velocity in the course reference frame

From before, we have the position vector $\mathbf{r}_\mathrm{k}$ for a point k in the rotating course reference frame in equation (4.2). By applying the product rule, the velocity vector $\frac{d\mathbf{r}_\mathrm{k}}{dt}$ becomes equation (4.11).

$$\mathbf{r}_\mathrm{k} = r\mathbf{e}_\mathrm{r} \tag{4.2}$$

$$\frac{d\mathbf{r}_\mathrm{k}}{dt} = \frac{dr}{dt}\mathbf{e}_\mathrm{r} + r\frac{d\mathbf{e}_\mathrm{r}}{dt} \tag{4.11}$$

The left term in equation (4.11) is equal to the relative velocity of k in the course frame, because $\mathbf{e}_\mathrm{r}$ always points to k. Denoting the relative velocity as $\left[\frac{d\mathbf{r}_\mathrm{k}}{dt}\right]$ results in equation (4.12). Furthermore, the time derivative of a vector is equal to the cross product of its rotation vector $\mathbf{\Omega}$ with the vector itself (see Section 4.9, p171 in Goldstein [23]), giving equation (4.13).

$$\frac{dr}{dt}\mathbf{e}_\mathrm{r} \equiv \left[\frac{d\mathbf{r}_\mathrm{k}}{dt}\right] \tag{4.12}$$

$$\frac{d\mathbf{e}}{dt} = \mathbf{\Omega} \times \mathbf{e} \tag{4.13}$$

Substituting equations (4.12) and (4.13) into equation (4.11) gives the absolute velocity vector $\frac{d\mathbf{r}_\mathrm{k}}{dt}$ expressed in C-frame unit vectors in equation (4.14). Here, $\mathbf{\Omega}_C$ is the rotation vector of the course reference frame with respect to the inertial reference frame.

$$\frac{d\mathbf{r}_\mathrm{k}}{dt} = \left[\frac{d\mathbf{r}_\mathrm{k}}{dt}\right] + \mathbf{\Omega}_C \times \mathbf{r}_\mathrm{k} \tag{4.14}$$

4.2.2. Acceleration in the course reference frame

To express the acceleration of k in terms of C-frame unit vectors, equation (4.11) is differentiated with respect to time once more. Applying the product rule and chain rule gives:

$$\frac{d^2\mathbf{r}_\mathrm{k}}{dt^2} = \frac{d^2r}{dt^2}\mathbf{e}_\mathrm{r} + 2\frac{dr}{dt}\frac{d\mathbf{e}_\mathrm{r}}{dt} + r\frac{d^2\mathbf{e}_\mathrm{r}}{dt^2}$$

Which, after substituting equation (4.13) and introducing the relative acceleration $\left[\frac{d^2\mathbf{r}_\mathrm{k}}{dt^2}\right]$, results in the absolute acceleration $\frac{d^2\mathbf{r}_\mathrm{k}}{dt^2}$ in terms of C-frame unit vectors in equation (4.15).

$$\frac{d^2\mathbf{r}_\mathrm{k}}{dt^2} = \left[\frac{d^2\mathbf{r}_\mathrm{k}}{dt^2}\right] + 2\mathbf{\Omega}_C \times \left[\frac{d\mathbf{r}_\mathrm{k}}{dt}\right] + \mathbf{\Omega}_C \times (\mathbf{\Omega}_C \times \mathbf{r}_\mathrm{k}) + \frac{d\mathbf{\Omega}_C}{dt} \times \mathbf{r}_\mathrm{k} \tag{4.15}$$

Equation (4.15) shows that the absolute acceleration of k is a summation of the relative acceleration of k, the Coriolis acceleration, the centrifugal acceleration and the Euler acceleration, with:

$\rightarrow \left[\frac{d^2\mathbf{r}_\mathsf{k}}{dt^2}\right]$	The relative acceleration of k with respect to reference frame C.
$\rightarrow 2\mathbf{\Omega}_C \times \left[\frac{d\mathbf{r}_\mathsf{k}}{dt}\right]$	The Coriolis acceleration due to the relative velocity of k in C.
$\rightarrow \mathbf{\Omega}_C \times (\mathbf{\Omega}_C \times \mathbf{r}_\mathsf{k})$	The centrifugal acceleration due to the angular motion of C.
$\rightarrow \frac{d\mathbf{\Omega}_C}{dt} \times \mathbf{r}_\mathsf{k}$	The Euler acceleration, that is the apparent (tangential) acceleration due to the variation in angular velocity of C.

Unfortunately, equation (4.15) is not yet very useful: an expression for the rotation vector $\mathbf{\Omega}_C$ in terms of convenient state variables must first be derived. From before, we have that the velocity $\frac{d\mathbf{r}_\mathsf{k}}{dt}$ is given by equation (4.5). Also, by definition of the course reference frame transformation in section 4.1, $\mathbf{\Omega}_C$ is given by in equation (4.16).

$$\frac{d\mathbf{r}_\mathsf{k}}{dt} = v_\tau \mathbf{e}_\chi + v_r \mathbf{e}_\mathsf{r} \tag{4.5}$$

$$\mathbf{\Omega}_C = \dot{\phi}\mathbf{e}_z - \dot{\beta}\mathbf{e}_\phi - \dot{\chi}\mathbf{e}_\mathsf{r} \tag{4.16}$$

Substituting the transformations for $\mathbf{e}_z, \mathbf{e}_\phi, \mathbf{e}_\mathsf{r}$ given in equation (4.3) into equation (4.16) gives the rotation vector $\mathbf{\Omega}_C$ in terms of C-frame unit vectors (equation (4.17)).

$$\begin{aligned} \mathbf{\Omega}_C &= \dot{\phi}\begin{bmatrix}\cos\chi\cos\beta\\ \sin\chi\cos\beta\\ \sin\beta\end{bmatrix} - \dot{\beta}\begin{bmatrix}\sin\chi\\ -\cos\chi\\ 0\end{bmatrix} - \dot{\chi}\begin{bmatrix}0\\0\\1\end{bmatrix} \\ &= \begin{bmatrix}\dot{\phi}\cos\chi\cos\beta - \dot{\beta}\sin\chi\\ \dot{\phi}\sin\chi\cos\beta + \dot{\beta}\cos\chi\\ \dot{\phi}\sin\beta - \dot{\chi}\end{bmatrix}^{\chi,n,r} \end{aligned} \tag{4.17}$$

Now, two expressions for $\mathbf{\Omega}_C \times \mathbf{r}_\mathsf{k}$ can be obtained: one by using equation (4.2) and equation (4.17), the other by substituting the kinematic constraint in equation (4.5) into equation (4.14):

$$\begin{aligned} \mathbf{\Omega}_C \times \mathbf{r}_\mathsf{k} &= r\begin{bmatrix}\dot{\phi}\sin\chi\cos\beta + \dot{\beta}\cos\chi\\ \dot{\beta}\sin\chi - \dot{\phi}\cos\chi\cos\beta\\ 0\end{bmatrix}^{\chi,n,r} \\ &= \frac{d\mathbf{r}_\mathsf{k}}{dt} - \left[\frac{d\mathbf{r}_\mathsf{k}}{dt}\right] = \begin{bmatrix}v_\tau\\0\\0\end{bmatrix}^{\chi,n,r} \end{aligned}$$

From this system of equations, we obtain the expressions for $\dot{\phi}$, $\dot{\beta}$ and χ in equations (4.18) to (4.20). Equation (4.20) is a logical result: χ follows from the ratio between the velocity towards the azimuth and the velocity towards the zenith in the tangential plane τ. The cosine term appears because the azimuth rate $\dot{\phi}$ is measured along $\mathbf{e}_z$ instead of $\mathbf{e}_\beta$.

$$\dot{\phi} = \frac{v_\tau \sin\chi}{r\cos\beta} \tag{4.18}$$

$$\dot{\beta} = \frac{v_\tau \cos\chi}{r} \tag{4.19}$$

$$\tan\chi = \frac{\dot{\phi}\cos\beta}{\dot{\beta}} \tag{4.20}$$

The rotation vector $\mathbf{\Omega}_C$ can now be expressed in state variables v_τ, v_r, course angle χ and the course angle rate $\dot{\chi}$, through substitution of equations (4.18) and (4.19) into equation (4.17).

$$\mathbf{\Omega}_C = \begin{bmatrix}\frac{v_\tau}{r}\sin\chi\cos\chi - \frac{v_\tau}{r}\sin\chi\cos\chi\\ \frac{v_\tau}{r}\sin^2\chi + \frac{v_\tau}{r}\cos^2\chi\\ \frac{v_\tau}{r}\sin\chi\tan\beta - \dot{\chi}\end{bmatrix}^{\chi,n,r} = \begin{bmatrix}0\\ \frac{v_\tau}{r}\\ \frac{v_\tau}{r}\sin\chi\tan\beta - \dot{\chi}\end{bmatrix}^{\chi,n,r} \tag{4.21}$$

The relative acceleration, the Coriolis acceleration, and the centrifugal acceleration, become respectively equations (4.22) to (4.24). The Euler acceleration in equation (4.25) is calculated after substituting equation (4.21) into equation (4.13).

$$\left[\frac{d^2\mathbf{r}_\mathrm{k}}{dt^2}\right] = \begin{bmatrix} 0 \\ 0 \\ \dot{v}_r \end{bmatrix}^{\chi,n,r} \tag{4.22}$$

$$2\boldsymbol{\Omega}_C \times \left[\frac{d\mathbf{r}_\mathrm{k}}{dt}\right] = \begin{bmatrix} 2\frac{v_\tau v_r}{r} \\ 0 \\ 0 \end{bmatrix}^{\chi,n,r} \tag{4.23}$$

$$\boldsymbol{\Omega}_C \times (\boldsymbol{\Omega}_C \times \mathbf{r}_\mathrm{k}) = \begin{bmatrix} 0 \\ \frac{v_\tau^2}{r}\sin\chi\tan\beta - v_\tau\dot{\chi} \\ -\frac{v_\tau^2}{r} \end{bmatrix}^{\chi,n,r} \tag{4.24}$$

$$\begin{aligned}
\frac{d\boldsymbol{\Omega}_C}{dt} \times \mathbf{r}_\mathrm{k} &= \left(\left[\frac{d\boldsymbol{\Omega}_C}{dt}\right] + \boldsymbol{\Omega}_C \times \boldsymbol{\Omega}_C\right) \times \mathbf{r}_\mathrm{k} \\
&= \left(\left[\frac{d\boldsymbol{\Omega}_C}{dt}\right] + \mathbf{0}\right) \times \mathbf{r}_\mathrm{k} \\
&= \begin{bmatrix} 0 \\ \frac{\dot{v}_\tau}{r} - \frac{v_\tau v_r}{r^2} \\ \frac{d}{dt}\left(\frac{v_\tau}{r}\sin\chi\tan\beta - \dot{\chi}\right) \end{bmatrix} \times \begin{bmatrix} 0 \\ 0 \\ r \end{bmatrix} \\
&= \begin{bmatrix} \dot{v}_\tau - \frac{v_\tau v_r}{r} \\ 0 \\ 0 \end{bmatrix}^{\chi,n,r}
\end{aligned} \tag{4.25}$$

Finally, the absolute acceleration $\frac{d^2\mathbf{r}_\mathrm{k}}{dt^2}$ is obtained in terms of C-frame unit vectors and state variables, through substitution of equations (4.22) to (4.25), into equation (4.15).

$$\frac{d^2\mathbf{r}_\mathrm{k}}{dt^2} = \begin{bmatrix} \dot{v}_\tau + \frac{v_\tau v_r}{r} \\ \frac{v_\tau^2}{r}\sin\chi\tan\beta - v_\tau\dot{\chi} \\ \dot{v}_r - \frac{v_\tau^2}{r} \end{bmatrix}^{\chi,n,r} \tag{4.26}$$

4.3. Equations of motion in the course reference frame

With the absolute acceleration in the C-frame given by equation (4.26), various equilibria can be defined in this reference frame. The aim of this section is to propose a set of equilibrium definitions, to promote consistent usage of the terms 'steady' and 'quasi-steady' in the context of AWE.

4.3.1. Dynamic equilibrium

First, let us obtain the dynamic equilibrium equations. From Newton's second law, we have that dynamic translational motion of a kite with point mass m, upon which the external forces acting consist of the aerodynamic force $\mathbf{F}_\mathrm{a}$, the tether force $\mathbf{F}_\mathrm{t}$ and the gravity force $\mathbf{F}_\mathrm{g}$, is given by equation (4.27). Here, F_χ, F_n and F_r are total force components of the external forces in the $\mathbf{e}_\chi$, $\mathbf{e}_\mathrm{n}$, and $\mathbf{e}_\mathrm{r}$ directions, respectively.

$$\begin{aligned}
m\frac{d^2\mathbf{r}_\mathrm{k}}{dt^2} &= \mathbf{F}_\mathrm{a} + \mathbf{F}_\mathrm{t} + \mathbf{F}_\mathrm{a} \\
&= F_\chi\mathbf{e}_\chi + F_n\mathbf{e}_\mathrm{n} + F_r\mathbf{e}_\mathrm{r}
\end{aligned} \tag{4.27}$$

Substituting equation (4.26) into equation (4.27) allows the dynamic equilibrium equations (4.28) to (4.30) to describe the acceleration terms $\dot{v}_\tau$, $\dot{v}_r$, and $\dot{\chi}$ elegantly in terms of the external force components, the spherical position coordinates, the tangential and radial velocity components v_τ, v_r and finally the course angle χ.

$$\dot{v}_\tau = \frac{F_\chi}{m} - \frac{v_\tau v_r}{r} \tag{4.28}$$

$$v_\tau \dot{\chi} = \frac{v_\tau^2}{r} \sin\chi \tan\beta - \frac{F_n}{m} \tag{4.29}$$

$$\dot{v}_r = \frac{F_r}{m} + \frac{v_\tau^2}{r} \tag{4.30}$$

Equations (4.28) to (4.30) thus describe the kite motion as a system of mixed order coupled differential equations with 3 degrees of freedom (DOF). The three degrees of freedom are the kite motion in the course direction, the radial direction and the course angle itself. Equations (4.28) and (4.30) are second order differential equations, whereas equation (4.29) is a first order equation. A model that solves this system of dynamic equations could resolve all unsteady effects mentioned in table 1.1, provided that sufficiently detailed kite, tether and atmospheric models are used.

4.3.2. Inertia-free equilibrium

Reducing the order of the differential equations of motion allows for simulating kite motion in an efficient manner, as already mentioned in section 2.2. Van Der Vlugt et al. achieved this with their QSM by assuming that all inertial force contributions are zero, resulting in equation (4.31). This corresponds to equation (31) in [15]. Although the authors refer to this equilibrium as quasi-steady, a more descriptive term might be 'inertia-free'. To promote usage of clear terminology, this report will thus use 'inertia-free' to describe the equilibrium in equation (4.31).

$$\mathbf{F}_\mathrm{a} + \mathbf{F}_\mathrm{t} + \mathbf{F}_\mathrm{g} = \mathbf{0} \tag{4.31}$$

The inertia-free assumption originates from the notion that the airborne mass is small compared to the aerodynamic force acting upon the kite system, and that the tether length is relatively long. Van Der Vlugt et al. argue that in this case, the omission of the inertial forces caused by the kite's acceleration only results in a small change in the magnitude of the external loads, thereby justifying this simplification.

A model that solves the inertia-free equilibrium equation equation (4.31) could only resolve the unsteady effects in table 1.1 to a certain extent, as all inertial forces are neglected.

4.3.3. Steady equilibrium

Another equilibrium state that results in an order reduction of the dynamic equations of motion, is that of steady flight. Although section 1.2 already discussed that crosswind tethered flight is inherently unsteady, defining steadiness helps to eventually formulate the definition of quasi-steady flight.

In conventional atmospheric flight dynamics, a steady flight state is often interpreted as a state in which the aircraft's motion, the aerodynamic field and gravity are constant in a body reference frame. This definition is proposed by Etkin in the 1972 book 'Dynamics of Atmospheric Flight' [24]. In the context of tethered flight, this steady state condition can only be satisfied under certain conditions, because of the motion constraining tether.

More specifically, the tether forces the kite to revolve around the ground station. Therefore, the condition of constant kite motion, aerodynamic field and gravity is only satisfied when the kite's course angle is constant and its tangential speed is zero. In practice, such steady state realistically only happens during the final portion of the reel-in phase, i.e. between t_2 and t_3 in figure 4.3. Schmehl et al. refer to this steady reel-in state as an asymptotic limit state, which is not necessarily reached [25].

Mathematically, a steady state is thus constrained by the condition in equation (4.32). Substituting this condition into the absolute acceleration equation (4.26), the resulting steady state force equilibrium becomes the same as the inertia-free equilibrium in equation (4.31).

$$v_\tau = \dot{\chi} = \dot{v}_\tau = \dot{v}_r = 0 \tag{4.32}$$

4.3.4. Quasi-steady equilibrium

The steady-state condition in equation (4.32) isn't particularly useful in the context of crosswind flight. During crosswind flight, v_τ is nonzero, and $\dot{\chi}$ varies throughout a crosswind maneuver. Thus, the steady-

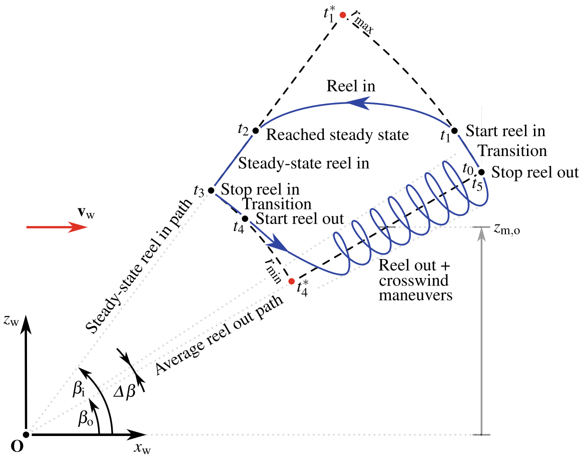

Figure 4.3: Realistically, a steady state in which the kite motion, aerodynamic field and gravity are constant in a body fixed reference frame, may occur only during reel-in. From Schmehl et al. [25].

state condition in equation (4.32) must be modified to obtain a more useful 'quasi-steady' equilibrium condition.

A useful definition of a quasi-steady state would be that in which the tangential speed and radial speeds are nonzero, but constant. This is the same as Noom's definition in his master thesis [14], which is also mentioned in the 2013 book 'Airborne Wind Energy' by Schmehl et al. [3]. If such state is stable, and any deviation from this state would decay sufficiently fast, one could model kite motion as a sequence of said quasi-steady states.

Thus, by assuming quasi-steadiness, it is assumed that any perturbations in the external forces result in an instantaneous change in kite speed. Such perturbations are for example the changes in the wind and gravity relative to the kite, as the kite moves along a trajectory. This results in the following definition of quasi-steadiness.

Definition: Quasi-Steadiness

Let K be a point with mass m, at a distance r from the origin O, and let the velocity of K be decomposed into tangential speed v_τ, radial speed v_r, and course angle χ. When K is in quasi-steady equilibrium, the *quasi-steady condition* is satisfied:

$$\dot{v}_\tau = \dot{v}_r = 0 \tag{4.33}$$

Consequently, the quasi-steady equilibrium equations in the course, normal and radial directions become respectively:

$$\frac{F_\chi}{m} = \frac{v_\tau v_r}{r} \tag{4.34}$$

$$\frac{F_n}{m} = \frac{v_\tau^2}{r} \sin\chi \tan\beta - v_\tau \dot{\chi} \tag{4.35}$$

$$\frac{F_r}{m} = -\frac{v_\tau^2}{r} \tag{4.36}$$

Comparing the quasi-steady equilibrium equations (4.34) to (4.36) to the inertia-free equilibrium equation (4.31), highlights some important differences between the two simplifications.

From a mathematical perspective, the external forces obtained from an inertia-free equilibrium are those required for the kite to hypothetically follow a rectilinear trajectory at a constant speed. In contrast, the external forces obtained from a quasi-steady equilibrium correspond to those required for the kite to hypothetically follow a curved trajectory at a constant speed, with this trajectory bound by a constant radial speed.

In terms of modeling, when kite motion is simulated under the inertia-free assumption, both the kite's speed and direction vary instantaneously with a change in the external forces. However, under the quasi-steady assumption, only the speed varies instantaneously with the external forces. The inertial forces caused by a change in direction, i.e. centrifugal forces, are resolved, as well as the Coriolis forces and part of the Euler forces. Thus considering the unsteady effects in table 1.1, the quasi-steady assumption allows to resolve more unsteady effects with greater detail, such as the centrifugal forces during a crosswind figure-eight maneuver, or the Coriolis forces due to the tether reeling motion.

By assuming quasi-steadiness, the second order differential equations (4.28) and (4.30) of dynamic motion in the course and radial directions are effectively reduced to first order equations. The inertial forces have become time-invariant, allowing for efficient simulation.

5
Modeling external loads on the kite

In chapter 4, the equations of motion for a point mass kite were derived in the C-frame. Equation (4.27) showed that the external loads acting on the kite consist of the gravity force $\mathbf{F}_\mathrm{g}$, the aerodynamic force $\mathbf{F}_\mathrm{a}$, and the tether force $\mathbf{F}_\mathrm{t}$. To simulate kite motion, we must express these forces in terms of the C-frame unit vectors and state variables.

For the gravity force $\mathbf{F}_\mathrm{g}$, this is straightforward as it is constant. By the transformation $\mathbb{T}_{P\leftarrow W}$ given in equation (4.7), $\mathbf{F}_\mathrm{g}$ is expressed in the C-frame by equation (5.1), where m is the kite mass and g is the gravitational acceleration.

$$\mathbf{F}_\mathrm{g} = -mg\mathbf{e}_z = -mg \begin{bmatrix} \cos\chi\cos\beta \\ \sin\chi\cos\beta \\ \sin\beta \end{bmatrix}^{\chi,n,r} \tag{5.1}$$

Expressing the tether force $\mathbf{F}_\mathrm{t}$ and aerodynamic force $\mathbf{F}_\mathrm{a}$ in terms of unit vectors $\mathbf{e}_\chi, \mathbf{e}_\mathrm{n}, \mathbf{e}_\mathrm{r}$ requires more work.

5.1. Tether force of an inertia-free, straight tether

A realistic tether can only be loaded axially and therefore deforms due to gravity, aerodynamic drag, and inertial forces. Modeling the deformation is complicated, and a straight tether is assumed. This results in tether loading in the directions of the tangential plane, as shown in the free body diagram in figure 5.1.

The task at hand is to find the expressions for the tether loading components at the suspension points. If it is assumed that the tether is inertia-free, the moment sum at the ground station is zero (equation (5.2)), meaning that the moment caused by the kite force on the tether $\mathbf{F}_\mathrm{k}$ cancels the moments $\mathbf{M}_g, \mathbf{M}_D$ caused by the tether gravity and tether drag respectively. Noting that the tether force on the kite $\mathbf{F}_\mathrm{t}$ is related to $\mathbf{F}_\mathrm{k}$ by equation (5.3), the implicit expression in equation (5.4) for the tether force $\mathbf{F}_\mathrm{t}$ is obtained.

$$\mathbf{0} = \mathbf{r}_\mathrm{k} \times \mathbf{F}_\mathrm{k} + \mathbf{M}_g + \mathbf{M}_D \tag{5.2}$$

$$\mathbf{F}_\mathrm{k} \equiv -\mathbf{F}_\mathrm{t} \tag{5.3}$$

$$\mathbf{r}_\mathrm{k} \times \mathbf{F}_\mathrm{t} = \mathbf{M}_g + \mathbf{M}_D \tag{5.4}$$

To find gravity moment $\mathbf{M}_g$, the tether density ρ_t is introduced as the tether mass per unit length l, such that the tether gravity differential $d\mathbf{F}_\mathrm{g}$ becomes equation (5.5). The gravity moment $\mathbf{M}_g$ (equation (5.6)) is then found by integrating the cross product between position vector $\mathbf{r}_\mathrm{k}$ and force differential $d\mathbf{F}_\mathrm{g}$.

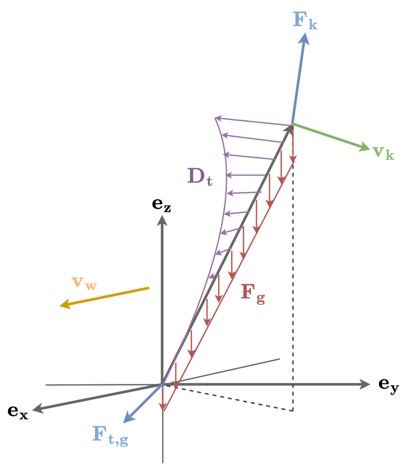

Figure 5.1: Free body diagram of a straight tether.

$$\begin{aligned} d\mathbf{F}_\mathrm{g} &= -\rho_t g dr \mathbf{e}_z \\ &= -\rho_t g \begin{bmatrix} \cos\chi\cos\beta \\ \sin\chi\cos\beta \\ \sin\beta \end{bmatrix}^{\chi,n,r} dl \end{aligned} \tag{5.5}$$

$$\begin{aligned} \mathbf{M}_g &= \int (\mathbf{r}_\mathrm{k} \times d\mathbf{F}_\mathrm{g}) \\ &= -\rho_t g \int_0^r \left(\begin{bmatrix} 0 \\ 0 \\ l \end{bmatrix} \times \begin{bmatrix} \cos\chi\cos\beta \\ \sin\chi\cos\beta \\ \sin\beta \end{bmatrix} \right) dl \\ &= \frac{\rho_t g}{2} r^2 \begin{bmatrix} \sin\chi\cos\beta \\ -\cos\chi\cos\beta \\ 0 \end{bmatrix}^{\chi,n,r} \end{aligned} \tag{5.6}$$

5.1.1. Tether force due to distributed tether drag load

To find drag moment $\mathbf{M}_D$, we note that the speed at any point in the straight tether is linearly related to the kite velocity components v_τ and v_r. Again using l as the local tether length coordinate, we obtain the local apparent wind velocity function $\mathbf{v}'_a$, in equation (5.7), where $\mathbf{v}_t$ is the local tether velocity.

$$\begin{aligned} \mathbf{v}'_a &= \mathbf{v}_\mathrm{w} - \mathbf{v}_t \\ &= \begin{bmatrix} v_{w,\chi} \\ v_{w,n} \\ v_{w,r} \end{bmatrix} - \begin{bmatrix} \frac{v_\tau l}{r} \\ 0 \\ v_r \end{bmatrix} \\ &= \begin{bmatrix} v_{w,\chi} - \frac{v_\tau l}{r} \\ v_{w,n} \\ v_{w,r} - v_r \end{bmatrix}^{\chi,n,r} \end{aligned} \tag{5.7}$$

Introducing the tether diameter d_t and the tether drag coefficient $C_{D,t}$, and defining the local apparent wind speed v'_a per equation (5.8), yields the drag force differential $d\mathbf{D}_t$ in equation (5.9). The drag moment is found by evaluating the cross product between the position and drag vectors, as shown in equation (5.10).

$$v'_a \equiv \|\mathbf{v}'_a\| \tag{5.8}$$

$$\begin{aligned} d\mathbf{D}_t &= \frac{\rho C_{D,t} d_t}{2} \|\mathbf{v}'_a\| \mathbf{v}'_a dl \\ &= \frac{\rho C_{D,t} d_t}{2} v'_a \begin{bmatrix} v_{w,\chi} - \frac{v_\tau l}{r} \\ v_{w,n} \\ v_{w,r} - v_r \end{bmatrix}^{\chi,n,r} dl \end{aligned} \tag{5.9}$$

$$\begin{aligned} \mathbf{M}_D &= \int (\mathbf{r}_\mathsf{k} \times d\mathbf{D}_t) \\ &= \frac{\rho C_{D,t} d_t}{2} \int_0^r v'_a \begin{bmatrix} -l v_{w,n} \\ v_{w,\chi} l - \frac{v_\tau l^2}{r} \\ 0 \end{bmatrix} dl \end{aligned} \tag{5.10}$$

Evaluating the integral in equation (5.10) could be done analytically when the wind velocity $\mathbf{v}_\mathsf{w}$ is constant, but a numerical method allows to integrate for e.g., a logarithmic wind profile. Substituting the gravity moment (equation (5.6)) and drag moment (equation (5.10)) into the inertia-free moment equilibrium (equation (5.4)), gives the tether force components at the kite $F_{t,\tau}$ and $F_{t,n}$ per equations (5.11) and (5.12).

$$F_{t,\tau} = -r\frac{\rho_t g}{2} \cos\chi \cos\beta + \frac{\rho C_{D,t} d_t}{2r^2} \int_0^r v'_a l (v_{w,\chi} r - v_\tau l) dl \tag{5.11}$$

$$F_{t,n} = -r\frac{\rho_t g}{2} \sin\chi \cos\beta + \frac{\rho C_{D,t} d_t}{2r} \int_0^r v_{w,n} v'_a l dl \tag{5.12}$$

The radial tether force component at the ground station is related to the radial tether force component at the kite through equation (5.13).

$$\mathbf{F}_{tg} = \mathbf{F}_\mathsf{k} + \mathbf{F}_\mathsf{g} + \int_0^r d\mathbf{D}_t \tag{5.13}$$

$$F_{tg,r} = -F_{t,r} - \rho_t g \sin\beta + \frac{\rho C_{D,t} d_t}{2} \int_0^r v'_a (v_{w,r} - v_r) dl \tag{5.14}$$

5.1.2. Tether force due to simplified tether drag

Alternatively, the tether drag can be approximated by assuming that the tether drag acts as a force at the kite, in the direction of the apparent wind velocity. This simplification, given in equation (5.15), was used by Van Der Vlugt et al. in [15]. The drag moment then becomes equation (5.16).

$$\mathbf{D}_t = \frac{1}{8} \rho d_t r C_{D,c} v_a \mathbf{v}_\mathsf{a} \tag{5.15}$$

$$\mathbf{M}_D = \mathbf{r}_\mathsf{k} \times \mathbf{D}_t = \frac{1}{8} \rho d_t r^2 C_{D,c} v_a \begin{bmatrix} -v_{w,n} \\ v_{w,\chi} - v_\tau \\ 0 \end{bmatrix}^{\chi,n,r} \tag{5.16}$$

Again substituting equation (5.6) and equation (5.16) yields the gives the tether force components at the kite $F_{t,\tau}$ and $F_{t,n}$, shown in equations (5.17) and (5.18). Calculating the force sum gives the radial component of the tether force at the ground station $F_{tg,r}$ in equation (5.19). One can see the similarity between the full straight tether force equations (5.11) to (5.13) and the simplified straight tether force equations (5.17) to (5.19).

$$F_{t,\tau} = -r\frac{\rho_t g}{2}\cos\chi\cos\beta + \frac{\rho C_{D,c} d_t r}{8} v_a(v_{w,\chi} - v_\tau) \tag{5.17}$$

$$F_{t,n} = -r\frac{\rho_t g}{2}\sin\chi\cos\beta + \frac{\rho C_{D,c} d_t r}{8} v_a v_{w,n} \tag{5.18}$$

$$F_{tg,r} = -F_{t,r} - \rho_t g \sin\beta + \frac{\rho C_{D,c} d_t r}{8} v_a(v_{w,r} - v_r) \tag{5.19}$$

5.2. Aerodynamic force acting on the kite

The aerodynamic force on the kite is the sum of the kite lift **L** and kite drag **D**. Defining the lift and drag coefficients C_L and C_D per equation (5.20) and equation (5.21), allows the aerodynamic force $\mathbf{F}_\mathsf{a}$ to be defined by equation (5.22). Here, S is the kite surface, ρ the air density and $\mathbf{e}_\mathsf{D}, \mathbf{e}_\mathsf{L}$ are the unit vectors of the lift and drag forces.

$$C_L = \frac{\|\mathbf{L}\|}{\frac{1}{2}\rho\|\mathbf{v}_\mathsf{a}\|^2 S} \tag{5.20}$$

$$C_D = \frac{\|\mathbf{D}\|}{\frac{1}{2}\rho\|\mathbf{v}_\mathsf{a}\|^2 S} \tag{5.21}$$

$$\mathbf{F}_\mathsf{a} = \mathbf{D} + \mathbf{L} = \frac{1}{2}\rho\|\mathbf{v}_\mathsf{a}\|^2 S(C_D\mathbf{e}_\mathsf{D} + C_L\mathbf{e}_\mathsf{L}) \tag{5.22}$$

The task at hand is to obtain expressions for the unit vectors $\mathbf{e}_\mathsf{D}, \mathbf{e}_\mathsf{L}$ in terms of C-frame unit vectors $\mathbf{e}_\chi, \mathbf{e}_\mathsf{n}, \mathbf{e}_\mathsf{r}$.

For the drag unit vector $\mathbf{e}_\mathsf{D}$, this becomes quite trivial when we realize that drag is aligned with the apparent wind velocity $\mathbf{v}_\mathsf{a}$. Decomposing the apparent wind velocity into C-frame components (equation (5.23)), gives equation (5.24).

$$\begin{aligned}\mathbf{v}_\mathsf{a} &= \mathbf{v}_\mathsf{k} - \mathbf{v}_\mathsf{w} \\ &= v_{a,\chi}\mathbf{e}_\chi + v_{a,n}\mathbf{e}_\mathsf{n} + v_{a,r}\mathbf{e}_\mathsf{r}\end{aligned} \tag{5.23}$$

$$\begin{aligned}\mathbf{e}_\mathsf{D} &= \frac{1}{v_a}\mathbf{v}_\mathsf{a} \\ &= \frac{1}{v_a}\begin{bmatrix} v_{a,\chi} \\ v_{a,n} \\ v_{a,r}\end{bmatrix}^{\chi,n,r}\end{aligned} \tag{5.24}$$

Obtaining the expression for lift unit vector $\mathbf{e}_\mathsf{L}$ requires more work. Although we know that the lift vector **L** must lie in the plane normal to the apparent wind, we do not yet know the orientation of the unit vector **L** in this normal plane.

To obtain the direction of $\mathbf{e}_\mathsf{L}$ in this normal plane, let's start by defining the basis vectors that span this plane. Once these basis vectors are defined, $\mathbf{e}_\mathsf{L}$ can be decomposed in these basis vectors.

Consider the somewhat arbitrary reference frame C', with unit vectors $\mathbf{e}_{\chi'}, \mathbf{e}_{\mathsf{n}'}, \mathbf{e}_{\mathsf{r}'}$. If it is oriented such that $\mathbf{e}_{\chi'}$ points in the negative direction of the apparent wind vector $\mathbf{v}_\mathsf{a}$, then the ($\mathbf{e}_{\mathsf{n}'}, \mathbf{e}_{\mathsf{r}'}$)-plane must be normal to the wind vector (Figure 5.2).

Figure 5.2 shows that the transformation $\mathbb{T}_{C' \leftarrow C}$ required to obtain the C'-frame, consists of a rotation of magnitude $-\chi_a$ around the $\mathbf{e}_\mathsf{r}$-vector, followed by a rotation of magnitude γ_a around the $\mathbf{e}_{\mathsf{n}'}$-vector (equation (5.25)). We will respectively call these angles the aerodynamic heading and the aerodynamic flight path. Physically, χ_a is the direction of the incoming wind in the tangential plane τ, and γ_a is the angle between the incoming wind and the tangential plane. The rotation around $\mathbf{e}_\mathsf{r}$ is by -χ_a, such that wind coming 'from the right' has a positive value, which is in line with aeronautical conventions.

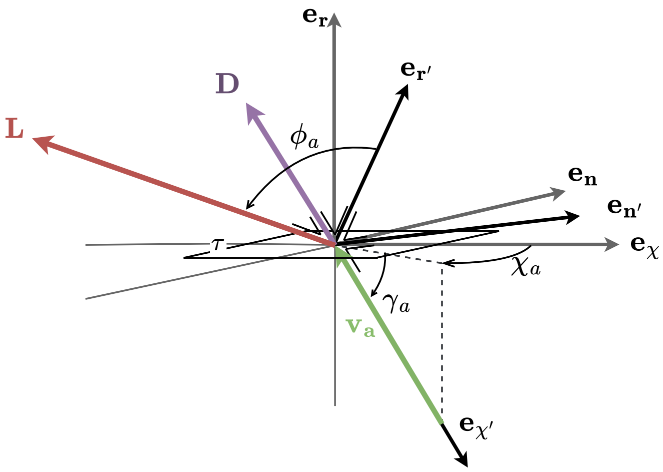

Figure 5.2: Required transformation $\mathbb{T}_{C' \leftarrow C}$ such that the ($\mathbf{e}_{n'}$, $\mathbf{e}_{r'}$)-plane is normal to the apparent wind velocity $\mathbf{v}_a$. Note that χ_a is defined positive in the negative direction of $\mathbf{e}_r$.

$$\begin{aligned}\mathbb{T}_{C' \leftarrow C} &= \mathbb{T}_{n'}(\gamma_a)\mathbb{T}_r(-\chi_a) \\ &= \begin{bmatrix} \cos\gamma_a \cos\chi_a & -\cos\gamma_a \sin\chi_a & \sin\gamma_a \\ \sin\chi_a & \cos\chi_a & 0 \\ -\sin\gamma_a \cos\chi_a & \sin\gamma_a \sin\chi_a & \cos\gamma_a \end{bmatrix}\end{aligned} \tag{5.25}$$

$$\begin{bmatrix} \mathbf{e}_{\chi'} \\ \mathbf{e}_{n'} \\ \mathbf{e}_{r'} \end{bmatrix} = \mathbb{T}_{C' \leftarrow C} \begin{bmatrix} \mathbf{e}_{\chi} \\ \mathbf{e}_{n} \\ \mathbf{e}_{r} \end{bmatrix} \tag{5.26}$$

Applying the doc product with $\mathbf{v}_a$ to both sides in equation (5.26), we obtain the system of equations in equation (5.27), i.e. the apparent wind speed components in the plane normal to $\mathbf{v}_a$ are both zero.

$$\begin{bmatrix} 0 \\ 0 \end{bmatrix} = \begin{bmatrix} \sin\chi_a & \cos\chi_a & 0 \\ -\sin\gamma_a \cos\chi_a & \sin\gamma_a \sin\chi_a & \cos\gamma_a \end{bmatrix} \begin{bmatrix} v_{a,n} \\ v_{a,r} \end{bmatrix} \tag{5.27}$$

Solving for the aerodynamic heading χ_a and aerodynamic flight path γ_a gives equations (5.29) and (5.30), respectively. Note that $\sqrt{v_{a,\chi}^2 + v_{a,n}^2}$ is simply the apparent wind velocity projected onto the tangential plane τ, which can be written as $v_{a,\tau}$, per equation (5.28).

$$v_{a,\tau} \equiv \sqrt{v_{a,\chi}^2 + v_{a,n}^2} \tag{5.28}$$

$$\tan\chi_a = -\frac{v_{a,n}}{v_{a,\chi}} \tag{5.29}$$

$$\tan\gamma_a = \frac{v_{a,r}}{\sqrt{v_{a,\chi}^2 + v_{a,n}^2}} = \frac{v_{a,r}}{v_{a,\tau}} \tag{5.30}$$

After substituting equations (5.29) and (5.30) into equation (5.26) and simplifying the trigonometric functions, we have obtained the two basis vectors that span the plane normal to $\mathbf{v}_a$, given in equations (5.31) and (5.32).

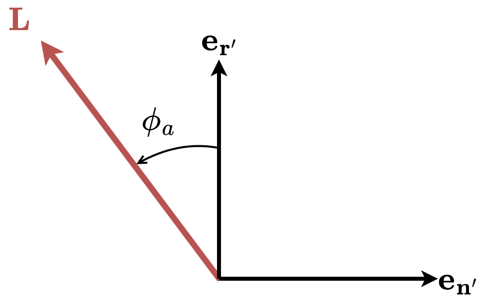

Figure 5.3: Direction of lift **L** in the $(\mathbf{e}_{\mathrm{n}'}, \mathbf{e}_{\mathrm{r}'})$-plane normal to the apparent wind $\mathbf{v}_{\mathrm{a}}$ roll ϕ_a, determined by the aerodynamic roll ϕ_a.

$$\mathbf{e}_{\mathrm{n}'} = \frac{1}{v_{a,\tau}} \begin{bmatrix} v_{a,n} \\ -v_{a,\chi} \\ 0 \end{bmatrix}^{\chi,n,r} \tag{5.31}$$

$$\mathbf{e}_{\mathrm{r}'} = \frac{1}{v_a v_{a,\tau}} \begin{bmatrix} -v_{a,\chi} v_{a,r} \\ -v_{a,n} v_{a,r} \\ v_{a,\tau}^2 \end{bmatrix}^{\chi,n,r} \tag{5.32}$$

The lift unit vector $\mathbf{e}_{\mathrm{L}}$ is then obtained by decomposition into these basis vectors. Introducing the aerodynamic roll ϕ_a as the angle between $\mathbf{e}_{\mathrm{r}'}$ and $\mathbf{e}_{\mathrm{L}}$ (figure 5.3), yields the decomposition in equations (5.33) and (5.34). By definition of ϕ_a, $\phi_a = 0$ corresponds to lift acting in the direction of $\mathbf{e}_{\mathrm{r}}$ and that $0 < \phi_a < \pi$ induces a right-hand turn from the perspective of the kite.

$$\mathbf{e}_{\mathrm{n}'} = -\sin\phi_a \mathbf{e}_{\mathrm{L}} \tag{5.33}$$

$$\mathbf{e}_{\mathrm{r}'} = \cos\phi_a \mathbf{e}_{\mathrm{L}} \tag{5.34}$$

Finally, $\mathbf{e}_{\mathrm{L}}$ is expressed in C-frame components by substituting equations (5.29), (5.30), (5.33) and (5.34) into equation (5.26), resulting in equation (5.35).

$$\begin{aligned} \mathbf{e}_{\mathrm{L}} &= -\sin\phi_a \mathbf{e}_{\mathrm{n}'} + \cos\phi_a \mathbf{e}_{\mathrm{L}} \\ &= \frac{1}{v_a v_{a,\tau}} \begin{bmatrix} -v_a v_{a,n} \sin\phi_a - v_{a,\chi} v_{a,r} \cos\phi_a \\ v_a v_{a,\chi} \sin\phi_a - v_{a,n} v_{a,r} \cos\phi_a \\ v_{a,\tau}^2 \cos\phi_a \end{bmatrix}^{\chi,n,r} \end{aligned} \tag{5.35}$$

The aerodynamic force $\mathbf{F}_{\mathrm{a}}$ is then expressed in C-frame unit-vectors as function of the aerodynamic roll angle ϕ_a and apparent wind speed components $v_{a,\chi}, v_{a,n}, v_{a,r}$ per equation (5.36), which is obtained through substitution of equations (5.24) and (5.35) into equation (5.22).

$$\mathbf{F}_{\mathrm{a}} = \frac{1}{2}\rho S C_D v_a \begin{bmatrix} v_{a,\chi} \\ v_{a,n} \\ v_{a,r} \end{bmatrix}^{\chi,n,r} + \frac{1}{2}\rho S C_L \frac{v_a}{v_{a,\tau}} \begin{bmatrix} -v_a v_{a,n} \sin\phi_a - v_{a,r} v_{a,\chi} \cos\phi_a \\ v_a v_{a,\chi} \sin\phi_a - v_{a,n} v_{a,r} \cos\phi_a \\ v_{a,\tau}^2 \cos\phi_a \end{bmatrix}^{\chi,n,r} \tag{5.36}$$

If the aerodynamics are assumed steady, then the values of the lift and drag coefficients C_L, C_D are constant.

6
Imposing the kite trajectory

So far, we have that the external loads on the kite depend on the tether tension at the ground station F_{tg}, the aerodynamic roll ϕ_a, the wind velocity $\mathbf{v}_\mathrm{w}$, and the kite velocity $\mathbf{v}_\mathrm{k}$. Similarly, we know that the acceleration of the kite depends on the external loads, the kite velocity, and the kite position.

Simulating kite motion thus becomes an initial value problem, i.e. what is the kite trajectory as a result of given ground station force, aerodynamic roll angle, and wind velocity inputs? However, to study the importance of the inertial forces, the 'inverse' of this problem must be solved, that is: what ground station force and aerodynamic roll angle are required to fly a given flight path?

In this chapter, the kite trajectory is parameterized and solution schemes are derived to obtain the force inputs required for flying the parameterized trajectory.

6.1. General parameterization problem description

Let $\mathbf{R}(s)$ be the parameterization of the position vector $\mathbf{r}_\mathrm{k}$ of point k, i.e. $\mathbf{r}_\mathrm{k} = \mathbf{R}(s)$. Then, the motion of point k is constrained by Equation 6.1.

$$\mathbf{r}_\mathrm{k}(t) = \mathbf{R}(s(t)) \tag{6.1}$$

This means that given a parametric path curve $\mathbf{R}(s)$, simulating the motion of k requires finding the time-dependent coordinate function $s(t)$. Differentiating Equation 6.1 with respect to t gives equation (6.2), and applying the dot product with $\frac{d\mathbf{R}}{ds}$ to both sides, results in equation (6.3).

$$\frac{d\mathbf{r}_\mathrm{k}}{dt} = \frac{d\mathbf{R}}{ds}\frac{ds}{dt} \tag{6.2}$$

$$\frac{d\mathbf{r}_\mathrm{k}}{dt} \cdot \frac{d\mathbf{R}}{ds} = \frac{ds}{dt}\left\|\frac{d\mathbf{R}}{ds}\right\|^2 \tag{6.3}$$

By definition of the dot product in equation (6.4), we obtain equation (6.5), realizing that the angle between $\frac{d\mathbf{r}_\mathrm{k}}{dt}$ and $\frac{d\mathbf{R}}{ds}$ is zero.

$$\mathbf{a} \cdot \mathbf{b} \equiv \|\mathbf{a}\|\,\|\mathbf{b}\| \cos\theta_{a,b} \tag{6.4}$$

$$\frac{d\mathbf{r}_\mathrm{k}}{dt} \cdot \frac{d\mathbf{R}}{ds} = \left\|\frac{d\mathbf{r}_\mathrm{k}}{dt}\right\| \left\|\frac{d\mathbf{R}}{ds}\right\| \tag{6.5}$$

Substituting equation (6.5) into equation (6.3) results in the normalized path speed $\dot{s}$ in equation (6.6), where the kite speed $v_k \equiv \left\|\frac{d\mathbf{r}_\mathrm{k}}{dt}\right\|$ is the magnitude of the velocity vector.

$$\dot{s} = \frac{v_k}{\left\|\frac{d\mathbf{R}}{ds}\right\|} \tag{6.6}$$

Finding the expression for $s(t)$ forms an initial value problem, considering that $s(t_0) = s_0$. Or in other words, simulating kite motion along a parameterized path, forms an differential problem where equation (6.6) must be satisfied, together with the force equations of motion.

6.2. Parameterization equations in the AZR-frame

To demonstrate the use of this formulation, let us consider the parameterization functions $\phi(s), \beta(s)$ and $r(s)$ for the AZR-frame coordinates (ϕ, β, r) in equation (6.7).

$$\phi = \phi(s) \qquad \beta = \beta(s) \qquad r = r(s) \tag{6.7}$$

We will use these parameterization functions to express the state variables of the dynamic equations of motion of section 4.3 in terms of the path parameters, that is, find expressions for all components of state vector **x** in equation (6.8) terms of $s, \dot{s}, \ddot{s}$.

$$\mathbf{x} = (\phi, \beta, r, v_\tau, v_r, \chi, \dot{v}_\tau, \dot{v}_r, \dot{\chi}) \tag{6.8}$$

To start, we realize that the parameterized position vector $\mathbf{R}(s)$ simply becomes equation (6.9).

$$\mathbf{R}(s) = r\mathbf{e}_\mathrm{r} \tag{6.9}$$

The derivation of $\frac{d\mathbf{R}}{ds}$ is similar to the derivation of the velocity vector in section 4.2. Note that $\frac{d\mathbf{R}}{ds}$ is given in terms of AZR-frame unit vectors.

$$\begin{aligned}
\frac{d\mathbf{R}}{ds} &= \frac{dr}{ds}\mathbf{e}_\mathrm{r} + r\frac{d\mathbf{e}_\mathrm{r}}{ds} \qquad (6.10)\\
&= \frac{dr}{ds}\mathbf{e}_\mathrm{r} + \mathbf{\Omega}_{AZR} \times \mathbf{R}\\
&= \frac{dr}{ds}\mathbf{e}_\mathrm{r} + \left(\frac{d\phi}{ds}\mathbf{e}_z - \frac{d\beta}{ds}\mathbf{e}_\phi\right) \times \mathbf{R}\\
&= \begin{bmatrix} 0 \\ 0 \\ \frac{dr}{ds} \end{bmatrix} + \begin{bmatrix} -\frac{d\beta}{ds} \\ \frac{d\phi}{ds}\cos\beta \\ \frac{d\phi}{ds}\sin\beta \end{bmatrix} \times \begin{bmatrix} 0 \\ 0 \\ r \end{bmatrix}\\
&= \begin{bmatrix} r\frac{d\phi}{ds}\cos\beta \\ r\frac{d\beta}{ds} \\ \frac{dr}{ds} \end{bmatrix}^{\phi,\beta,r} \qquad (6.11)
\end{aligned}$$

Such that the magnitude $\left\|\frac{d\mathbf{R}}{ds}\right\|$ becomes equation (6.12). One can see that this actually is the arc length integrand for a curve in spherical coordinates.

$$\left\|\frac{d\mathbf{R}}{ds}\right\| = \sqrt{\frac{dr}{ds}^2 + r^2\frac{d\beta}{ds}^2 + r^2\frac{d\phi}{ds}^2\cos^2\beta} \tag{6.12}$$

Realizing that the relative velocity of K in the rotating reference frame AZR is the same as the lefthand term on the right side of equation (6.10) scaled with $\dot{s}$, results in the radial speed component v_r in path parameters s and $\dot{s}$ in equation (6.13).

$$\left[\frac{d\mathbf{r}_\mathrm{k}}{dt}\right] = \frac{dr}{ds}\dot{s}\mathbf{e}_\mathrm{r} \quad \rightarrow v_r = \frac{dr}{ds}\dot{s} \tag{6.13}$$

By the definition of the kite velocity components v_τ and v_r in equation (4.5), we have that the kite speed v_k is given by equation (6.14). Substituting equations (6.6) and (6.13), gives the expression for v_τ in terms of path parameters $s, \dot{s}, \ddot{s}$ in equation (6.15).

$$
\begin{aligned}
v_k &= \sqrt{v_\tau^2 + v_r^2} \qquad (6.14)\\
v_\tau &= \sqrt{v_k^2 - v_r^2}\\
&= \sqrt{\dot{s}^2 \left\| \frac{d\mathbf{R}}{ds} \right\|^2 - \dot{s}^2 \frac{dr}{ds}^2}\\
&= \dot{s} r \sqrt{\frac{d\beta}{ds}^2 + \frac{d\phi}{ds}^2 \cos^2\beta} \qquad (6.15)
\end{aligned}
$$

The course angle rate $\dot{\chi}$ in equation (6.16) is obtained by applying the chain rule to the derivative $\frac{d\chi}{ds}$, which in turn follows from substituting the paremeterizations for ϕ and β in equation (4.20).

$$
\begin{aligned}
\dot{\chi} &= \frac{d\chi}{ds}\dot{s}\\
&= \dot{s}\left(\frac{\frac{d^2\phi}{ds^2}\frac{d\beta}{ds}\cos\beta - \frac{d\phi}{ds}\frac{d\beta}{ds}^2\sin\beta - \frac{d\phi}{ds}\frac{d^2\beta}{ds^2}\cos\beta}{\frac{d\beta}{ds}^2 + \frac{d\phi}{ds}^2\cos^2\beta} \right) \qquad (6.16)
\end{aligned}
$$

The acceleration components $\dot{v}_\tau, \dot{v}_r$ are found by time-differentiation of equations (6.13) and (6.15), respectively. Applying the product and chain rules gives $\dot{v}_r$ in equation (6.17), and though more tedious, $\dot{v}_\tau$ becomes equation (6.18).

$$
\begin{aligned}
\dot{v}_r &= \frac{d^2 r}{ds^2}\dot{s}^2 + \frac{dr}{ds}\ddot{s} \qquad (6.17)\\
\dot{v}_\tau &= \left(\dot{s}^2\frac{dr}{ds} + \ddot{s}r\right)\sqrt{A} + \frac{\dot{s}r}{2\sqrt{A}}\dot{A} \qquad (6.18)
\end{aligned}
$$

In equation (6.18), we have introduced A as in equation (6.19), such that its time derivative $\dot{A}$ becomes equation (6.20).

$$
\begin{aligned}
\sqrt{A} &\equiv \frac{v_\tau}{\dot{s}r} \qquad (6.19)\\
&= \sqrt{\frac{d\beta}{ds}^2 + \frac{d\phi}{ds}^2\cos^2\beta}\\
\dot{A} &= 2\dot{s}\left(\frac{d\beta}{ds}\frac{d^2\beta}{ds^2} + \frac{d\phi}{ds}\frac{d^2\phi}{ds^2}\cos^2\beta - \frac{d\phi}{ds}^2\frac{d\beta}{ds}\cos\beta\sin\beta\right) \qquad (6.20)
\end{aligned}
$$

Substitution of the parameterization equations (6.13) and (6.15) to (6.20) into the equations of motion from chapter 4 essentially reduces the number of degrees of freedom in the system. In general flight, three DOFs are present: motion in the course and radial directions and the course angle. For parameterized flight, only one DOF is present: motion along the path, quantified by the path coordinate s.

Finally, by substituting the kite aerodynamic force and tether force equations of chapter 5 into the resulting 1-DOF differential equation of parameterized motion, the forces resulting from a parameterized path can be solved for.

6.3. Setting up path parameterizations

This section discusses various methods to parameterize the flight path. Parameterization can be done explicitly in terms of the path coordinate s, that is, the path is fixed in space. However, if the kite speed varies along such fixed path, the reeling speed of the kite will vary too.

More realistic would be to operate the AWE system with a constant reeling speed, and therefore the path must not be fixed in time. The corresponding method of parameterizing such flexible flight path is to express the path in both s and time t, as will be dicussed in this section.

6.3.1. Parameterizing in s

Parameterizing the path in terms of the path coordinate s can be done in various ways. Common crosswind maneuvers are a circular maneuver, or a figure-eight-like maneuver. Such maneuver is typically elevated at a certain path elevation angle β_P. The following subsections present examples of how to parameterize the flight path resulting from such crosswind maneuvers.

Example: downwind helix

A helical flight path can be described in W-frame coordinates by equation (6.21). Here, the helix radius r_h is the distance to the downwind vector $\mathbf{e}_x$, and ω is the maneuver frequency.

$$x = x_0 + s \qquad y = r_h \sin(\omega s) \qquad z = r_h \cos(\omega s) \tag{6.21}$$

Applying the transformation $\mathbb{T}_{AZR \leftarrow W}$ in equation (4.4), results in the AZR-coordinate parameterization functions in equation (6.22).

$$\phi = \arctan \frac{y}{x} \qquad \beta = \arctan \frac{z}{\sqrt{x^2 + y^2}} \qquad r = \sqrt{x^2 + y^2 + z^2} \tag{6.22}$$

Substituting the helix-parameterization equation (6.21) into equation (6.22) results in the spherical coordinates in equations (6.23) to (6.25). Analytical expressions for the first and second order s-derivatives of the parameterizations can be found through existing algebraic solvers, such as the `sympy` python library.

$$\phi = \arctan \frac{r_h \sin(\omega s)}{x_0 + s} \tag{6.23}$$

$$\beta = \arctan \frac{r_h \cos(\omega s)}{\sqrt{x_0^2 + s^2 + 2x_0 s + r_h^2 \sin^2(\omega s)}} \tag{6.24}$$

$$r = \sqrt{x_0^2 + s^2 + 2x_0 s + r_h^2} \tag{6.25}$$

Example: elevated helix

A realistic helical flight path in AWE systems is not aligned with the downwind vector, but oriented at a certain path elevation angle β_p. Let's denote the unit vectors that span this elevated reference frame x', y' and z'. The elevated helix then becomes:

$$\mathbf{R}(s) = x'\mathbf{e}_{x'} + y'\mathbf{e}_{y'} + z'\mathbf{e}_{z'} \tag{6.26}$$

$$= \begin{bmatrix} x_0 + s \\ r_h \sin(\omega s) \\ r_h \cos(\omega s) \end{bmatrix}^{x',y',z'} \tag{6.27}$$

To obtain the W-frame unit vectors from the elevated unit vectors, we simply have the rotation matrix $\mathbb{T}_y(\beta_p)$ in equation (6.28).

$$\mathbb{T}_y(\beta_p) = \begin{bmatrix} \cos\beta_p & 0 & -\sin\beta_p \\ 0 & 1 & 0 \\ \sin\beta_p & 0 & \cos\beta_p \end{bmatrix} \tag{6.28}$$

The W-frame unit vector components (x, y, z) straightforwardly become equations (6.29) to (6.31), resulting in the elevated helix parameterization in equation (6.32).

$$x = x' \cos\beta_p - z' \sin\beta_p \tag{6.29}$$

$$y = y' \tag{6.30}$$

$$z = x' \sin\beta_p + z' \cos\beta_p \tag{6.31}$$

$$\mathbf{R}(s) = \mathbb{T}_y(\beta_p)\begin{bmatrix} x_0 + s \\ r_h \sin(\omega s) \\ r_h \cos(\omega s) \end{bmatrix} = \begin{bmatrix} \cos\beta_p(x_0+s) - \sin\beta_p r_h \cos(\omega s) \\ r_h \sin(\omega s) \\ \sin\beta_p(x_0+s) + \cos\beta_p r_h \cos(\omega s) \end{bmatrix}^{x,y,z} \tag{6.32}$$

An example of such elevated helix is given in figure 6.1, where $\beta_p = 35°$ and $r_h = 40$ m. The brown dot represents the ground station position $O(0,0,0)$. In the (x,z)-plane projection in figure 6.1b, the helix elevation and constant helix pitch are clearly visible.

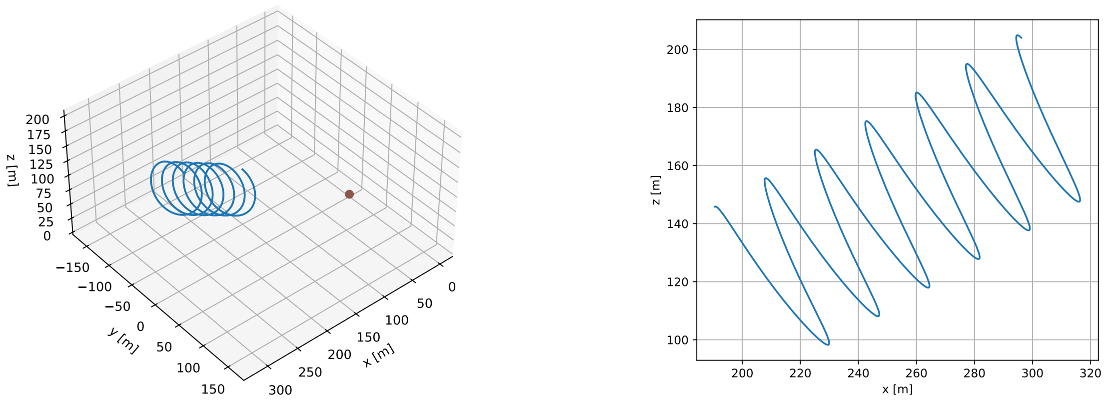

(a) Isometric view

(b) Projection on the (x,z)-plane

Figure 6.1: An elevated helix, parameterized by equation (6.32), with $\beta_p = 35°$ and $r_h = 40$ m. The brown dot represents the ground station point $O(0,0,0)$.

Example: elevated Lissajous figure-eight

The parameterization transformation equation (6.28) can also be used to effortlessly parameterize a more realistic elevated figure-eight flight path. Consider the Lissajous figure-eight parameterization in equation (6.33).

$$x' = x_0 + s \qquad y' = r_y \cos(\omega s) \qquad z' = r_z \sin(2\omega s) \tag{6.33}$$

The path represented by this parameterization is plotted in figure 6.2. Although this flight path may look realistic, it is not. The almost straight, crosswind segments of the figure eight dictate that the kite must be reeled-in during the traction phase. Such impractical reeling-strategy stresses the limitations of parameterizing the path with only the path coordinate s.

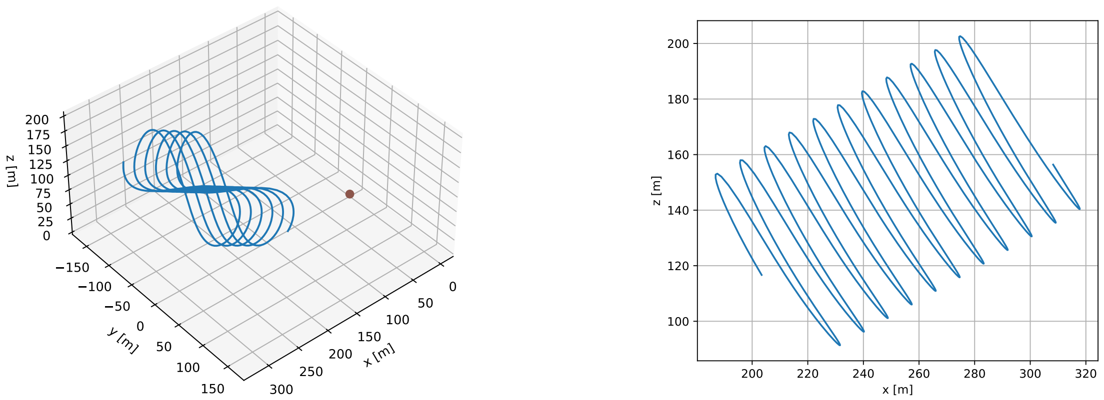

(a) Isometric view

(b) Projection on the (x,z)-plane

Figure 6.2: An elevated Lissajous figure-eight, parameterized by equation (6.33), with $\beta_p = 35°, r_y = 100$m and $r_z = 50$m.

6.3.2. Parameterizing in both s and t

Parameterization with constant reelout speed

In realistic operation of AWE systems, the radial kite speed is not controlled in periodic fashion resulting from the s-parameterization previously discussed. A more realistic control scheme is to keep the reeling speed constant throughout a phase (equation (6.34)).

$$r = r_0 + v_r t \tag{6.34}$$

The parameterization equations must be adapted to comply with such constant reelout speed. Suppose that the flight pattern should stay the same (e.g. circles with constant radius on the $y'z'$-plane), then only the function for x or x' should be adjusted (equation (6.35)).

$$x' = \sqrt{r^2 - (y')^2 - (z')^2} \tag{6.35}$$

For the downwind helix case, the constant reelout speed constraint in equation (6.34) results in the parameterization in equation (6.36). The parameterizations for the elevated helix or elevated figure-eight can be adapted to fit with a constant reelout scheme in a similar fashion.

$$x = \sqrt{\left(r_0 + v_r t\right)^2 - r_h^2} \qquad y = r_h \sin \omega s \qquad z = r_h \cos \omega s \tag{6.36}$$

Impact of parameterizing in t: (counterinuitive) history-dependency of the course angle

Imposing the time-dependent function $r(t)$ means that now, the ϕ and β parameterization functions depend on both s and t. Thus, for a path parameterized in s and t, the total derivatives in the parameterization equations in section 6.2, should include partial derivatives. The first order total azimuth derivative with respect to s it obtained as follows.

$$\begin{aligned} \frac{d\phi}{ds} &= \frac{\partial \phi}{\partial s} + \frac{\partial \phi}{\partial t}\frac{dt}{ds} \\ &= \frac{\partial \phi}{\partial s} + \frac{1}{\dot{s}}\frac{\partial \phi}{\partial t} \end{aligned} \tag{6.37}$$

And similarly, the s-derivatives of the elevation angle and radial distance become:

$$\frac{d\beta}{ds} = \frac{\partial \beta}{\partial s} + \frac{1}{\dot{s}}\frac{\partial \beta}{\partial t} \tag{6.38}$$

$$\frac{dr}{ds} = \frac{v_r}{\dot{s}} \tag{6.39}$$

This implies that the course angle χ depends on s, t and $\dot{s}$, where in the previously discussed cases it only depended on s.

The dependency on t is explained by the reeling out motion. Consider for example the helix with constant radius r_h and constant reelout speed $v_r > 0$. If s is constant, i.e. $v_\tau = 0$, but t is increasing, i.e, r is increasing, then the azimuth and elevation angles must decrease. This affects the course angle, eplaining the dependency of χ on t.

However, the dependency of χ on $\dot{s}$ seems most counterintuitive: how can the course angle at any position be affected by the kite speed at that position? The answer lies in the history-dependency caused by the radial position being parameterized t.

Namely, if the radial position is dictated by t, the arc length integrand changes with $\dot{s}$ (this is proven by substitution of equations (6.37) to (6.39) into equation (6.11)). Or in other words: the path shape is affected by the kite's speed. Depending on how fast the kite has traveled along the flight path, the path will have had a different arc length and therefore, the course angle can have multiple values for the same t and s.

$$\frac{\tan \chi}{\cos \beta} = \frac{d\phi}{d\beta} = \frac{\dot{s}\frac{\partial \phi}{\partial s} + \frac{\partial \phi}{\partial t}}{\dot{s}\frac{\partial \beta}{\partial s} + \frac{\partial \beta}{\partial t}} \tag{6.40}$$

This history-dependency is governed by equation (6.40), and illustrated in figure 6.3. Here, two paths parameterized by the same elevated helix with constant reelout speed are plotted. The blue and orange traces have the same start and end values for t and s, but a different speed-history, shown by the $(t, \dot{s})$-plot in figure 6.3b. This difference in $\dot{s}$ explains the different values for χ possible for the same t and s. For this specific example, the course angle start and end values are $\chi_0 = 122.6°, \chi_1 = 292.9°$ for the blue trace, and $\chi_0 = 93.28°, \chi_1 = 306.4°$ for the orange trace.

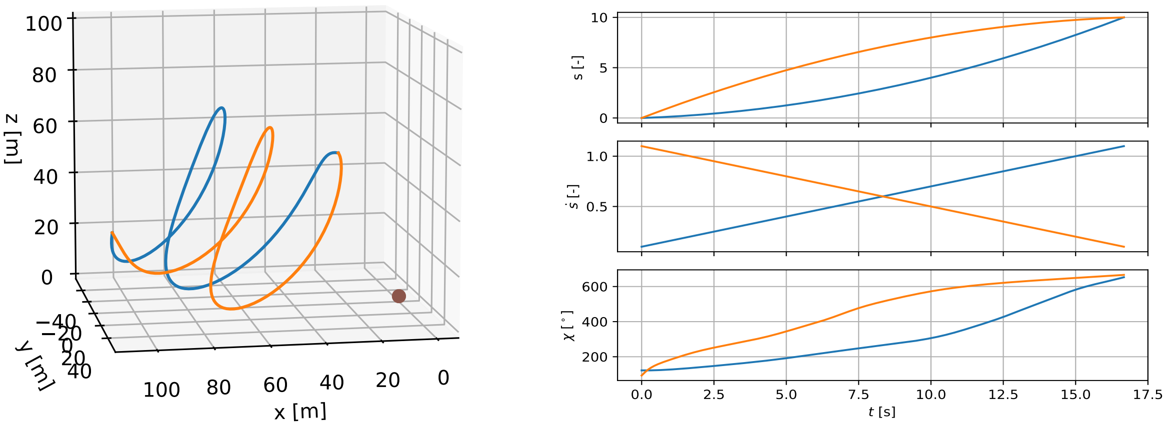

(a) Isometric view

(b) State variables s, $\dot{s}$ and χ versus time t.

Figure 6.3: The course angle χ is history-dependent, if the path is parameterized in both s and t. In such case, the path shape is affected by $\dot{s}$, meaning that χ can attain multiple values at the same time t. Even at the same time t and position s, there is no unique value of χ. These paths are parameterized by the same equations, specifying a circular motion in the $y'z'$-plane with constant reelout speed.

Observe that similar history-dependency is present for the course angle rate of change $\dot{\chi}$, shown in equation (6.41). Prescribing a function for r explicit in t does not raise the order of the differential problem, equation (6.41) is still only contains first order derivatives, but the nonlinearity of the problem has greatly increased because of the history-dependency.

$$\begin{aligned} \dot{\chi} &= \frac{d\chi}{ds}\dot{s} \\ &= \frac{\partial \chi}{\partial s}\dot{s} + \frac{\partial \chi}{\partial t} \end{aligned} \tag{6.41}$$

6.4. Parameterized position integration schemes

6.4.1. Dynamic position integration

Parameterizing the flight path considerably simplifies the simulation of dynamic kite motion. For a 'free flight' simulation, where the primary variables are ϕ, β, r, the first and second order derivatives are rather cumbersome to obtain, given the speed components v_τ, v_r, χ and acceleration components $\dot{v}_\tau, \dot{v}_r, \dot{\chi}$. In contrast, for the parameterized case, the primary variable is only s, and the first and second order derivatives are $\dot{s}$ and $\ddot{s}$, respectively. Given an the initial parameterized kite position and speed given by s, $\dot{s}$, the motion simulation becomes a relatively straightforward second order initial value problem.

Existing solvers can be used to solve this initial value problem, and typically require that the problem is given in state-space representation (i.e. as a system of first order differential equations). Algorithm 1 shows the pseudo-code of a solution algorithm to simulate the dynamic response using the publicly available Python-based `scipy.integrate.solve_ivp` procedure. The procedure `FindSddot` in algorithm 1 solves a dynamic state, given $t, s, \dot{s}$, and returns the solution in a state-space vector $(\dot{s}, \ddot{s})$. Once the solver has converged, the kite speed and loads are obtained by solving the dynamic state for each $t, s, \dot{s}, \ddot{s}$.

Depending on the force and path models, the problem can become quite stiff, requiring the use of an implicit solver. For a simple circular path with constant tether length, the explicit Runge-Kutta-

45 scheme quickly converges, but for a flight path with complex turns (such as a figure-eight with constant reelout speed), better model performance is obtained with scipy's implicit BFD solver, which uses various backward differentiation formulas.

Algorithm 1 Dynamic motion simulation for explicitly parameterized paths

procedure FindSddot($t, s, \dot{s}$) ▷ Expands 2nd order EOM as system of 1st order diff. eqs.
    procedure ForceResidual($\ddot{s}, \phi_a, F_{t,g}$)
        $(\phi, \beta, r) \leftarrow \mathbf{R}(t, s)$ ▷ Obtain position, speed and acceleration
        $v_\tau \leftarrow \dot{s} r \sqrt{A}$
        $v_r \leftarrow \frac{dr}{ds} \cdot \dot{s}$
        $\chi \leftarrow \chi(s, t, \dot{s})$
        $\dot{\chi} \leftarrow \frac{d\chi}{ds} \cdot \dot{s}$
        $\dot{v}_\tau \leftarrow \left(\dot{s}^2 \frac{dr}{ds} + \ddot{s} r\right) \sqrt{A} + \frac{\dot{s} r}{2\sqrt{A}} \dot{A}$
        $\dot{v}_r \leftarrow \frac{d^2 r}{ds^2} \dot{s}^2 + \frac{dr}{ds} \ddot{s}$
        $\mathbf{F_g} \leftarrow F_g(\phi, \beta, \chi, m, g)$
        $\mathbf{F_a} \leftarrow F_a(\phi, \beta, r, v_\tau, v_r, \chi, S, C_L, C_D, \rho)$
        $\mathbf{F_t} \leftarrow F_t(\phi, \beta, r, v_\tau, v_r, \chi, \rho_t, g, d_t, C_{D,t}, F_{t,g})$
        $\mathbf{F_i} \leftarrow F_i(\phi, \beta, r, v_\tau, v_r, \chi, \dot{v}_\tau, \dot{v}_r, \dot{\chi})$
        return $\mathbf{F_g} + \mathbf{F_a} + \mathbf{F_t} + \mathbf{F_i}$
    end procedure

    $(\ddot{s}, \phi_a, F_{t,g}) \leftarrow$ solve$\{$ForceResidual$(\ddot{s}, \phi_a, F_{t,g}) = 0\}$
    return $(\dot{s}, \ddot{s})$
end procedure

procedure DynamicMotion($t_0, s_0, \dot{s}_0, t_1, \Delta t$) ▷ Solves system of 1st order diff. eqs.
    return solve_ivp(FindSddot, $t_0, s_0, \dot{s_0}, t_1$, BDF))
end procedure

6.4.2. Quasi-steady position integration

For the special case where $\dot{s}$ is constant with respect to time, that is $\ddot{s} = 0$, the initial value problem in equation (6.6) is straightforwardly solved by equation (6.42), and the path coordinate s at $t + \Delta t$ becomes equation (6.43).

$$s(t) = s_0 + \frac{v_k}{\left\| \frac{d\mathbf{R}}{ds} \right\|} t \tag{6.42}$$

$$s(t + \Delta t) = s(t) + \Delta t \frac{v_k}{\left\| \frac{d\mathbf{R}}{ds} \right\|} \tag{6.43}$$

Substituting equation (6.43) into equation (6.1), results in the forward Euler scheme to integrate the position of k in equation (6.44).

$$\mathbf{r}_\mathsf{k}^{n+1} = \mathbf{R}(s^{n+1}) = \mathbf{R}\left(s^n + \Delta t \left(\frac{v_k}{\left\| \frac{d\mathbf{R}}{ds} \right\|}\right)^n\right) \tag{6.44}$$

Equation (6.44) is a quick and effective method to integrate the position along the parameterized path. Assuming $\ddot{s} = 0$ is very useful when simulating kite motion in a quasi-steady fashion, as the assumption reduces the order of the initial value problem: no information on $\ddot{s}$ and thus $\dot{v}_\tau$ and $\dot{v}_r$ is necessary.

Combining equation (6.44) with the quasi-steady EOM in section 4.3.4 forms a system of time-invariant equations, which can be straightforwardly solved by the time-marching scheme in algorithm 2.

Algorithm 2 shows how the quasi-steady EOM are solved iteratively. This iterative nature originates from v_τ depending on $\dot{\chi}$, while at the same time, $\dot{\chi}$ depends on $\dot{s}$ and thus on v_τ. Noom demonstrated a similar method [14], but skipped this iterative step to resolve the dependency of $\dot{\chi}$ on v_τ. Furthermore, they calculated $\dot{s}$ via equation (2.4), which, comparing to equation (6.15), seems to be missing the $\cos^2$ term. It would be interesting to assess the differences between assuming quasi-steadiness and assuming $\ddot{s} = 0$.

Algorithm 2 Quasi-steady motion simulation for explicitly parameterized paths

procedure QuasiSteadyMotion($t_0, s_0, t_1, \Delta t$)
  $t, s \leftarrow t_0, s_0$ ▷ Seed the iteration with initial conditions
  while $t \leq t_1$ **do** ▷ Forward Euler time-marching
    $(\phi, \beta, r) \leftarrow \mathbf{R}(t, s)$ ▷ Obtain position
    $(\dot{s}, v_k) \leftarrow (0, 1)$ ▷ Initial guess
    while $\dot{s} \left\| \frac{d\mathbf{R}}{ds} \right\| \neq v_k$ **do** ▷ Iteratively solve EOM until solution converges
      $\dot{s} \leftarrow v_k \left\| \frac{d\mathbf{R}}{ds} \right\|^{-1}$
      $\chi \leftarrow \chi(s, t, \dot{s})$
      $v_r \leftarrow \frac{dr}{ds} \cdot \dot{s}$
      $\dot{\chi} \leftarrow \frac{d\chi}{ds} \cdot \dot{s}$
      $(\dot{v}_\tau, \dot{v}_r) \leftarrow (0, 0)$ ▷ Impose quasi-steady condition
      $(v_\tau, \phi_a, F_{t,g}) \leftarrow$ solve$\{\Sigma\mathbf{F}(v_\tau, \phi_a, F_{t,g}) = 0\}$
      $v_k \leftarrow \sqrt{v_\tau^2 + v_r^2}$ ▷ Update kite speed with new solution
    end while
    $s \leftarrow s + \dot{s}\Delta t$ ▷ Update position and time
    $t \leftarrow t + \Delta t$
  end while
end procedure

Impact of the truncation error caused by assuming $\ddot{s} = 0$

Consider the parameterization equation (6.6). We realize that the condition $\ddot{s} = 0$ results in equation (6.45), i.e. the change in kite speed is governed by the change in the arc length integrand. Thus, the quasi-steady condition $\dot{v}_\tau = \dot{v}_r = 0$ only results in $\ddot{s} = 0$ for flight paths where the radial speed and arc length integrand are constant, e.g. a circular flight path with constant tether length. For all other flight paths, the quasi-steady condition can never result in $\ddot{s}$ to be zero.

$$\ddot{s} = \frac{d}{dt}\left(\frac{v_k}{\left\|\frac{d\mathbf{R}}{ds}\right\|}\right) = \frac{\left\|\frac{d\mathbf{R}}{ds}\right\| \dot{v}_k - v_k \frac{d}{dt}\left\|\frac{d\mathbf{R}}{ds}\right\|}{\left\|\frac{d\mathbf{R}}{ds}\right\|^2} = 0 \qquad \Rightarrow \dot{v}_k|_{\ddot{s}=0} = \dot{s}\frac{d}{dt}\left\|\frac{d\mathbf{R}}{ds}\right\| \tag{6.45}$$

This is further demonstrated by figure 6.4, which shows the simulation results for a kite flying a figure-eight path with a constant tether length, subjected to varying assumptions. Figure 6.4b shows the kite speed v_k, its time-derivative $\dot{v}_k$ and the tether tension at the ground $F_{t,g}$ for a dynamic simulation in blue. At each position, the quasi-steady solution is plotted in orange, and an solution assuming $\ddot{s} = 0$ is plotted in green. The solution for $\ddot{s} = 0$ results in significantly larger and time-shifted extrema of all the quantities plotted in figure 6.4b.

Concluding, a substantial truncation error may be introduced by the forward Euler scheme in equation (6.43), which depends locally on the change of the flight path curvature.

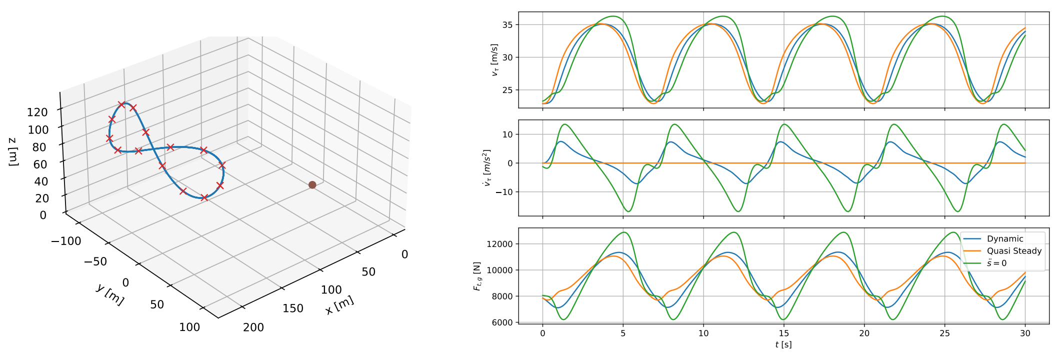

(a) Elevated figure-eight with constant tether length. A marker is plotted in constant intervals Δs.

(b) Tangential velocity (top) and tether force (bottom) versus time, for various force equilibrium conditions

Figure 6.4: A quasi-steady equilibrium and a ($\ddot{s} = 0$)-equilibrium differ substantially. The condition $\ddot{s} = 0$ is satisfied when the kite accelerates proportionally to the change in the path's arc length integrand, i.e. equation (6.45). In the case of a figure eight, the arc length integrand changes along the path, meaning that the quasi-steady condition can never result in $\ddot{s} = 0$, meaning that substantial truncation error may be induced.

7

Verifying the dynamic model

7.1. Qualitative discussion on the equations of motion

The dynamic equations of motion in equations (4.28) to (4.30) can be verified qualitatively by assessing the origin of each term in the equations.

$$\dot{v}_\tau = \frac{F_\tau}{m} - \frac{v_\tau v_r}{r} \tag{4.28}$$

Starting with equation (4.28), we see that the change in tangential speed $\dot{v}_\tau$ is simply the force-mass ratio in tangential direction, minus a Coriolis term. According to equation (4.28), if there no forces are present in the tangential direction and the kite is being reeled out, i.e. $F_\tau = 0$ and $v_r > 0$, we have that $\dot{v}_\tau < 0$, meaning that the kite's tangential speed will decrease. This is in line with expectations, since the angular momentum of the kite around the ground station must be conserved.

$$v_\tau \dot{\chi} = \frac{v_\tau^2}{r} \sin\chi \tan\beta - \frac{F_n}{m} \tag{4.29}$$

The normal force equilibrium equation (4.29) contains a term with represents the centrifugal force in the normal direction. equation (4.29) shows that to ensure a constant course angle (i.e. $\dot{\chi} = 0$), a nonzero normal force F_n is required, except when $\sin\chi \tan\beta = 0$, that is, except for when $\chi = 0 \mod \pi$ or $\beta = 0 \mod \pi$.

This condition may seem counterintuitive – shouldn't a constant χ result in an orthodromal flight path (i.e. a great circle with its center at the ground station), meaning that the normal forces F_n must be zero if $\dot{\chi} = 0$? However, a path set out by a constant χ does not necessarily form an orthodrome. Instead, it forms a loxodrome (or rhumb line), shown in figure 7.1. Such loxodrome is inherently curved, except for the specific values of χ and β mentioned earlier: then it coincides with the orthodrome. This curvature explains the centrifugal term in equation (4.29).

$$\dot{v}_r = \frac{F_r}{m} + \frac{v_\tau^2}{r} \tag{4.30}$$

Finally, the radial force equilibrium equation (4.30) states that the change in radial speed is affected by the radial forces and a centrifugal term $\frac{v_\tau^2}{r}$. The latter follows from the kite being tethered to the ground station: a kite flying with a constant radial speed, i.e. $\dot{v}_r = 0$ and positive tangential speed $v_\tau > 0$ must endure a negative radial (tether) force.

7.2. Comparison to Talmar's asymptotic solutions

Talmar's asymptotic tether force equation (2.9) describes the tether force for a kite flying a downwind helix, connected to a mass- and dragless tether in an environment with no gravity. In such situation, the presented dynamic model should converge to Talmar's solution.

Figure 7.2 shows how the dynamic response of a kite with zero initial kite speed quickly converges to Talmar's solution. Since for this comparison, only the ratio between the model's predicted tether force

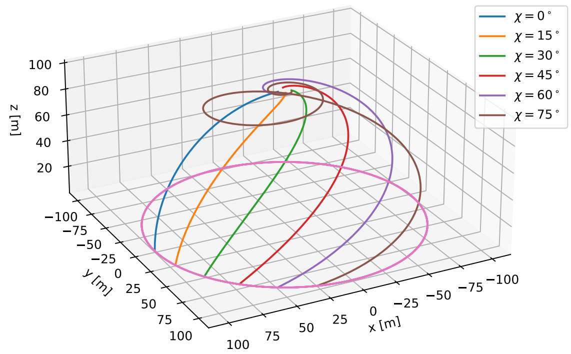

Figure 7.1: Loxodromes of constant course angle χ. Their inherent curvature explains the centrifugal term in the normal force equilibrium equation (4.29).

F_t and Talmar's tether force $F_{t,Talmar}$ are of interest, the exact kite properties (mass, surface area, etc) are irrelevant. Nonetheless, to demonstrate the good correspondence between the two models, a 'heavy' kite was simulated, with a surface-to-mass ratio of $0.1\,\mathrm{m^2\,kg^{-1}}$ such that the inertial forces are relatively high.

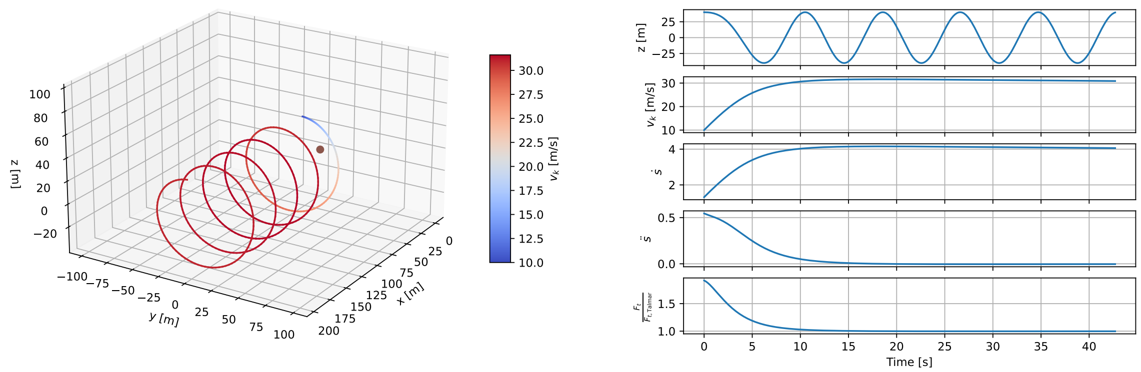

(a) Downwind helix. The color denotes the local kite speed v_k.

(b) State variables versus time.

Figure 7.2: Dynamic response of a kite with $\frac{S}{m} = 0.1$ and initial speed $v_\tau = 0$, flying a downwind helix in an environment with no gravity and uniform wind speed.

Figure 7.2 shows that the model corresponds well with Talmar's tether force. Within one revolution, the asymptotic state is reached and a near-steady tether force obtained. A small error in the order of $\mathcal{O}(10^{-4})$ remains present. This is explained by Talmar's model not taking into account the Coriolis acceleration caused by the positive reelout speed, meaning that Talmar slightly underestimates the tether force.

For a circular flight path with no reelout, the error in tether force converges to $\mathcal{O}(10^{-10})$, suggesting good correspondence of the dynamic model with the analytical solution.

7.3. Verification of the distributed tether drag model

The distributed drag tether model resolves the exponential distribution of the drag along the tether. Close to the ground station, the tether is virtually stationary, while close to the kite, the tether moves with the same velocity as the kite. This variation in speed affects the apparent wind, and therefore, the local drag components in the course, normal, and radial directions vary exponentially with the position l along the tether.

Figure 7.3 shows the distributed tether drag components along the tether, for a flight state at position

$\phi = 30°, \beta = 45°$, with course angle $\chi = 0°$, kite velocity components $v_\tau = 10\,\mathrm{m\,s^{-1}}, v_r = 3\,\mathrm{m\,s^{-1}}$, and wind speed $v_w = 10\,\mathrm{m\,s^{-1}}$. The expected nonlinear dependency is clearly visible: each component grows in magnitude with increasing $\frac{l}{r}$.

Note also how the drag component in the course direction is the strongest and experiences the largest variation. This is in line with expectations: close to the kite, the tangential speed of the tether is highest, resulting in the highest apparent wind speed in the course direction. This effect diminishes towards the ground station, leaving only true wind speed components and thus lower drag. Because of the reel-out motion, the drag in the radial direction is the smallest.

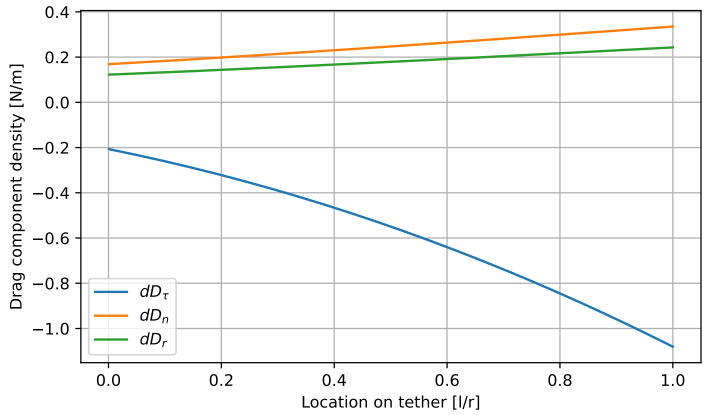

Figure 7.3: Drag distribution C-frame components dD_τ, dD_n, dD_r along the tether, for $\phi = 30°, \beta = 45°, \chi = 0°$, and velocity components $v_\tau = v_w = 10\,\mathrm{m\,s^{-1}}, v_r = 3\,\mathrm{m\,s^{-1}}$. Each component scales exponentially with relative position $\frac{l}{r}$, as expected.

7.3.1. Comparison with the simplified drag tether model

The distributed-drag-tether model can be further verified by comparing the tether force components with those resulting from the simplified-drag-tether model for an arbitrary state. Figure 7.4 shows the relative differences in the tether drag forces at the kite in the course, normal, and radial directions. This analysis is obtained with the same quantities as before, but including $r = 100\,\mathrm{m}$. A ground tether tension of $F_{t,g} = 1000\,\mathrm{N}$ is used to prevent compression at the kite, which can occur when the tension induced by the drag exceeds the compression induced by the tether gravity. Figure 7.4 shows that the differences between the two tether models are quite substantial.

The distributed drag model generally predicts much higher forces (up to 70%) in both the normal and course directions, with the discrepancies being the largest for high azimuth angle ϕ and high elevation angle β. Although the absolute differences relative to the tether tension are small (<3%), the significant discrepancy indicates that further validation of both tether models may be necessary to determine which model is most accurate.

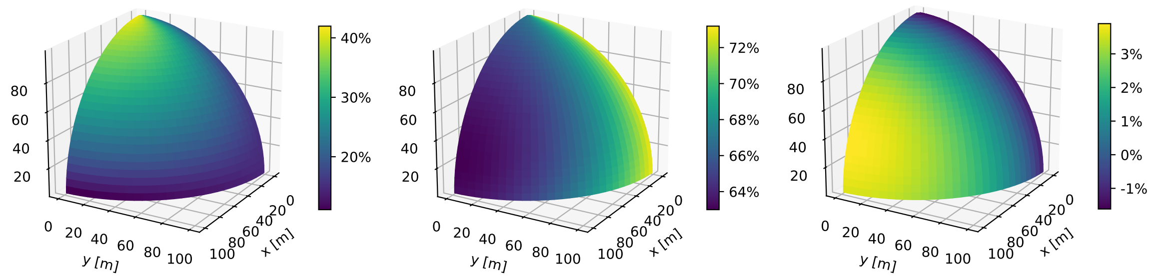

(a) Error in $F_{t,\tau}$ **(b)** Error in $F_{t,n}$ **(c)** Error in $F_{t,r}$

Figure 7.4: Distribution of the discrepancy between the distributed drag and simplified drag tether models. The error in tether force components F_τ, F_n, F_r is plotted over the downwind window, for $\chi = 0$. Tether gravity is included. The ground tension is $F_{t,g} = 1000\,\mathrm{N}$.

8

Analyzing the impact of the inertial forces

This chapter shows how simulations performed with the dynamic model compare to those performed with an inertia-free model and a quasi-steady model. The impact of resolving the kite inertia is first discussed qualitatively. In section 8.1, the effects of each inertial term are assessed, and the dominating inertial terms are identified. Other relevant phenomena caused by the dynamic simulation are discussed in section 8.2.

To see how the phenomena observed in the dynamic simulation scale for varying inputs, the solution space of the dynamic solution and the differences between the three models is analyzed in section 8.3. Finally, the impact of unsteady wind conditions and the impact of the tether model used are discussed in section 8.4.

8.1. Qualitatively assessing the effect of the distinct inertial terms

The inclusion of inertia in the dynamic model should result in a different solution, compared to the quasi-steady and inertia-free models. To better understand the contribution of each inertial term – namely the relative, Coriolis, centrifugal, and Euler accelerations – this section presents several variations of the equilibrium equations and their impact on the system response.

8.1.1. Identifying the dominating the inertial components

Six variations are used to simulate the response of a kite with mass-to-surface ratio $\frac{m}{S} = 8\,\mathrm{kg\,m^{-2}}$, flying a downwind helix with helix radius $r_h = 50\,\mathrm{m}$ and constant reelout speed of $3\,\mathrm{m\,s^{-1}}$. Because of the high kite mass, a lift-to-drag ratio of 6 was used to obtain convergence for all six variations. The tether drag and mass are neglected, gravity included, and a uniform wind speed of $v_w = 12\,\mathrm{m\,s^{-1}}$ is used. The six variations of the equations of motion are the inertia-free formulation, a formulation with only Coriolis forces considered, one with only centrifugal forces, one with both centrifugal and Coriolis, the quasi-steady formulation, and finally, the dynamic formulation.

The paths resulting from each formulation are plotted in figure 8.1a and the responses of the altitude, tangential speed and tether tension versus time are plotted in figure 8.1b. The dynamic position integration method was used only for the dynamic formulation, the quasi-steady integration method was used for all five other formulations.

Figure 8.1 shows how each variation of the equations of motion, results in different time-responses. Each response varies in amplitude, mean value and frequency. Note how the amplitudes in the v_τ and F_t responses of the dynamic simulation are much smaller than those for all other simulations, although the mean value is among the highest.

Considering the Coriolis simulation, a decrease in the average values of both the v_τ and F_t responses compared to the inertia-free solution is observed. The amplitudes are unaffected. The same diminishing effect of the Coriolis forces is observed when comparing the centrifugal and centrifugal + Coriolis simulations, meaning that the diminishing effect of the Coriolis forces is not influenced by the presence of centrifugal forces.

In contrast to Coriolis forces, inclusion of centrifugal forces leads to increased average values of v_τ and F_t compared to an inertia-free solution. This becomes apparent by comparing the centrifugal and inertia-free solutions. As the solution including both centrifugal and Coriolis terms is closer to the centrifugal solution than the Coriolis solution, the centrifugal forces are more dominant than the Coriolis forces.

This dominance of the centrifugal forces over the Coriolis forces is explained by the fact that the centrifugal terms in the absolute acceleration equation (4.26) are governed by $\frac{v_\tau^2}{r}$, while the Coriolis forces are governed by $\frac{v_\tau v_r}{r}$. As the tangential speed $v_\tau \gg v_r$ in general, the centrifugal forces are higher than the Coriolis forces.

The quasi-steady solution always lies in between the centrifugal solution and the centrifugal + Coriolis solution. This is explained by the inclusion of the Euler term in the quasi-steady solution, which halves the Coriolis force component in equation (4.26). The dominance of the centrifugal forces over the Coriolis forces in the quasi-steady solution is once again confirmed by the quasi-steady solution being closer to the centrifugal solution than the Coriolis solution.

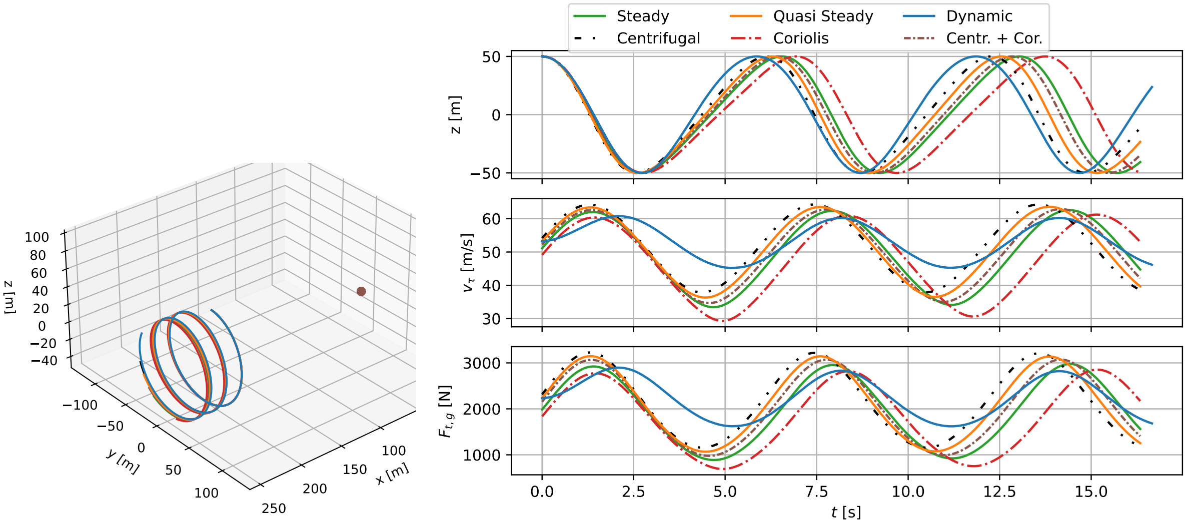

(a) Downwind circle with constant reelout speed. **(b)** Altitude (top), tangential velocity (middle) and ground tether tension (bottom) versus time.

Figure 8.1: Effect of each inertial force component on the solution for a kite flying a downwind circle with constant reelout speed $v_r = 1\,\mathrm{m\,s^{-1}}$. This kite has a mass-to-surface ratio $\frac{m}{S} = 8\,\mathrm{kg\,m^{-1}}$ and flies in an environment with gravity and a uniform wind speed $v_w = 15\mathrm{m\,s^{-1}}$. The tether drag and mass are neglected.

8.1.2. Examining the phase differences in the solutions

So far, only the differences in amplitude and average values of each solution are discussed, but also phase and frequency differences are observed in figure 8.1b. Each solution has maxima at different timestamps t, at different intervals. However, comparing the phase and frequency changes in terms of t provides little insight: it is more sensible to compare the solutions at each position along the path.

One method of doing so, is to plot the tangential speed on the y,z-plane, that is, looking 'upwind'. Figure 8.2 shows the location of the points of $v_{\tau,min}$ and $v_{\tau,max}$ on this plane, for each simulation. To obtain a fair comparison, the data points in figure 8.2 are filtered between $2\pi < s \leq 4\pi$, that is, the tangential speed along the second[1] full circle are plotted.

Figure 8.2 shows how the inertia-free and Coriolis solutions predict the point of maximum velocity located in the lower half of the circle, albeit quite subtle. The centrifugal, centrifugal + Coriolis, and quasi-steady solutions all predict this point slightly higher in the circle. That is, the phase of the quasi-steady v_τ is leading the inertia-free v_τ response, in terms of the path coordinate s.

However, most notable is the difference in locations of the $v_{\tau,max}, v_{\tau,min}$-points considering the dynamic solution. The points are located respectively much lower and higher in the circle. The dynamic v_τ lags the inertia-free v_τ by a significant amount.

[1]The first circle is skipped to ensure that any transient caused by the initial conditions has fully decayed.

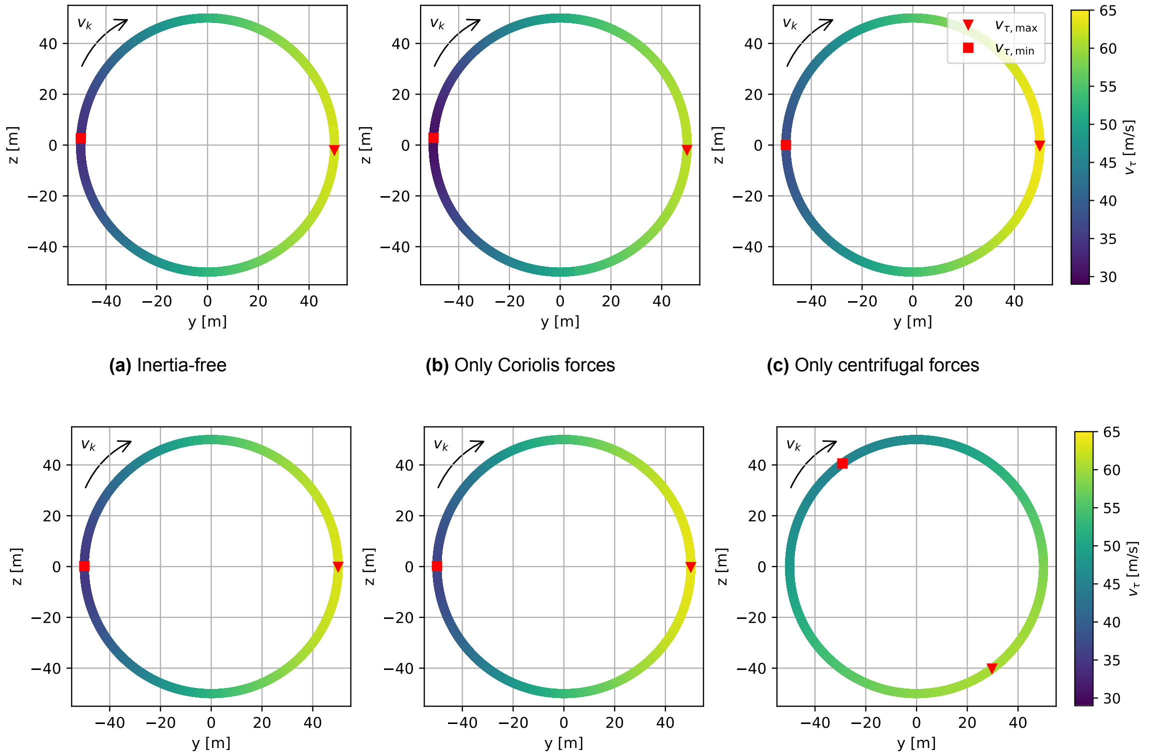

(a) Inertia-free **(b)** Only Coriolis forces **(c)** Only centrifugal forces

(d) Coriolis and centrifugal forces **(e)** Quasi-steady **(f)** Dynamic

Figure 8.2: Locations of the maximum and minimum tangential speed points in the (y, z)-plane for various formulations of the force equilibrium equations.

The phase of a point can be quantified by multiplying the path coordinate s with the maneuver frequency ω, resulting in equation (8.1). Then, the phase shift between e.g., the dynamic and inertia-free solutions becomes equation (8.2), which has the unit rad.

$$\Phi \equiv \omega s \tag{8.1}$$

$$\Delta\Phi_{v_\tau,\text{max}}\Big|_{\text{dyn, if}} = \omega\left(s_{v_\tau,\text{max}}\Big|_{\text{dyn}} - s_{v_\tau,\text{max}}\Big|_{\text{if}}\right) \tag{8.2}$$

For the example in figure 8.2, the phase shifts are given in table 8.1. It becomes apparent that the phase shifts actually represent the angle between the two speed maxima, measured along the x-axis. For an elevated parameterization, this angle would be measured along the elevated x'-axis.

To conclude this section, the Coriolis forces have a diminishing effect on the average kite velocity and tether tension and cause a subtle phase delay of the kite velocity response measured in s. In the contrary, more dominant centrifugal forces increase the average kite velocity and tether tensions, and cause a phase lead of the kite velocity. The amplitudes of the velocity and tether tension responses

Resolved inertial terms	**Phase $\Phi_{v_\tau,\text{max}}$**	**Phase shift $\Delta\Phi_{v_\tau,\text{max}}\big\|_{\text{if}}$**
Inertia-free	92.012°	n/a
Coriolis	92.142°	0.130°
Centrifugal	90.182°	-1.830°
Coriolis + Centrifugal	90.291°	-1.721°
Quasi-steady	90.237°	-1.775°
Dynamic	143.322°	51.310°

Table 8.1: Tangential speed phase and phase shift w.r.t. the inertia-free solution, for simulations with varying resolved inertial terms.

are marginally affected by the Coriolis and centrifugal acceleration terms, but much more significantly by the $\dot{v}_\tau, \dot{v}_r$-acceleration. These terms have a dampening effect on the velocity and kite responses, affect the average values, and introduce a most significant phase delay of the responses over the path coordinate s.

8.2. Other effects of dynamic simulation

The inclusion of inertia also affects other aspects. Since the dynamic model resolves the mass damping, a dynamic solution contains a transient and an asymptotic part, whereas a quasi-steady solution does not have a transient. Less obvious, but nonetheless significant, are the increased solution smoothness and enlarged solution space for a dynamic simulation.

8.2.1. Transient and asymptotic parts in the solution

Already briefly mentioned in section 7.2, the dynamic simulation of kite motion along a parameterized path requires defining the initial conditions t_0, s_0 and $\dot{s}_0$. The value of $\dot{s}_0$, which follows from the initial kite speed $v_{k,0}$, strongly influences the system response.

The solution component that is affected by the initial conditions forms the transient part of the solution. For a downwind circle with constant tether length in an environment without gravity, the asymptotic part is governed by the condition $\ddot{s} = 0$. One can quantify the decay of the transient part by the half-life path coordinate $s_{1/2}$, which is the value for s at which $\ddot{s} = \frac{1}{2}\ddot{s}_0$.

Figure 8.3 shows the half-life coordinates $s_{1/2}$ for kites with varying mass-to-surface ratios flying downwind circles in an environment with no gravity. The tether drag and mass are both 0. Figure 8.3 shows that the half-life is significantly larger for heavier kites. For this case, the half-life coordinate scales approximately linear with the mass-to-surface ratio.

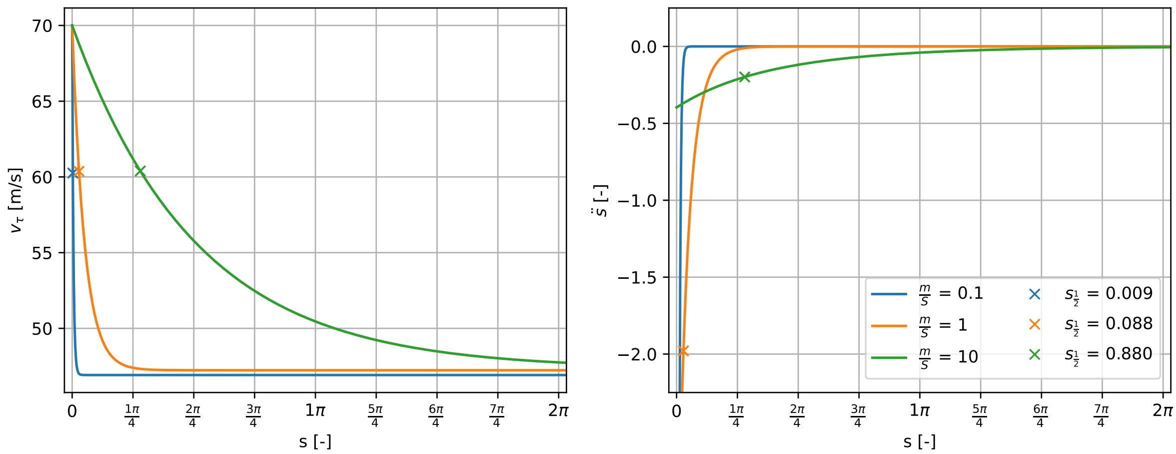

Figure 8.3: The decay of the transient can be quantified by the half-life $s_{1/2}$, which depends strongly on the mass-to-surface ratio $\frac{m}{S}$. These results are obtained for a perfect downwind circle with a dragless tether of constant length, in an environment with a uniform wind speed and no gravity. A value of $s = 2\pi$ means that one circle has been completed.

Following the discussion in section 8.1.2, the phase of the half-life point can be defined by equation (8.3). For this example, where $\omega = 1\,\mathrm{rad\,s^{-1}}$, the phase difference between the s_0-point and the $s_{1/2}$-point is $0.54°$ for the kite with $S/m = 10$, and $54.4°$ for the kite with $S/m = 0.1$.

$$\phi_{1/2} \equiv \omega s_{1/2} \tag{8.3}$$

The short half-life coordinate for the light-weight kite suggests that any perturbation would decay quick enough to validate not resolving the transient response. However, this may not be the case for a heavy kite. This strong dependency of the half life coordinate on the kite mass-to-surface ratio suggests that there is a certain mass ratio below which any perturbation decays quickly enough to validate assuming quasi-steadiness.

8.2.2. Increased smoothness of the dynamic solution

The kite inertia also affects the smoothness of the solution. This is illustrated in figure 8.4, which shows the dynamic response of a kite in an environment with gravity and uniform wind speed, flying an elevated figure eight pattern with constant reelout speed. The drag of the tether is ignored, and the quasi-steady velocity is used for the initial conditions. The figure shows the dynamic time responses of the tangential speed and the ground tether tension in blue. The quasi-steady solution at each position is plotted in orange.

Figure 8.4 shows that for this specific example, the quasi-steady tether tension peaks at the points where the kite has transitioned from flight towards Zenith, into flight towards the negative or positive azimuth directions. These peaks can be explained by the steep slope of the quasi-steady tangential velocity at these locations, increasing the aerodynamic forces and thus the overall loading on the system.

Since the dynamic model resolves the kite inertia, the tangential velocity varies slower, resulting in a smoother tether tension solution.

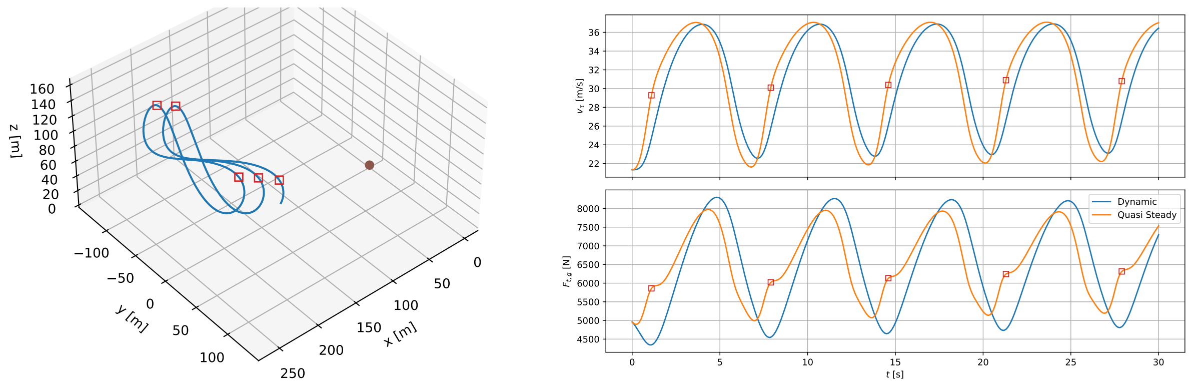

(a) Elevated figure-eight with constant reelout. **(b)** Tangential velocity (top) and tether tension (bottom) versus time.

Figure 8.4: Smoothness of solution depends on which inertial terms are resolved. A peak in tether tension is observed in the quasi-steady solution at the positions marked red. These peaks are not present in the dynamic solution.

8.2.3. Enlarged solution space of the dynamic simulation

The quasi-steady condition $\dot{v}_\tau = \dot{v}_r = 0$ cannot always be satisfied, as was briefly discussed by Noom [14]. Van Der Vlugt et al. furthermore showed examples for which no inertia-free solution could be found by their solver [15]. Why the (quasi)-steady condition restricts the solution space, has to do with the coupling between the aerodynamic force and kite velocity.

As discussed in more detail in section 5.2, the aerodynamic force only varies in magnitude with the apparent wind velocity, and by definition, it lies in the $\mathbf{e}_{n'}, \mathbf{e}_{r'}$-plane. The orientation of $\mathbf{F_a}$ in this plane is quantified by the aerodynamic roll angle ϕ_a.

These restrictions mean that for a given kite position (ϕ, β, r) and kite velocity (v_τ, v_r, χ), the components of the aerodynamic force in the course, normal and radial directions are coupled. That is, there is a limit to how much aerodynamic force can be generated in the course direction versus the normal direction, for a certain kite orientation and speed.

When considering the quasi-steady equations of motion in equation (2.6), it becomes apparent that this coupling between $F_{a,\tau}, F_{a,n}$ and v_τ dictates a relationship between $v_\tau \dot{\chi}$ and v_τ, i.e. a relationship between the normal acceleration and the tangential speed. The course angle rate of change $\dot{\chi}$ is thus coupled to the tangential velocity v_τ and the aerodynamic roll ϕ_a. And since $0 \leq \phi_a \leq 2\pi$, there is a limit to the path's curvature in the tangential plane for which a quasi-state exists.

To define this curvature, we introduce the tangential turn radius r_τ as the radius of the hypothetical circle in the tangential plane τ that the kite would travel, given a constant tangential speed v_τ and rotation rate around the $\mathbf{e}_r$ vector. Equation (8.4) shows the definition of r_τ, which follows from equation (4.21). The norm is taken to ensure a positive tangential turn radius, independent of the turn direction.

$$r_\tau \equiv \left\| \frac{v_\tau}{\boldsymbol{\Omega}_C \cdot \mathbf{e}_r} \right\| = \left\| \frac{r v_\tau}{v_\tau \sin\chi \tan\beta - r\dot{\chi}} \right\| \quad (8.4)$$

For any given kite position and direction, there exists a value for $r_\tau < r_{\tau,min}$ at which the path becomes too curved for a quasi-steady solution to exist. The value of $r_{\tau,min}$ depends on many quantities, such as the kite position, direction, mass, surface, wind speed and gravity.

Example of the minimum tangential quasi-steady turning radius for a downwind kite

A hill climb optimization algorithm can be used to find the value of $\dot{\chi}$ that yields the smallest tangential turn radius for a given kite configuration and direction.

The algorithm starts with a value of $\dot{\chi}$ that matches a great circle path, i.e. $r_{\tau,min} = \infty$. The value of $\dot{\chi}$ is then increased iteratively, with each iteration resulting in a decreased r_τ and v_τ. After some number of iterations, the decrease in v_τ is substantially large, and r_τ does not decrease anymore for increasing $\dot{\chi}$. It is assumed that this obtained local minimum is the global minimum, $r_{\tau,min}$.

This hill climbing algorithm was used to obtain the distributions of $r_{\tau,min}$ over the sphere spanned by a constant tether length for kites with varying mass-to-surface ratio $\frac{m}{S}$, presented in figure 8.5. For these simulations, the tether mass and drag were neglected, gravity was included, and a uniform wind speed $v_w = 10\,\mathrm{m\,s^{-1}}$ was used. Furthermore, the a downwind kite direction was imposed, i.e. χ is such that $v_{w,\tau} < 0, v_{w,n} = 0$, explaining the quasi-axisymmetrical distributions in figure 8.5.

Figure 8.5 shows how the minimum tangential turn radius is greatly affected by the azimuth and elevation angles: at the edges of the downwind window, the minimum turn radius quickly grows to infinity, after which no quasi-steady solution exists regardless of $r_{\tau,min}$. Closer to the downwind axis, the value for $r_{\tau,min}$ is in the order of several meters. The blue ring in figure 8.5a and yellow ring in figure 8.5b show the presence of local minimum in the minimum turning radius.

The isocontours of constant $r_{\tau,min} = 10\,\mathrm{min}$ in each subplot of figure 8.5, furthermore show how the mass-to-surface ratio significantly affects the minimum turn radius. For a kite with $\frac{m}{S} = \frac{1}{2}\,\mathrm{kg\,m^{-2}}$, the minimum turn radius $r_{\tau,min} < 10\,\mathrm{m}$ for the majority of the downwind window, while for a kite with $\frac{m}{S} = 2\,\mathrm{m\,kg^{-1}}$, this condition is only satisfied for a small portion of the downwind window.

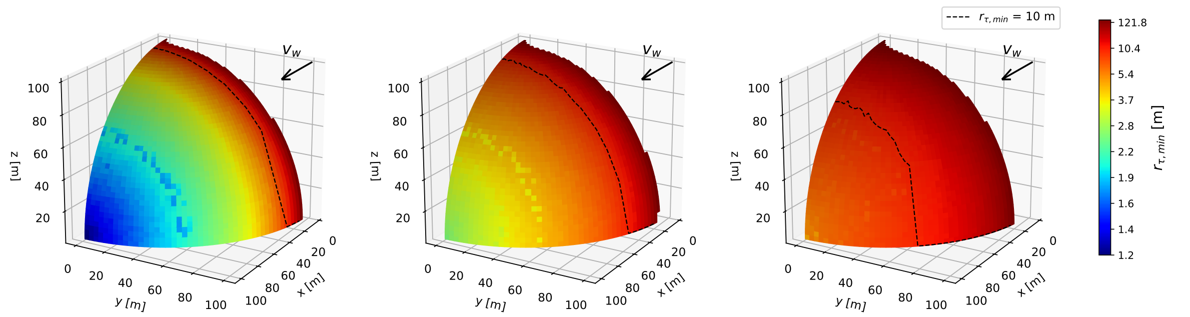

(a) $\frac{m}{S} = \frac{1}{2}\,\mathrm{kg\,m^{-2}}$ **(b)** $\frac{m}{S} = 1\,\mathrm{kg\,m^{-2}}$ **(c)** $\frac{m}{S} = 2\,\mathrm{kg\,m^{-2}}$

Figure 8.5: Distribution of the minimum tangential turn radius $r_{\tau,min}$, for various mass-to-surface ratios $\frac{m}{S}$. No quasi-steady solution exists for paths curved more strongly. For this simulation, a uniform wind speed of $12\,\mathrm{m\,s^{-1}}$ was used, gravity was included and a tether with constant length and without drag or mass was used. At any position, the course angle χ was such the kite was flying 'downwind'. Note the inverse linear scale on the color bar.

For a dynamic simulation, the solution space is larger. Since it is allowed to allowed to have $\dot{v}_\tau \neq \dot{v}_r \neq 0$, the coupling between v_τ and $\dot{\chi}$ is less strict, resulting in an enlarged solution space.

Figure 8.6 shows an example where there a quasi-steady solution could be found only at specific locations along the trajectory. The segment at which no quasi-steady solution was found is marked red in figure 8.6a. At this position, the path curvature is such that the quasi-steady solver in algorithm 2 could not find a combination of $\dot{s}, F_t, \phi_a$ that would satisfy the quasi-steady equations of motion.

At this location, the kite velocity becomes small. Somewhat counterintuitive: the value of $\dot{v}_\tau$, obtained with the dynamic model, is relatively close to 0 in the segment for which the quasi-steady solver fails to find a solution.

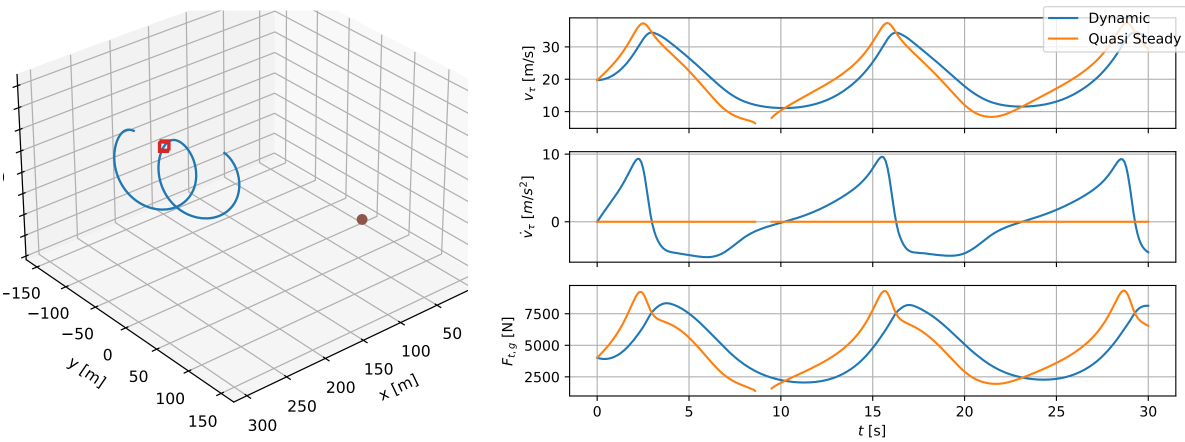

(a) Elevated circle with relatively high constant reelout speed.

(b) Tangential velocity (top), its time derivative (middle), and the tether tension (bottom) versus time.

Figure 8.6: Dynamic simulation of a kite flying an elevated circle with a relatively high constant reelout speed v_r. A quasi-steady solution could not be found in the segment marked in red.

8.3. Solution space comparison

Section 8.1 identified that the inertial terms affect the tangential speed v_τ and tether tension F_t responses in terms of average value, amplitude and phase. This section aims to provide insight in how these phenomena scale with varying kite configurations.

For this analysis, an elevated helix with path elevation angle $\beta_P = 30°$ is simulated, for varying kite mass-to-surface ratios, reelout speeds, helix radii, and lift-to-drag ratios. Gravity is included, and a uniform wind speed of $v_w = 10\,\mathrm{m\,s^{-1}}$ is used. The kite has a fixed drag coefficient of $c_d = 0.2$, the lift coefficient is determined through the lift-to-drag ratio. More details on the used simulation quantities are provided in appendix A. The simulations are run for radial distances $200\,\mathrm{m} \leq r < 400\,\mathrm{m}$ and cut-off time $t_1 = 400\,\mathrm{s}$. Any simulation result that has not converged, or in which the kite did not manage to complete one full circle, is discarded. Tether drag and mass are ignored, such that the assumption of an inertia-free tether does not affect the observed differences in the model solutions.

Three quantities are compared for this input space. The normalized average traction power $\frac{\bar{P}}{S}$, calculated by equation (8.5), quantifies how the response mean values are affected. The velocity peak-to-peak amplitude Δv_τ quantifies how the response extrema are affected. This value is calculated for the first completed circle, per equation (8.6). Finally, the phase of the point of maximum velocity $\Phi v_{\max}$ is calculated by equation (8.7) to quantify how the phase shifts with varying inputs, also for the first circle.

$$\frac{\bar{P}}{S} = \frac{1}{S}\frac{\Delta t \sum_{t_0}^{t_1} F_{t,g,r}(t) v_r(t)}{t1 - t0} \tag{8.5}$$

$$\Delta v_\tau \equiv v_{\tau,\max} - v_{\tau,\min} \qquad \text{for} \quad 0 < s \leq 2\pi \tag{8.6}$$

$$\Phi_{v_{\tau,\max}} \equiv \omega s_{v_{\max}} \qquad \text{for} \quad 0 < s \leq 2\pi \tag{8.7}$$

In the following subsections, the wing-surface normalized average traction power $\frac{\bar{P}}{S}$, the peak-to-peak tangential speed amplitude Δv_τ, and the phase of the maximum tangential speed point $\Phi v_{\tau,\max}$ are plotted on three planes: the $\frac{m}{S}, v_r$-plane, the $\frac{m}{S}, r_h$-plane and the $\frac{m}{S}, E$-plane. The locations of these planes in the input space are listed in table 8.2.

Table 8.2: Locations of the analyzed planes in the input space.

Plane	Radial speed v_r [m s^{-1}]	Helix radius r_h [m]	Lift-to-drag ratio E [-]
(m, v_r)	n/a	40	4
(m, r_h)	3	n/a	4
(m, E)	3	40	n/a

8.3.1. Sensitivity of the normalized average traction power

This subsection presents the sensitivity of the normalized average traction power $\frac{\bar{P}}{S}$ for each model, and compares the three models. However, this comparison is not straightforward. For the same inputs, the models predict different kite speeds and therefore a different location when the maximum tether length has been reached. This causes wrinkles in the model error solution space presented in this section. An alternative would be to compare the average traction powers over the same number of completed maneuvers, but also this has a flaw: in a real world application, the flight path is controlled by the tether length, not by a strict number of completed maneuvers. The tether length required so fly a number of maneuvers can vary greatly depending on the kite and operational quantities.

Sensitivity to reeling speed

Figure 8.7 shows the normalized average power $\frac{\bar{P}}{S}$ of the dynamic model on the m, v_r-plane, and how the inertia-free and quasi-steady models compare. The grey blocks in figures 8.7b and 8.7c represent the inputs for which a dynamic solution was found, but no (quasi-)steady solution.

An optimal reeling speed $v_{r,\text{opt}} \approx 3\,\text{m}\,\text{s}^{-1}$ for which the average power is maximized for a certain kite mass is visible in figure 8.7a. This corresponds to a reeling factor $f = 0.3$, which is close to the 2D optimal reeling factor $f = \frac{1}{3}$ presented by Luchsinger [26]. A subtle decrease in optimal reeling speed for increasing kite mass is present in the solution. At the feasibility boundary of v_r, i.e. the value of v_r beyond which no solution is obtained for a specific $\frac{m}{S}$, the average power drops drastically. At such high feeling speed, the tether tension and tangential speed in the upward segment of the circle are low, meaning that little power is generated for a significant duration.

Figure 8.7b shows that the inertia-free model predicts up to 10% lower average power than the dynamic model, with the greatest difference obtained for high kite masses. The quasi-steady model predicts higher $\frac{\bar{P}}{S}$ than the dynamic model for high reel-out speeds, and lower $\frac{\bar{P}}{S}$ for low reel-out speeds. For this kite and path configuration, the difference between the quasi-steady and dynamic model ranges between ± 5%, but is limited to < 1% for kites with a mass-to-surface ratio $\frac{m}{S} = 1\text{kg}\,\text{m}^{-2}$.

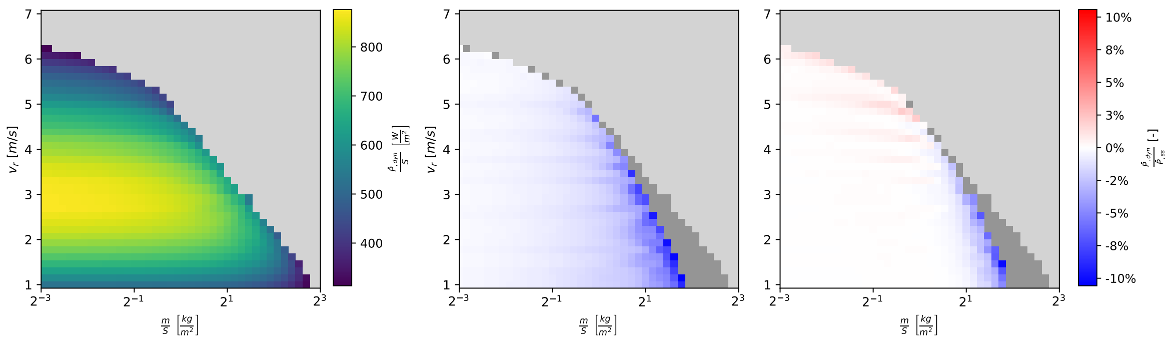

(a) Dynamic **(b)** Inertia-free versus dynamic **(c)** Quasi-steady versus dynamic

Figure 8.7: Average power on the m, v_r-plane for the dynamic model (left). Figures 8.8b and 8.8c show how the inertia-free and quasi-steady models compare to the dynamic model.

Sensitivity to path curvature

Figure 8.8 shows the average power distribution for the dynamic simulation and the differences with the inertia-free and quasi-steady models.

Figure 8.8a shows that lighter kites flying tighter turns, produce more power. The range of r_h for which a solution is found, decreases with increasing kite mass. Several local optima are found in the helix radius for each kite mass, indicated by the near-horizontal lines in figure 8.8a. These are the result of the simulation termination criteria. As the simulation is terminated when the radial distance reaches r_{max}, the value of s_max changes with r_h, that is, the number of completed maneuvers in the same tether length range varies with r_h, explaining the local optima.

The inertia-free model is compared to the dynamic model in figure 8.8b. Over the majority of the input space, the inertia-free model yields lower $\frac{\bar{P}}{S}$, especially for high kite mass. However, at the feasibility boundary $r_{h,min}$, the inertia-free model yields higher $\frac{\bar{P}}{S}$ than the quasi-steady and dynamic models, by up to +10%. There is an indication that for tight turns, the centrifugal forces significantly reduce the tether force.

Figure 8.8c shows the difference between the quasi-steady and dynamic $\frac{\bar{P}}{S}$ solutions. For heavy kites flying tight turns, the quasi-steady model underestimates the average power. Near the $r_{h,max}$-boundary, the quasi-steady model overestimates the average power. The solution space of the quasi-steady model is notably smaller than that of the dynamic model, highlighted by the grey markers.

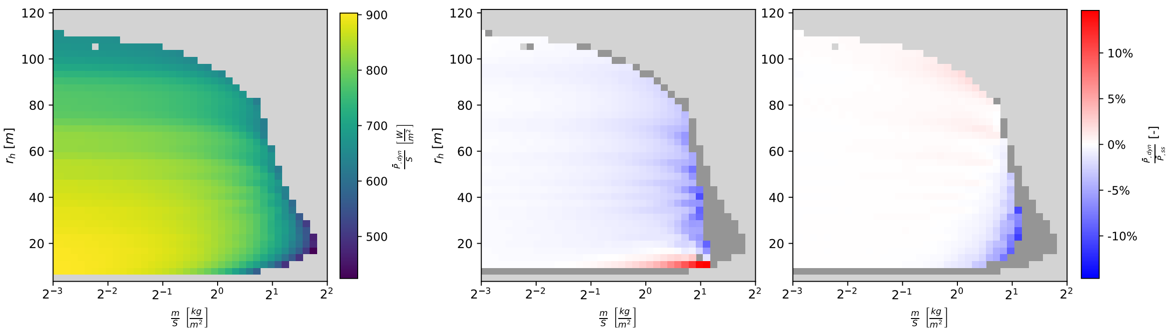

(a) Dynamic **(b)** Inertia-free versus dynamic **(c)** Quasi-steady versus dynamic

Figure 8.8: Average power on the m, r_h-plane for the dynamic model (left). Figures 8.8b and 8.8c show how the inertia-free and quasi-steady models compare to the dynamic model.

Sensitivity to lift-to-drag ratio

The average normalized power $\frac{\bar{P}}{S}$ on the m, E-plane is plotted in figure 8.9. For a non-maneuvering downwind kite, Loyd showed that the traction power scales with $\frac{C_L^3}{C_D^2}$ [2]. Figure 8.9a acknowledges a strong dependency of $\frac{\bar{P}}{S}$ on E.

The inertia-free and quasi-steady average power are compared with the dynamic average power in figures 8.9b and 8.9c. The previously discussed wrinkles in the solution space are even more pronounced on the m, E-plane. The inertia-free model again underestimates the power generation, compared to the dynamic model. This is most notable for heavier kites. The quasi-steady model underestimates the power produced by heavy kites with high E, but overestimates may overestimate the power for a more light-weight kite. The difference in $\frac{\bar{P}}{S}$ between the quasi-steady model and dynamic model are relatively subtle ($\pm 5\%$), but not straightforward to determine a priori.

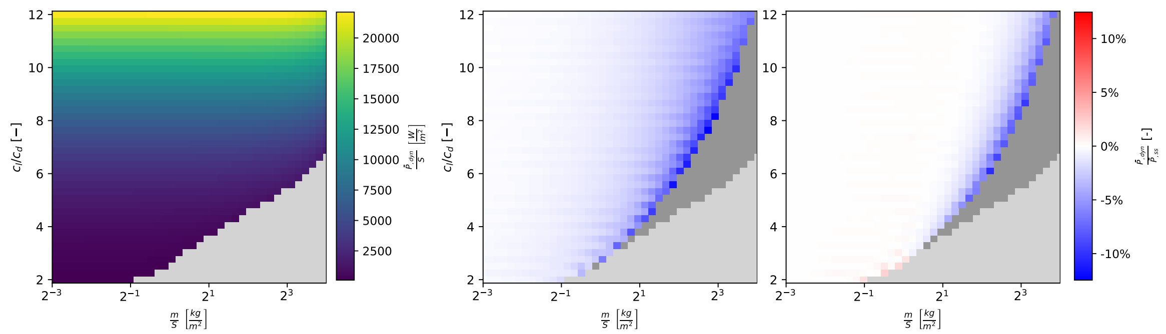

(a) Dynamic **(b)** Inertia-free versus dynamic **(c)** Quasi-steady versus dynamic

Figure 8.9: Average power on the m, E-plane for the dynamic model (left). Figures 8.8b and 8.8c show how the inertia-free and quasi-steady models compare to the dynamic model.

8.3.2. Sensitivity of the tangential speed variation

This section presents the sensitivity of the variation in tangential speed Δv_τ along the first maneuver for each model, and compares the models. At the feasibility boundaries of the solution space, the difference in Δv_τ of the inertia-free and quasi-steady models with respect to the dynamic models becomes substantially large.

Sensitivity to reeling speed

The sensitivity of the variation in tangential speed Δv_τ along the first maneuver to the reeling speed and mass is depicted in figure 8.10. Figure 8.10a shows Δv_τ on the m, v_r-plane, and the comparison with the inertia-free and quasi-steady models is given in figures 8.10b and 8.10c.

Figure 8.10b shows that the variation in tangential speed grows rapidly near the $v_{r,max}$ feasibility boundary, especially for higher kites. The inertia-free and quasi-steady models in figures 8.10b and 8.10c, predict even greater Δv_τ , with an error of >30% (!). For a kite with $\frac{m}{S} = 1$, the inertia-free and quasi-steady models yield respectively +10% and +5% higher Δv_τ for all v_r, compared to the dynamic model. The difference in Δv_τ between the inertia-free and quasi-steady models is small, compared to the difference to the dynamic model.

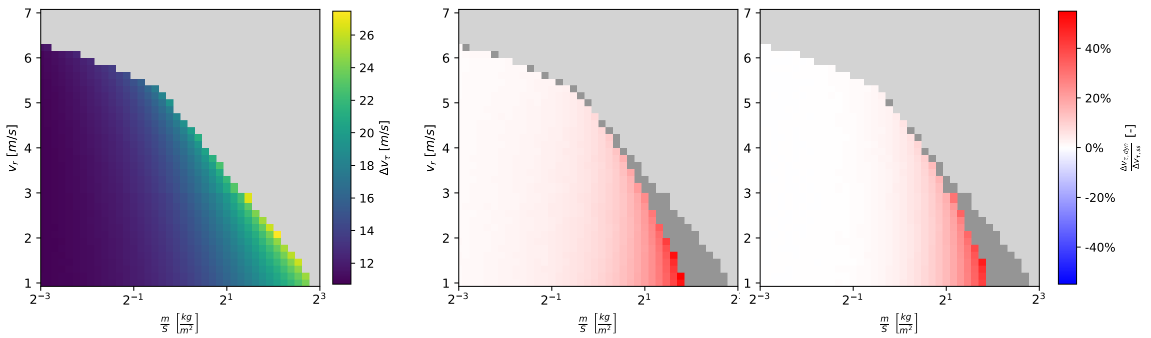

(a) Dynamic **(b)** Inertia-free versus dynamic **(c)** Quasi-steady versus dynamic

Figure 8.10: Variation in the tangential speed Δv_τ along the first completed maneuver, on the m, v_r-plane for the dynamic model (left). The inertia-free and quasi-steady models are compared to the dynamic model in figures 8.10b and 8.10c.

Sensitivity to path curvature

The sensitivity of the tangential speed variation Δv_τ to the path curvature is shown in figure 8.11. The variation in tangential speed for a given kite mass is largest at the $r_{h,max}$ feasibility boundary, and smallest towards the $r_{h,min}$ feasibility boundary.

The difference between the dynamic, inertia-free and quasi-steady models is respectively given in figures 8.11b and 8.11c. The differences at the $r_{h,max}$ feasibility boundary are small compared to the differences at the $r_{h,min}$ boundary. The inertia-free and quasi-steady models yield significantly higher tangential speed variations, compared to the dynamic model. For heavy kites flying tight turns, the difference in Δv_τ with to dynamic model ranges up to +60% and +20% for the inertia-free and quasi-steady models.

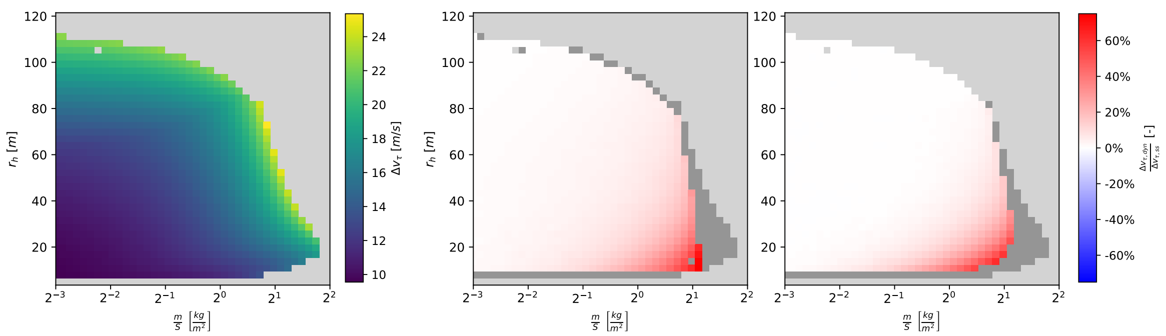

(a) Dynamic **(b)** Inertia-free versus dynamic **(c)** Quasi-steady versus dynamic

Figure 8.11: Variation in the tangential speed Δv_τ along the first completed maneuver, on the m, r_h-plane for the dynamic model (left). The inertia-free and quasi-steady models are compared to the dynamic model in figures 8.11b and 8.11c.

Sensitivity to lift-to-drag ratio

Figure 8.12b shows the sensitivity of the tangential speed variation Δv_τ to the lift-to-drag ratio and kite mass. The solution space of the dynamic model is plotted in figure 8.12a, the respective differences of the inertia-free and quasi-steady models with the dynamic model are shown in figures 8.12b and 8.12c.

Figure 8.12a shows an interesting pattern. Close to the m_{max} feasibility boundary, the tangential speed variation is the largest. Local minima in the solution of Δv_τ exist at low m, low E, and at high m, high E. The effect of the kite mass on Δv_τ is minimal for $E \approx 8$.

The inertia-free and quasi-steady models are compared to the dynamic model in figures 8.12b and 8.12c. Again, note the difference in the size of the solution space of these models with respect to the dynamic model. Near the m_{max} feasibility boundary, neither the inertia-free nor the quasi-steady models provide solutions, whereas the dynamic model resolves an ever-increasing Δv_τ . One hypothesis is that the dynamic model accounts for the necessary exchange between the kite's kinetic and potential energy, allowing it to overcome segments of the trajectory that require such energy exchange. In contrast, the inertia-free and quasi-steady models do not account for this momentum exchange.

The difference in Δv_τ obtained with each model grows very rapidly with increasing m. Compared to the dynamic model, the obtained Δv_τ is up to 3 and 2 times larger for the inertia-free and quasi-steady model.

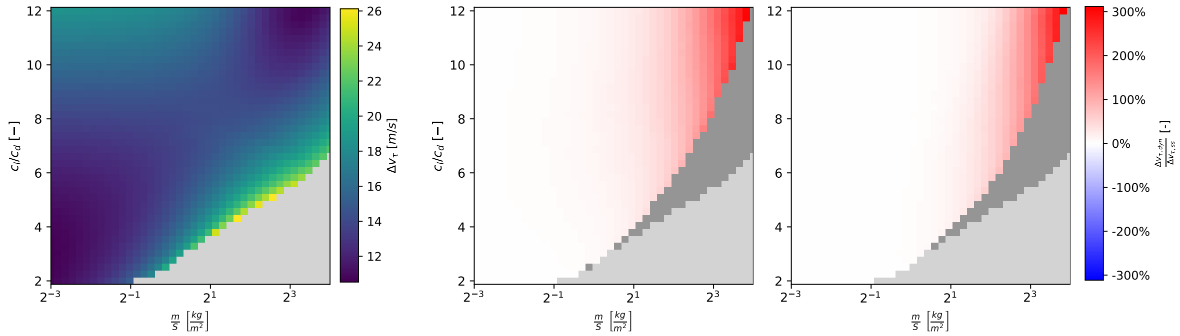

(a) Dynamic **(b)** Inertia-free versus dynamic **(c)** Quasi-steady versus dynamic

Figure 8.12: Variation in the tangential speed Δv_τ along the first completed maneuver, on the m, r_h-plane for the dynamic model (left). The inertia-free and quasi-steady models are compared to the dynamic model in figures 8.12b and 8.12c.

8.3.3. Sensitivity of the phase of the velocity response

So far, the sensitivity of the solution average values and the sensitivity of the solution amplitudes has been assessed. This section focuses on the phase differences in the solutions between the inertia-free, quasi-steady and dynamic models.

Sensitivity to reeling speed

Figure 8.13 shows the phase of the maximum velocity point $\Phi_{v_\tau,\text{max}}$ for the inertia-free, quasi-steady and dynamic models on the m, v_r plane. The patterns in the solutions are substantially different for each model.

The dynamic model in figure 8.13d shows the most complex solution space shape. For increasing reeling speed, $\Phi_{v_\tau,\text{max}}$ becomes smaller. The highest values for $\Phi_{v_\tau,\text{max}}$ are found for small kite masses with low reeling speeds, and for high kite masses. Both the inertia-free and quasi-steady models in figures 8.13b and 8.13c do not show this increase in $\Phi_{v_\tau,\text{max}}$ for higher kite mass. In contrary, they model show the lowest values for $\Phi_{v_\tau,\text{max}}$ near the kite mass feasibility boundary, which seems unrealistic. Furthermore, the quasi-steady model shows little dependency of $\Phi_{v_\tau,\text{max}}$ with the reeling speed, although this dependency on v_r is more pronounced in the inertia-free and dynamic solutions.

The differences in the $\Phi_{v_\tau,\text{max}}$ values are plotted in figures 8.13d to 8.13f for the quasi-steady and dynamic models. Over the entire analyzed solution space, the inertia-free model predicts a delayed phase of $\Phi_{v_\tau,\text{max}}$ with respect to the quasi-steady model, confirming the conclusion in section 8.1 that the inclusion of centrifugal advances the phase of the tangential speed response in time.

The dynamic tangential velocity is lagging the inertia-free and quasi-steady solutions for all $\frac{m}{S}$. For $\frac{m}{S} < 1$, this lag is subtle, in the order of $\mathcal{O}(10^0)$ degrees. But, for $\frac{m}{S} > 1$, the phase shift can become as big as $35°$, which for the used helix radius $r_h = 40$ m translates to a distance of ≈ 25 m along the trajectory.

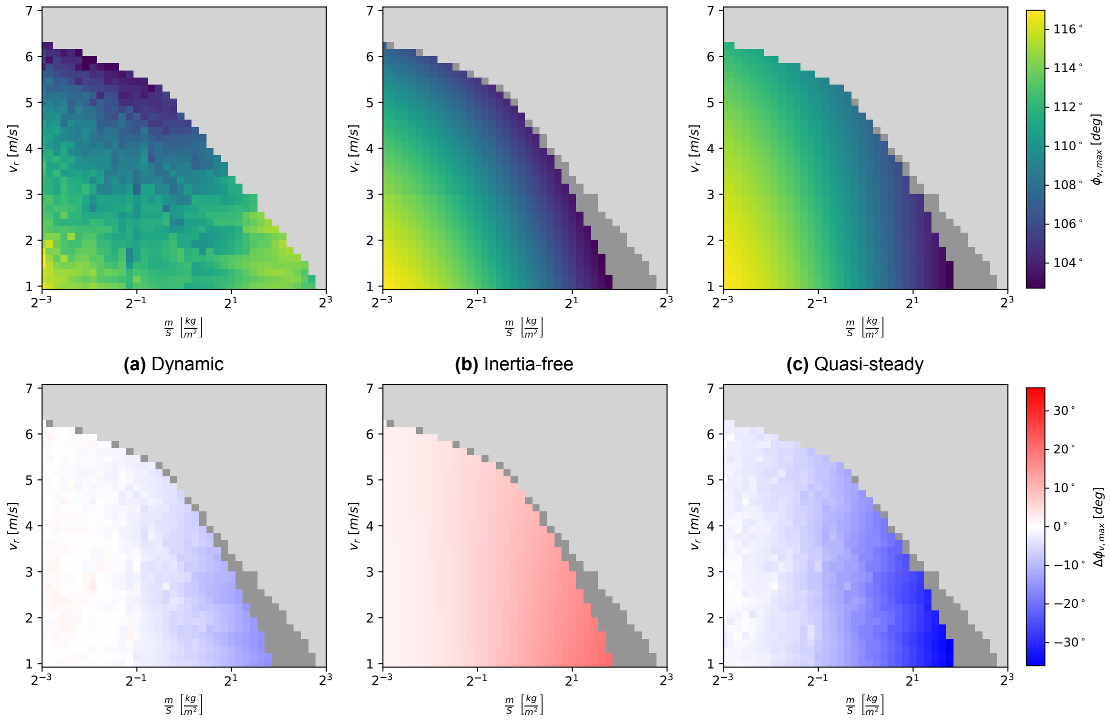

(a) Dynamic **(b)** Inertia-free **(c)** Quasi-steady

(d) Inertia-free versus dynamic **(e)** Inertia-free versus quasi-steady **(f)** Quasi-steady versus dynamic

Figure 8.13: Phase of the maximum tangential speed point $\Phi_{v_\tau,\text{max}}$ on the m, v_r-plane, for the inertia-free, quasi-steady and dynamic models. The phase shifts between each model are plotted in the bottom row.

Sensitivity to path curvature

The phases of the maximum velocity point on the m, r_h-plane are plotted for the inertia-free, quasi-steady, and dynamic models in figure 8.14.

The most lagging phases are obtained for lightweight kites flying loose turns, and the most advanced phases are for heavy kites flying tight turns. Under conditions of tighter turns, characterized by increased centrifugal forces, the quasi-steady $\Phi_{v_\tau,\text{max}}$ is more advanced than the dynamic solution, resulting in the increasingly negative phase difference compared to the inertia-free and dynamic model shown in figure 8.14c. The difference between the inertia-free and dynamic models is relatively subtle, compared to the difference with the quasi-steady model.

For specific turn radii, i.e., $20 < r_h < 50$, the dynamic model predicts a slight phase delay for increasing mass, underscoring its distinct response to high centrifugal force conditions compared to the quasi-steady model.

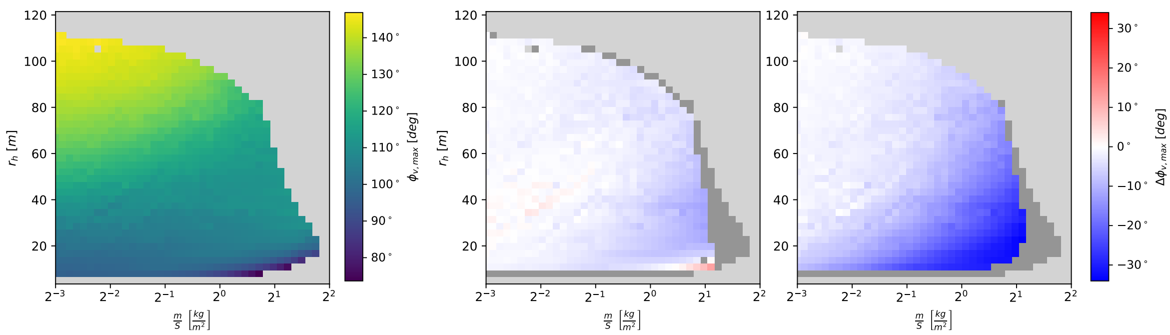

(a) Dynamic **(b)** Inertia-free versus dynamic **(c)** Quasi-steady versus dynamic

Figure 8.14: Phase of the maximum tangential velocity point $\Phi_{v_\tau,\text{max}}$ on the on the m, r_h-plane for the dynamic model. The inertia-free and quasi-steady models are compared to the dynamic model in figures 8.14b and 8.14c.

Sensitivity to lift-to-drag ratio

The phases for the inertia-free, quasi-steady and dynamic models are plotted on the m, E-plane in figure 8.15. The profiles for each model are very distinct.

The quasi-steady model shows a sharp discontinuity of the phase for high lift-to-drag ratios, a feature resolved weaker by both the inertia-free and dynamic models. Figures 8.15d to 8.15f show that the phase error between the inertia-free and dynamic model is smaller than the phase error between the quasi-steady and dynamic model.

The phase of the quasi-steady model can be advanced by more than $80°$ with respect to the dynamic model. In section 8.1, a smaller phase difference between was observed. A potential explanation for this large difference is that for these analyses, an elevated circle is simulated instead of a downwind circle.

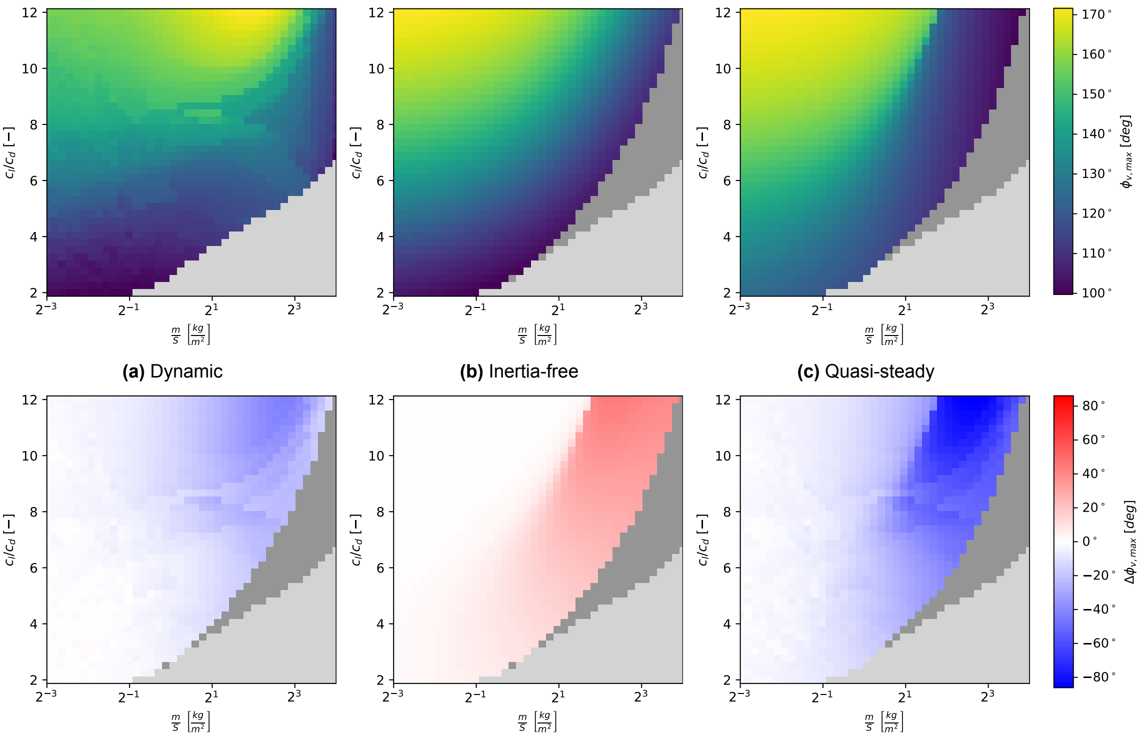

(a) Dynamic **(b)** Inertia-free **(c)** Quasi-steady

(d) Inertia-free versus dynamic **(e)** Inertia-free versus quasi-steady **(f)** Quasi-steady versus dynamic

Figure 8.15: Phase of the maximum tangential speed point $\Phi_{v_\tau,\text{max}}$ on the m, E-plane, for the inertia-free, quasi-steady and dynamic models. The phase shifts between each model are plotted in the bottom row. Per row, the same color scale is used for the three subplots.

8.4. Sensitivity to wind conditions

A uniform wind speed has been used in all previous analyses. Although the error in power between the quasi-steady and dynamic models is relatively small across the majority of the input space, a significant phase difference of the point of maximum velocity has been observed. If the wind speed is nonuniform, does this phase difference lead to an increased error in the average power estimation?

8.4.1. Impact of the mean wind speed profile

The impact of the mean wind speed profile on the power error can be estimated by comparing the error between the quasi-steady and dynamic models considering a uniform wind speed, to the error between the two models for a logarithmic wind speed profile.

Figure 8.16 illustrtes the distributions of the difference in the power errors across the entire analyzed solution space, grouped by mass-to-surface ratio. Each node in the boxplot is calculated by equation (8.8), where the logarithmic wind speed is calculated with the log law by Stull [16], using $h_ref = 100\,\text{m}$ and $h_0 = 0.005\,\text{m}$.

$$\Delta\epsilon_{P,\text{log-unif}} = \left\| \frac{\bar{P}_{\text{dyn}}}{\bar{P}_{\text{qs}}}\Big|_{\text{log}} - \frac{\bar{P}_{\text{dyn}}}{\bar{P}_{\text{qs}}}\Big|_{\text{unif}} \right\| \tag{8.8}$$

Figure 8.16 reveals how the average power error between the dynamic and quasi-steady models changes with the mean wind speed profile. Up to a mass-to-surface ratio of $\frac{m}{S} = 1\,\text{kg}\,\text{m}^{-2}$, the dynamic power error is virtually independent of the wind profile. However, as the mass increases, the average power error becomes more influenced by the mean wind speed profile.

For a mass-to-surface ratio of $\frac{m}{S} = 8\text{kg}\,\text{m}^{-2}$ in the analyzed solution space, the difference in average power error between the logarithmic and uniform wind profiles has a median value of 0.6%. This implies that the error between the dynamic simulation and quasi-steady simulation is approximately 0.6% larger for a logarithmic wind profile than for a uniform wind profile at $\frac{m}{S} = 8\text{kg}\,\text{m}^{-2}$.

Moreover, the interquartile range of the difference in error increases significantly, exceeding 0.40% for heavier kites. This indicates that the uncertainty in the error caused by assuming a certain wind profile (e.g, when comparing simulation data to experimental data), grows with larger kite mass.

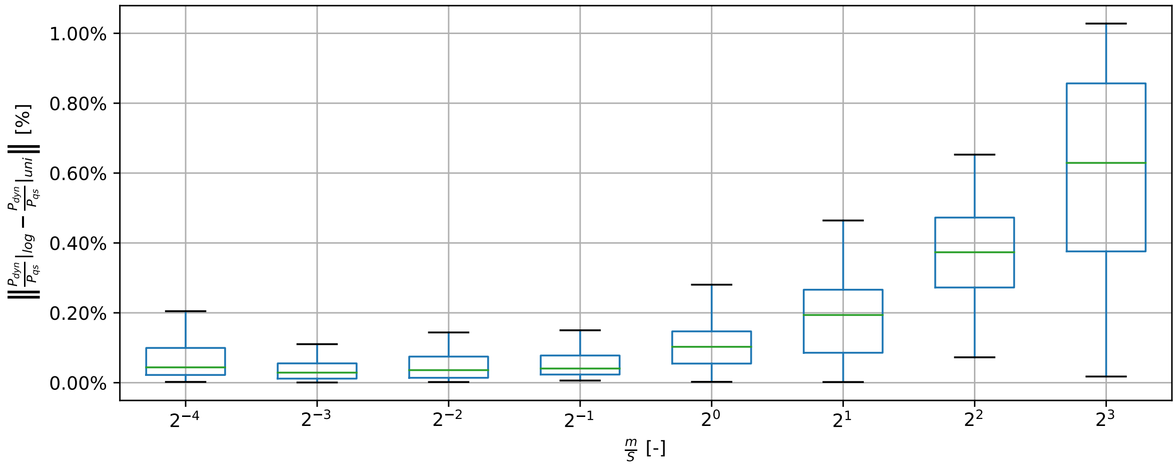

Figure 8.16: Distributions of the difference in the average power error between the dynamic and quasi-steady models obtained with a logarithmic profile, and the average power error obtained with a uniform profile, grouped by the kite mass-to-surface ratio $\frac{m}{S}$. Note how the magnitude of the difference between the dynamic power error and quasi-steady error is larger for heavier kites.

8.4.2. Impact of turbulence

The system response in a turbulent environment can be simulated using the pyconturb Python package. This package allows for the generation of the time evolution of a 2D turbulence field in the yz plane. To obtain the wind speed at a certain horizontal distance and time step, it is assumed that the turbulence convects downwind following the logarithmic mean wind speed profile. Nearest-neighbour interpolation is used to interpolate between data points to maintain the turbulence profile.

The system response in a turbulent environment can be simulated with the `pyconturb` python package. With this package, the time-evolution of a 2D turbulence field in the yz plane can be simulated. To obtain the wind speed at a certain horizontal distance and time step, it is assumed that the turbulence convects downwind following the logarithmic mean wind speed profile. Nearest-neighbour interpolation is used to interpolate between data points to maintain the turbulent velocity profile.

Effect of turbulence on solution

Figure 8.17 shows the responses of the inertia-free, quasi-steady, and dynamic models in the same IEC Class A turbulent environment, classified as 'heavy' turbulence. The figure displays the true wind speed v_τ, altitude, tangential speed v_τ, and tether tension $F_{t,g}$ over time for each model. The differences in the true wind speed profiles are caused by the variations in the models' predicted kite positions at each moment in time. The dynamic model demonstrates how the inclusion of relative and Euler inertial terms leads to a damping effect on the tangential speed and tether tension responses.

To clarify, both the inertia-free and quasi-steady models exhibit very erratic v_τ and $F_{t,g}$ responses. In some instances, a solution could not even be found. On the other hand, the dynamic response shows a smoother solution, which aligns more closely with expectations. The mass of the kite should dampen the perturbations caused by turbulence, which is effectively captured by the dynamic model.

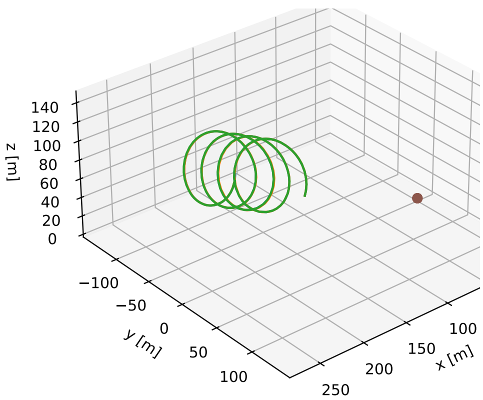

(a) Elevated circle in turbulent environment.

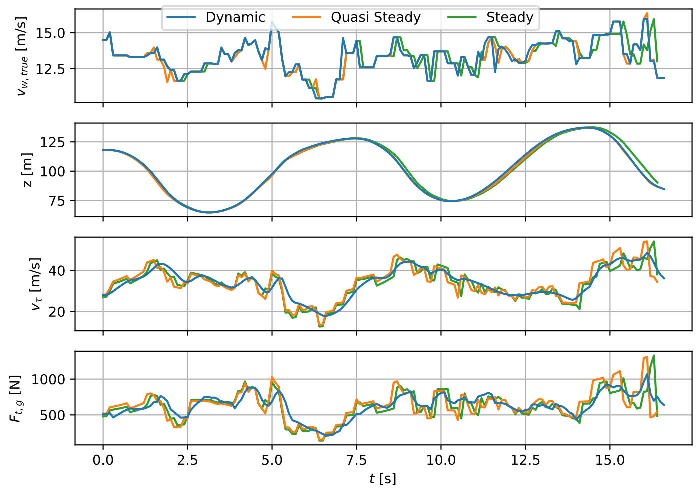

(b) From top to bottom: true wind velocity, altitude, tangential speed, and tether tension, versus time.

Figure 8.17: A kite with mass-to-surface ratio $\frac{m}{S} = 1\,\text{kg}\,\text{m}^{-2}$ flying an elevated circle with constant reelout speed $v_r = 3\,\text{m}\,\text{s}^{-1}$ in an environment with IEC Class A turbulence, with a logarithmic mean wind profile, with the a wind speed $v_{ref} = 12\,\text{m}\,\text{s}^{-1}$ at reference height $90\,\text{m}$. Note how the dynamic model shows a smoother system response to the same turbulent flow conditions.

Sensitivity of the average power to turbulence and mass

Figure 8.18 illustrates how the normalized average power scales with varying turbulence intensity, classified by Class A, Class B, and Class C, versus the kite mass-to-surface ratio, for the inertia-free, quasi-steady, and dynamic models. The inertia-free and quasi-steady models show a high dependency of average power on turbulence intensity, whereas the dynamic model shows a weaker relationship. This can be explained by the resolved kite inertia. The mass dampens the kite velocity and tether force, ensuring that at any point along the trajectory, the tether tension is closer to the value it would have in a non-turbulent environment, compared to the inertia-free and quasi-steady models.

In general, stronger turbulence results in higher average power for all three models. This is counterintuitive because, in a real-world scenario, turbulence typically reduces average power. The instantaneous changes in the angle of attack caused by turbulence result in reduced the average lift-to-drag ratio, but this phenomenon is not resolved by the steady aerodynamic model used in these simulations.

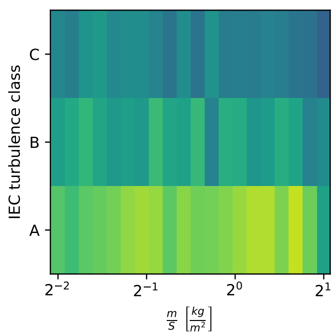

(a) Dynamic

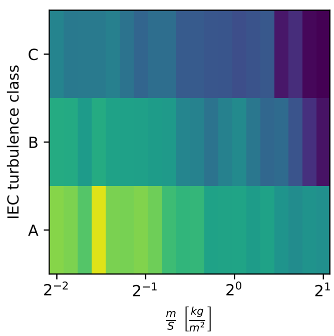

(b) Inertia-free

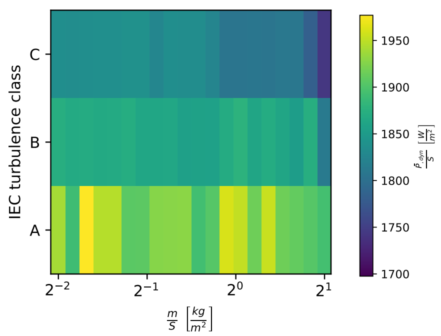

(c) Quasi-steady

Figure 8.18: Sensitivity of the average power error to IEC turbulence category and mass-to-surface ratio $\frac{m}{S}$, for helix radius $r_h = 40\,\text{m}$, path elevation $\beta_P = 30°$ and reeling speed $v_r = 3\,\text{m}\,\text{s}^{-1}$. Gravity included, logarithmic wind profile used with mean wind speed $\bar{v_w} = 12\,\text{m}\,\text{s}^{-1}$ at reference height $z_{ref} = 90\,\text{m}$.

Effect on computational cost

The solution time of the dynamic solver is typically equal to or even lower than that of the quasi-steady solver. Generally, the ratio between computation time and simulated time is in the order of $\mathcal{O}(10^{-1})$, meaning that 100 s of simulation time requires approximately 10 s on a mid-segment 2020 consumer laptop. However, the increased problem stiffness due to turbulence drastically worsens the computation time, by a factor of up to 30 times. In a turbulent environment, the same 100 s of simulation time may now take up to 300 s of computation time if the same tolerance settings and solution algorithm are used.

If an inertia-steady or quasi-steady simulation is performed, the computation time is virtually unaffected by the presence of turbulence. Only the initialization of the turbulence field requires additional time. This difference in the effect on computation time emphasizes the increased problem complexity when the full system dynamics must be resolved in the presence of perturbations such as those due to turbulence.

8.5. Impact of the tether model

The large difference in the predicted tether force in the tangential plane τ, between the two tether models was already discussed in section 7.3. All previous analyses have been conducted without considering the tether mass and drag, such that the assumptions taken in the tether models will not interfere with the conclusions drawn regarding the impact of the kite inertia. To see how the tether model may affect the system response, the sensitivity of the average traction power to the tether cross section A_t is assessed for the two tether models.

$$A_t = \frac{\pi d_t^2}{4}$$

The average power on the m, A_t-plane, obtained with the simplified drag tether model, is illustrated in figure 8.19, the relative error between the results obtained with either tether model is given in figure 8.19b. Both models show a significant decrease in traction power, for increasing tether diameter. The distributed drag tether model shows a greater decrease in traction power for thicker tethers, with a difference of 4% to the simplified drag tether model. Moreover, since the distributed drag tether model shows greater tether drag, the solution space, i.e. the maximum tether diameter for a given mass, is reduced significantly.

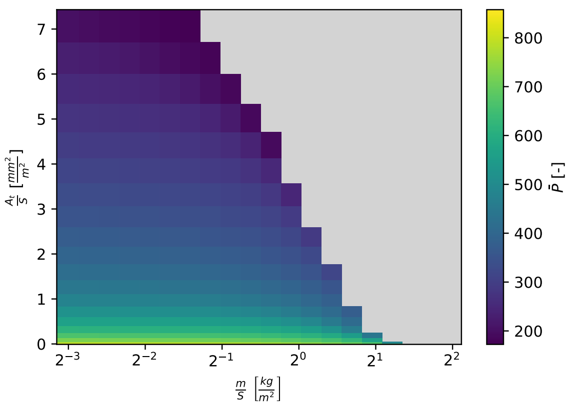

(a) Simplified drag

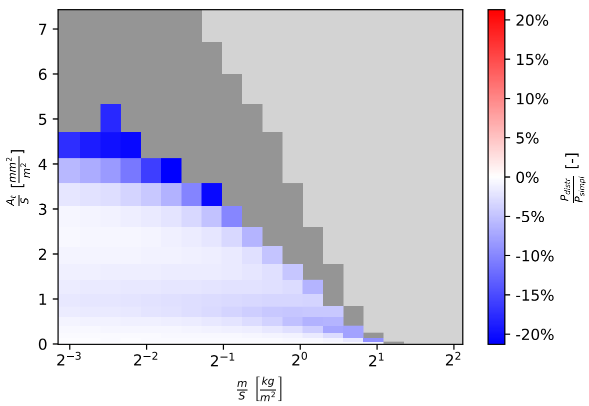

(b) Distributed drag versus simplified drag

Figure 8.19: Average power obtained with the distributed drag tether model on the m, A_t-plane (left) and the difference to the average power obtained with the simplified drag tether model (right). The grey values in figure 8.19b mark the inputs for which the simplified drag tether model has a solution, but the distributed drag tether model not.

9
Conclusions

The objective of this thesis was to advance the understanding of crosswind tethered flight dynamics. The motivation behind this research stems from the need to enhance the predictability of the power generation of Airborne Wind Energy (AWE) systems.

A complete framework for modeling and simulating dynamics was developed, specifically tailored to crosswind tethered flight. The impact of inertial forces was assessed by comparing the performance of inertia-free, quasi-steady, and dynamic models. The conclusions are divided into two sections: section 9.1 summarizes the developed theory, and the impact of inertia is concluded in section 9.2.

9.1. Summary of the developed theory and models

The term 'quasi-steady' has been used loosely in the past to describe kite motion. Such inconsistency is confusing, especially when comparing the performance of various models. In this thesis, precise definitions are provided to promote the use of consistent terminology in future research.

- If kite motion is **steady**, the kite motion, wind and gravity field are all constant in a body reference frame. Realistically, this only may occur during reel-in, when the course angle is constant and the tangential speed zero. A steady flight state is thus irrelevant in the context of crosswind tethered flight.
- If kite motion is **dynamic**, the kite is subject to all forms of inertial forces, i.e. those caused by relative, centrifugal, Coriolis and Euler accelerations. When expressed in the course reference frame, dynamic motion is governed by a 3-DOF, coupled, mixed order system of differential equations.
- Under the **inertia-free** assumption, all inertia forces are assumed to be sufficiently small relative to the external forces, such that they can be neglected. The kite's speed and direction thus vary instantaneously with a change in the external forces. Hypothetically, the inertia-free equilibrium equations dictate rectilinear kite motion with constant speed. The inertia-free assumption results in a 'zero' order differential equation of motion, as the sum of the external forces equals the zero vector.
- Under the **quasi-steady** assumption, it is assumed that the equilibrium state governed by constant tangential and radial speed components is stable, and that any perturbation from this quasi-steady equilibrium decays sufficiently fast to allow for the kite motion to be modeled as a sequence of quasi-steady states. The quasi-steady equilibrium equations hypothetically dictate the kite to follow a curved trajectory at a constant speed, with this trajectory constrained by the constant reel-out speed. Under the quasi-steady assumption, the centrifugal forces due to the kite's directional change are resolved, as well as the Coriolis forces and part of the Euler forces. This allows to solve more of the unsteady effects inherently present in crosswind tethered flight, such as those caused by kite steering and kite reel-out. The quasi-steady assumption reduces the dynamic equations of motion into a 3-DOF system of first order differential equations, with the inertial force becoming time-invariant.

The equations of motion for the inertia-free, quasi-steady and dynamic models are derived in the spherical 'course reference frame'. This reference frame is specifically tailored to AWE applications, making the EOM more concise and less complicated compared to expressions in the traditional physics convention spherical reference system.

Additionally, explicit equations for the aerodynamic force and the tether force were derived. The aerodynamic coefficients C_L, C_D were assumed to be constant. The tether was assumed to be straight and inertia-free. Two variations of tether drag were derived: a simplified tether drag model, analogous to Van Der Vlugt et al. [15] and Schmehl et al. [3], and a distributed drag model, which resolves the exponential drag distribution along the tether. Since the aerodynamic and tether force equations are explicit, they can be easily substituted into the EOM to form a system of three equations with three unknowns, allowing for straightforward solution of system states.

Various formulations to simulate motion along a parameterized path were developed. Explicit parameterization in s may lead to an unrealistic reel-out strategy; therefore, another formulation that handles constant reel-out speed is presented. Two algorithms were derived, to integrate the position of a kite along such parameterized path: a quasi-steady position integration scheme, and a dynamic position integration scheme. The first scheme is used to simulate steady or quasi-steady kite motion, the latter solves the second order initial value problem of dynamic kite motion. The benefit of flight path parameterization is that the number of DOFs in the EOM is reduced from three to one.

The presented modeling framework serves as a foundational step for future research, enabling more in-depth investigation of the many unsteady phenomena present in AWE systems.

9.2. The impact of kite inertia

The impact of inertial forces on the behavior of crosswind tethered kites was rigorously assessed by comparing the steady, quasi-steady, and dynamic models. The dynamic model was verified through a comparison with Talmar's analytical solution for a downwind helix. Additionally, the distributed tether drag model was qualitatively verified, but a significant discrepancy with the simplified model indicated that the choice of the used tether model should be carefully considered.

Depending on which EOM are solved (i.e., inertia-free, quasi-steady, or dynamic), a state variable's time response varies in terms of the average value, amplitude, and phase. To quantify these effects, the normalized average traction power $\frac{\bar{P}}{S}$, speed variation along a maneuver Δv_τ , and phase of the maximum speed point $\Phi_{v_{\tau,\max}}$ were analyzed. The sensitivity of these metrics to kite mass, reelout speed, path curvature, and lift-to-drag ratio was determined across the solution space for a kite flying an elevated helix with constant reelout speed, in an environment with gravity and uniform wind speed. Tether drag and mass were neglected in this analysis. Comparing the solution spaces provided insights into the effects of inertial forces.

The error in average power between quasi-steady and dynamic models is influenced by many factors, and no straightforward dependency on operational parameters was observed. Towards the feasibility boundaries of kite mass, reel-out speed, helix radius, and lift-to-drag ratio, the magnitude of the error exceeds 3%. Wrinkles in the power error graphs are attributed to differences in the number of completed maneuvers when the tether reaches its maximum length.

The errors in speed variation Δv_τ of the inertia-free and quasi-steady compared to the dynamic model is most significant for heavy kites with high lift-to-drag ratios, reaching up to 200% near the maximum mass feasibility boundary. This error is also large near the minimum helix radius boundary, where the kite does not have sufficient time to accelerate towards the quasi-steady state.

The phase error between quasi-steady and dynamic models is significant and likely contributes to the roughness of the average power error solution space. The phase delay increases with the relevance of inertial forces, such as by decreasing the helix radius or increasing the kite mass. The steady model generally predicts a more accurate phase than the quasi-steady model across all conditions, as the exclusion of centrifugal forces mitigates the errors caused by Euler and relative accelerations.

From these differences in the solution spaces, and the comparison of simulations with specific inertial force components resolved, several conclusions can be drawn about the inertial forces. Centrifugal forces, resolved by the quasi-steady model, are the most dominant inertial forces concerning the average values of a state variable's time response, such as average power. The inertial forces governed by $\dot{v}_\tau$ and $\dot{v}_r$, i.e. the relative accelerations and part of the Euler accelerations, are the most dominant concerning the amplitude and phase of a time response. They significantly dampen the response, and cause a phase delay in terms of s. The effect of Coriolis forces is small compared to the other inertial terms, albeit a minimal phase delay and decrease of the average value.

The error in average power for quasi-steady or dynamic models also depends on wind conditions. The contribution of phase differences to the average power error is amplified with a non-uniform wind profile, such as a logarithmic profile. The presence of turbulence further amplifies differences between the three models, as only the dynamic model accounts for mass-induced damping of perturbations.

The dynamic solver performance depends on the stiffness of the problem. For simple paths with smooth solutions, the initial value problem is easily solved, often faster than the quasi-steady model. However, as the problem becomes stiffer, such as in the presence of turbulence, the solver requires significantly more time compared to quasi-steady simulations.

For practical applications, if only the average power is of interest and kite operation remains within a reasonable regime, modeling under the quasi-steady assumption is sufficient to obtain a reasonably low error. However, a quasi-steady solution does not always exist, while the solution space of a dynamic model is significantly larger. Close to the feasibility boundaries of the quasi-steady model, it is recommended to use a dynamic model as there, the effects of the inertia are most severe.

10 Recommendations

10.1. Improvements to the current work

Several potential improvements to the current modeling framework have been identified, which could enhance the accuracy of the presented differences between the steady, quasi-steady and dynamic results.

Firstly, implementing a quasi-steady aerodynamic model would be beneficial. Currently, the aerodynamic coefficients C_L, C_D are assumed constant, which implies a constant orientation of the kite with respect to the apparent wind vector. This assumption is particularly unrealistic at the beginning of the downwind part of the flight path, where the aerodynamic yaw is the highest in magnitude. A model that accounts for changes in lift and drag due to sideslip would yield more realistic force and acceleration profiles throughout the traction pattern. Also, such model is more suited for the simulation of a turbulent environment, than what has been used in this work. However, this requires a kite model that resolves the kite orientation.

Another area for improvement is the implementation of realistic reel-in and transition phases. The current work only presents the differences in the traction phase, where the kite is in a powered state. The steady model has already been proven to significantly deviate from empiric test data during the reel-in and transition phases by Schelbergen et al. [13]. Resolving these flight phases would likely affect the presented discrepancies between the steady, quasi-steady and dynamic models.

Additionally, implementing implicit parameterized control, such as reeling with constant tether force instead of reel-out speed could provide a more accurate representation of the kite's dynamics, especially during phases with significant force variations.

Another improvement to the path control schemes is related to the quasi-steady parameterized position integration scheme. The truncation error of this scheme varied locally with the change in flight path curvature, thus contributing to the inertia-free and quasi-steady model errors. If a dynamic time step is used, accounting for the local change in path curvature, a potential model bias caused by the truncation error may be mitigated.

Also a more detailed tether model, for instance one that discretizes the tether into lumped masses and resolves the corresponding inertias, would enhance the model's accuracy. Currently, the tether is assumed steady, or its mass and drag have been neglected completely. Simulating with a more detailed tether models would yield a more realistic representation of the system dynamics.

Finally, the role of the path elevation angle β_P could be investigated more. The phase differences between the quasi-steady model and steady model for a downwind circle in section 8.1 were much smaller than for the elevated helix in section 8.3. A more detailed investigation into how β_P affects model accuracy could provide valuable insights.

10.2. Research made accessible by the current work

The developed modeling framework enables more accurate investigation into several previously researched topics and opens new avenues for future research.

With the developed modeling framework, previous work can be revisited with more accuracy. The phase difference between speed and acceleration, resolved by this model but unresolved in quasi-steady models, likely affects the the outcomes of optimization studies. For example, using the dynamic model would likely affect the optimal pumping cycle studied by Fechner in [17], or the optimal farm layout studied by Johnson in [19].

Additionally, obtaining a universal formula for the quasi-steady model error would be beneficial. Being able to determine a priori the quasi-steady model error as a function of kite properties (e.g. surface-to-mass ratio, lift-to-drag ratio), and operational parameters (e.g. reeling speed, path elevation, helix radius), would be very useful when performing analyses with a quasi-steady model. Obtaining such relationship requires a drastically more extensive analysis of the complete solution space of the presented model framework, due to the many intricacies affecting the quasi-steady model error.

The dynamic model could further be used to study other unsteady phenomena present in AWE systems. Investigating the impact of turbulence on the energy production can be done using the current model, when a quasi-steady aerodynamic model is implemented. This combination will allow the resolution of force changes due to angle of attack variations in turbulent conditions.

Finally, if the current framework is enriched with a quasi-steady aerodynamic model and a non-rigid tether model, the currently left untouched topic of aerodynamic damping induced by atmospheric turbulence and tether deformation, could be researched.

References

[1] Gonzalo Sánchez-Arriaga, Stefanie Thoms, and Roland Schmehl, eds. *The International Airborne Wind Energy Conference 2024: Book of Abstracts*. Madrid, Spain: Delft University of Technology, Apr. 25–26, 2024. 200 pp. doi: 10.4233/uuid:85fd0eb1-83ec-4e34-9ac8-be6b32082a52.

[2] Miles L. Loyd. “Crosswind Kite Power”. In: *Journal of energy* 4.3 (1980), pp. 106–111. doi: 10.2514/3.48021.

[3] Roland Schmehl, Uwe Ahrens, and Moritz Diehl. *Airborne Wind Energy*. Berlin, Heidelberg: Springer, 2013. doi: 10.1007/978-3-642-39965-7.

[4] Cristina L. Archer, Luca Delle Monache, and Daran L. Rife. “Airborne wind energy: Optimal locations and variability”. In: *Renewable Energy* 64 (Apr. 2014), pp. 180–186. doi: 10.1016/j.renene.2013.10.044.

[5] Antonello Cherubini et al. “Airborne Wind Energy Systems: A review of the technologies”. In: *Renewable and Sustainable Energy Reviews* 51 (Nov. 2015), pp. 1461–1476. issn: 1364-0321. doi: 10.1016/j.rser.2015.07.053.

[6] *Kitepower Falcon 100kW Airborne Wind Energy System*. url: https://thekitepower.com/product/ (visited on 11/11/2023).

[7] U. Fechner and R. Schmehl. “Downscaling of Airborne Wind Energy Systems”. English. In: *Journal of Physics: Conference Series* 753 (2016). doi: 10.1088/1742-6596/753/10/102002.

[8] Udo Zillmann and Philip Bechtle. “Emergence and Economic Dimension of Airborne Wind Energy”. In: *Airborne Wind Energy: Advances in Technology Development and Research*. Ed. by Roland Schmehl. Green Energy and Technology. Singapore: Springer, 2018, pp. 1–25. doi: 10.1007/978-981-10-1947-0_1.

[9] U. Fechner. “A Methodology for the Design of Kite-Power Control Systems”. en. PhD. Delft University of Technology, 2016. doi: 10.4233/UUID:85EFAF4C-9DCE-4111-BC91-7171B9DA4B77.

[10] Steffen Schön and Gaël Kermarrec. “Turbulence Theory”. In: *Handbook of Geomathematics*. Ed. by Willi Freeden, M. Zuhair Nashed, and Thomas Sonar. Berlin, Heidelberg: Springer, 2020, pp. 1–45. doi: 10.1007/978-3-642-27793-1_77-3.

[11] Storm Dunker. “Tether and Bridle Line Drag in Airborne Wind Energy Applications”. In: *Airborne Wind Energy: Advances in Technology Development and Research*. Ed. by Roland Schmehl. Green Energy and Technology. Singapore: Springer, 2018, pp. 29–56. doi: 10.1007/978-981-10-1947-0_2.

[12] Rachel Leuthold. “Multiple-Wake Vortex Lattice Method for Membrane-Wing Kites”. MA thesis. Delft University of Technology, Dec. 2015. doi: 10.13140/RG.2.2.30811.41765.

[13] M. Schelbergen and R. Schmehl. “Validation of the quasi-steady performance model for pumping airborne wind energy systems”. English. In: vol. 1618. ISSN: 1742-6588 Issue: 3. 2020. doi: 10.1088/1742-6596/1618/3/032003.

[14] M. N. Noom. “Theoretical Analysis of Mechanical Power Generation by Pumping Cycle Kite Power Systems”. en. MA thesis. Delft University of Technology, 2013. url: https://repository.tudelft.nl/islandora/object/uuid%3A1c1a3e90-11e6-4fe7-8808-8c6a1227dadb (visited on 06/11/2024).

[15] Rolf van der Vlugt et al. “Quasi-steady model of a pumping kite power system”. In: *Renewable Energy* 131 (2019), pp. 83–99. doi: 10.1016/j.renene.2018.07.023.

[16] Roland B. Stull. *Meteorology for Scientists and Engineers*. University of California: Brooks/Cole, 2000.

[17] Uwe Fechner and Roland Schmehl. “Model-Based Efficiency Analysis of Wind Power Conversion by a Pumping Kite Power System”. In: *Airborne Wind Energy*. Ed. by Uwe Ahrens, Moritz Diehl, and Roland Schmehl. Green Energy and Technology. Berlin, Heidelberg: Springer, 2013, pp. 249–269. doi: 10.1007/978-3-642-39965-7_14.

[18] Marcos Jerez Venegas. “Path Optimization of a Pumping Kite System”. en. MA thesis. Delft University of Technology, 2017. url: https://repository.tudelft.nl/islandora/object/uuid%3A0a67e3e9-358a-494f-a553-b65ed9f3c8c6 (visited on 06/11/2024).

[19] Holly Johnson. “Kite Farm Simulation: Assessing the impact of flight paths for multiple-unit airborne wind energy systems”. MA thesis. Delft University of Technology, 2019. url: https://repository.tudelft.nl/islandora/object/uuid%3A8afd27a0-f943-40c6-b3f3-10f7e570c0d5 (visited on 06/12/2024).

[20] M. Schelbergen et al. “Clustering wind profile shapes to estimate airborne wind energy production”. In: *Wind Energy Science* 5.3 (2020), pp. 1097–1120. doi: 10.5194/wes-5-1097-2020.

[21] Mihkel Talmar. “Quasi-Steady Model Enhancements of Airborne Wind Energy Systems”. MA thesis. Delft University of Technology, July 2021. url: https://repository.tudelft.nl/record/uuid:7101b8ec-25b7-49a1-a49e-7a9348267938 (visited on 08/08/2024).

[22] Uwe Fechner et al. “Dynamic model of a pumping kite power system”. In: *Renewable Energy* 83 (Nov. 2015), pp. 705–716. doi: 10.1016/j.renene.2015.04.028.

[23] Herbert Goldstein, Charles P. Poole, and John L. Safko. *Classical Mechanics*. 3rd. San Francisco: Addison-Wesley, 2002.

[24] Bernard Etkin. *Dynamics of Atmospheric Flight*. New York: Wiley, 1972.

[25] Roland Schmehl et al. “Airborne Wind Energy for Martian Habitats”. In: *Adaptive On- and Off-Earth Environments*. Ed. by Angelo Cervone, Henriette Bier, and Advenit Makaya. Cham: Springer, 2024, pp. 145–197. doi: 10.1007/978-3-031-50081-7_7.

[26] Rolf H. Luchsinger. “Pumping Cycle Kite Power”. In: *Airborne Wind Energy*. Ed. by Uwe Ahrens, Moritz Diehl, and Roland Schmehl. Green Energy and Technology. Berlin, Heidelberg: Springer, 2013, pp. 47–64. doi: 10.1007/978-3-642-39965-7_3.

A

Simulation parameters

Parameterization equations

This appendix provides the parameterization equations used in the simulation. The following functions define the position in terms of the variable s. In case of a constant reelout simulation, the function for $x'(s)$ is replaced by:

$$r(t) = r_{min} + v_r t$$

Helix

$$x'(s) = \sqrt{r_0^2 - r_h^2} + s$$
$$y'(s) = r_h \sin(\omega s)$$
$$z'(s) = r_h \cos(\omega s)$$

Figure eight

$$x'(s) = \sqrt{r_0^2 - r_y^2} + s$$
$$y'(s) = r_y \cos(\omega s)$$
$$z'(s) = r_z \sin(2\omega s)$$

Operational parameters

This appendix provides the operational parameters used in the simulations. Unless otherwise specified, the values listed here are used.

Parameter	**Value**
Air density [kg/m^3]	1.225
Gravitational acceleration [kgm/s^2]	9.81
Kite drag coefficient [-]	0.2
Kite lift coefficient [-]	0.8
Path elevation angle [deg]	35
Reference wind speed [m/s]	10
Tether density [kg/m^3]	724
Tether diameter [m]	0.004
Tether drag Coefficient [-]	1.1
Tether maximum length [m]	400
Tether minimum length [m]	200